

# Four-Wave Mixing Techniques Applied to the Investigation of Non-Adiabatic Dynamics in Polyatomic Molecules

**Dissertation**

zur Erlangung des

naturwissenschaftlichen Doktorgrades

der Bayerischen Julius–Maximilians–Universität Würzburg

vorgelegt von

**Torsten Uwe Siebert**

aus Wiesbaden

Würzburg 2002

Eingereicht am:  
bei der Fakultät für Chemie und Pharmazie

1. Gutachter: .....  
2. Gutachter: .....  
der Dissertation

1. Prüfer: .....  
2. Prüfer: .....  
der mündlichen Prüfung

Tag der mündlichen Prüfung: .....

Doktorurkunde ausgehändigt am: .....

*To my family and Liana*



# Contents

List of Figures . . . . .	vii
<b>1 Introduction and Motivation</b>	<b>1</b>
<b>2 Theory</b>	<b>7</b>
2.1 Time-Resolved, Third-Order Optical Spectroscopy . . . . .	7
2.1.1 Perturbation Theory for Third-Order Interactions . . . . .	8
2.1.2 Induction and Propagation of a First-Order Polarization . . . . .	10
2.1.3 Formation and propagation of a Population Grating . . . . .	13
2.1.4 Induction of a Third-Order Polarization and Bragg Scattering . . . . .	17
2.2 Classification of Four-Wave Mixing Techniques . . . . .	22
2.2.1 Time-Resolved Coherent anti-Stokes Raman Scattering . . . . .	23
2.2.2 Time-Resolved Coherent Stokes Raman Scattering . . . . .	27
2.2.3 Transient Gratings . . . . .	29
2.3 Theoretical Treatment of Elementary Molecular Dynamics . . . . .	33
2.3.1 Wave-Packet Formalism of Coherent Vibrational States . . . . .	33
2.3.2 Internal Conversion in Polyatomic Molecules . . . . .	35
<b>3 Experimental Setup</b>	<b>45</b>
3.1 Generation and Characterization of Femtosecond Laser Pulses . . . . .	45
3.1.1 1 kHz Laser System . . . . .	46
3.1.2 100 kHz Laser System . . . . .	48
3.2 Phase-Matching for Four-Wave Mixing Schemes . . . . .	50
3.3 CCD Broadband Detection . . . . .	53
<b>4 The State Selectivity of fs Time-Resolved Four-Wave Mixing</b>	<b>57</b>
4.1 Methodology of Time-Resolved Degenerate Four-Wave Mixing . . . . .	58
4.2 Experimental Results: CCD-Broadband Detection of Time-Resolved Four-Wave Mixing . . . . .	60
4.3 Discussion: State-Selectivity of Different FWM Processes . . . . .	66

---

<b>5</b>	<b>Non-adiabatic Transitions in Polyatomic Molecules</b>	<b>71</b>
5.1	The System: $\beta$ -Carotene . . . . .	72
5.2	The Role of Specific Vibrational Modes During an Internal Conversion Process . . . . .	75
5.2.1	Methodology of the <i>Pump</i> -CARS Scheme . . . . .	79
5.2.2	Experimental Results: CARS as a Mode-Selective Probe Process in a <i>Pump-Probe</i> Scheme . . . . .	86
5.2.3	Discussion: Nuclear Motion Involved in the $S_1/S_0$ Internal Conversion of $\beta$ -Carotene . . . . .	97
5.3	The Behavior of Vibrationally Hot Modes during Internal Conversion	106
5.3.1	Methodology of Population Gratings in $\beta$ -Carotene . . . . .	107
5.3.2	Experimental Results: Probing Vibrationally Hot Modes in Electronic Dark States . . . . .	109
5.3.3	Discussion: Vibrational Cooling and the Increasing Rate of Internal Conversion . . . . .	118
<b>6</b>	<b>Conclusion – Zusammenfassung</b>	<b>125</b>
6.1	Conclusion . . . . .	125
6.2	Zusammenfassung . . . . .	129
	<b>Bibliography</b>	<b>133</b>
	<b>Acknowledgements</b>	<b>143</b>

# List of Figures

2.1	Transient grating picture, potential energy diagram and double-sided Feynman diagram showing the formation of a first-order polarization.	11
2.2	Transient grating picture, potential energy diagram and double-sided Feynman diagram showing the formation of a population grating of molecules in the electronic ground state. . . . .	15
2.3	Transient grating picture, potential energy diagram and double-sided Feynman diagram showing the formation of a population grating of molecules in an electronically excited state. . . . .	16
2.4	Transient grating picture, potential energy diagram and double-sided Feynman diagram showing the formation of a third-order polarization initiating from molecules in the electronic ground state. . . . .	19
2.5	Transient grating picture, potential energy diagram and double-sided Feynman diagram showing the formation of a third-order polarization initiating from molecules in an electronically excited state. . . . .	20
2.6	Schematic representation of the temporal sequence of the three laser pulses involved in the DFWM process, $(\mathbf{k}_1, \mathbf{k}_2, \mathbf{k}_3)$ illustrating the relaxation processes taking place within the parametric delay times, $\Delta t_{12}$ and $\Delta t_{23}$ . . . . .	21
2.7	Potential energy diagrams and double-sided Feynman diagrams describing a time-resolved CARS process. . . . .	24
2.8	Potential energy diagrams and double-sided Feynman diagrams describing a time-resolved CSRS process. . . . .	28
2.9	Potential energy diagram and double-sided Feynman diagram describing a transient grating process. . . . .	30
2.10	Schematic representation of a conical intersection between two electronic states of a polyatomic molecule. . . . .	41
3.1	Experimental setup of a femtosecond laser system operating at a repetition rate of 1 kHz. . . . .	47
3.2	Experimental setup of a femtosecond laser system operating at a repetition rate of 100 kHz. . . . .	49

3.3	Beam geometry for achieving the phase-matching condition of a DFWM process . . . . .	52
3.4	Beam geometries for achieving the phase-matching conditions involved in a CARS and transient grating process. . . . .	54
4.1	Potential energy diagram of gaseous iodine showing the vibrational and electronic states accessed in a time-resolved DFWM experiment. . . . .	59
4.2	Contour plot of the DFWM signal intensity as a function of the delay time and the detection wavelength acquired by means of a CCD multi-channel detection of a time-resolved DFWM experiment on gaseous iodine. . . . .	61
4.3	Plots of the FWM signal at different spectral positions as a function of the delay time showing the wave packet dynamics in gaseous iodine characteristic for a CARS, CSRS and DFWM process. . . . .	62
4.4	Fourier transformations of the transient FWM signal at different spectral positions of FWM spectrum showing the state-selectivity of a CARS, CSRS and DFWM process in gaseous iodine. . . . .	64
4.5	Plots of the FWM signal as a function of the delay time showing the continuous transition from a DFWM to a CARS process as the detection is shifted to the blue side of the FWM spectrum. . . . .	68
5.1	Structural representation and illustration of the relevant electronic states of <i>all-trans-<math>\beta</math>-carotene</i> . . . . .	73
5.2	Schematic potential energy diagram of $\beta$ -carotene illustrating the experimental realization of a <i>pump-CARS</i> scheme. . . . .	80
5.3	Absorption spectrum of $\beta$ -carotene in <i>n</i> -hexane showing the spectral positions of the lasers pulses involved in a <i>pump-CARS</i> experiment. . . . .	82
5.4	Resonance Raman spectrum and the spectral profiles of the different CARS signals obtained from $\beta$ -carotene in <i>n</i> -hexane. . . . .	83
5.5	Schematic potential energy diagram of $\beta$ -carotene illustrating the experimental scheme used to resolve the CARS process in time within a <i>pump-CARS</i> scheme. . . . .	85
5.6	Plots of the CARS signal intensity obtained from $\beta$ -carotene as a function of the delay time between the <i>initial pump</i> laser and the CARS process. Five transients are shown that were recorded by tuning the lasers of the CARS process to different vibrational modes of $\beta$ -carotene in the electronic ground state. . . . .	87
5.7	Illustration of the theoretical formalism used to describe the resonance enhancement of a CARS process. . . . .	89
5.8	Plot of the CARS signal intensity obtained from $\beta$ -carotene by resolving the CARS process in time within a <i>pump-CARS</i> scheme. . . . .	95



---

5.9	Resonance Raman spectrum of the $S_1$ and $S_0$ state in $\beta$ -carotene measured by Hashimoto and Koyama. <sup>98</sup> . . . . .	96
5.10	Wavenumber positions of the vibrational modes probed with the CARS process as a function of the time constant, $\tau$ that describes the population flow into the vibrational modes of the electronic ground state of $\beta$ -carotene subsequent to the $S_1/S_0$ internal conversion. . . . .	98
5.11	Schematic model for the repopulation of the vibrational modes in the electronic ground state of $\beta$ -carotene subsequent to the $S_1/S_0$ internal conversion. . . . .	104
5.12	Schematic potential energy diagram of $\beta$ -carotene showing the experimental strategy of a transient grating scheme. . . . .	108
5.13	Contour plot of the intensity of the scattered <i>probe</i> pulse as a function of the delay time and the spectral position of the <i>probe</i> pulse obtained from a transient grating experiment on $\beta$ -carotene. . . . .	110
5.14	Intensity of the scattered <i>probe</i> pulse at five different spectral positions as a function of the delay time obtained from a transient grating experiment on $\beta$ -carotene. The plots show the fits to the experimental data using Model 1 in the fit procedure. . . . .	112
5.15	The percentage of cooling as a decay channel out of the probe window in the $S_1$ state of $\beta$ -carotene shown as a function of the spectral position of the <i>probe</i> pulse. The results were obtained by using Model 1 in the fit procedure. . . . .	116
5.16	Intensity of the scattered <i>probe</i> pulse at five different spectral positions as a function of the delay time obtained from a transient grating experiment on $\beta$ -carotene. The plots show the fits to the experimental data using Model 2 in the fit procedure. . . . .	117
5.17	The percentage of cooling as a decay channel out of the probe window in the $S_1$ state of $\beta$ -carotene shown as a function of the spectral position of the <i>probe</i> pulse. The results were obtained by using Model 2 in the fit procedure. . . . .	118
5.18	Parameters obtained from the fits to the transient grating data giving the percentage of cooling as a decay channel and the time constants for the $S_1/S_0$ internal conversion as a function of the probe energy using Model 1 and 2 in the fit procedure. . . . .	121



# Chapter 1

## Introduction and Motivation

Since the beginnings of quantum theory, a better understanding of the vast complexity innate to polyatomic molecules has been the aim of numerous theoretical and experimental works.<sup>1-3</sup> One of the challenging aspects of this complex problem is the interaction between the different forms of motion available to a polyatomic system. Particularly interesting is the coupling between nuclear and electronic motion in a polyatomic molecule, which governs elementary aspects of photochemistry and photobiology.<sup>4-11</sup> Here, the coupling of these two forms of molecular dynamics determines the pathway of photochemical reactions such as electron transfer, photo-dissociation and photo-isomerization and plays a central role in the mechanism of highly efficient photobiological processes such as vision and photosynthesis.<sup>12-15</sup> The electronic transitions and nuclear dynamics involved in these processes take place on an ultrafast timescale and it is the revolution in laser technology, opening the possibility of laser spectroscopy with femtosecond time resolution (fs =  $10^{-15}$  s), that allows for the direct observation of these forms of molecular dynamics as they take place. The new insight into the dynamic aspects of molecules observed on the relevant timescale has brought great advances to the field of molecular physics.<sup>16-18</sup> This development climaxed in 1999 with the award of the Nobel prize in chemistry to Ahmed Zewail, one of the founders of femtosecond laser spectroscopy.

On this ultrafast timescale, third-order, optical spectroscopy has shown the capability to address many facets of molecular dynamics due to the many degrees of freedom innate to this type of spectroscopic method.<sup>9,19-21</sup> In the area of time-resolved, coherent Raman scattering, pioneering work on the femtosecond timescale was per-

formed in the groups of Laubereau, Zinth and Kaiser.<sup>22</sup> Here, the excitation and dephasing of coherent Raman modes were first characterized with these techniques in the liquid phase.<sup>23,24</sup> In the group of Laubereau, the different tensor components of the third-order susceptibility could be isolated utilizing different polarization geometries within the framework of femtosecond time-resolved, coherent anti-Stokes Raman Scattering (CARS). This allowed for the isolation of the Raman resonant, isotropic element.<sup>25-27</sup> The slow dephasing of vibrational coherences on the femtosecond timescale under the collision-free conditions of gas phase samples facilitates the preparation and observation of wave packet dynamics on different electronic potentials within the coherent Raman techniques. This was utilized in the group of Kiefer for characterizing the state-selectivity of these techniques.<sup>28-30</sup> With the theoretical description of these third-order processes in the framework of higher order perturbation theory in the group of Engel, the relevance of Raman resonant processes versus process that utilize virtual states could be shown.<sup>31-33</sup>

Fundamental contributions in the area of photon echo were made in the group of Wiersma.<sup>34</sup> Here, two and three pulse photon echo schemes as well as multiple color experiments were developed. With this, the dephasing of optical transitions and the population flow in electronic states of different types of chromophors were monitored utilizing the different temporal schemes of the laser pulses involved. The contribution of the homogeneous dephasing could be separated from the effects of an inhomogeneous ensemble. In the group of Shank, the full scope of the temporal schemes available to three pulse photon echo were utilized to show the effects of coherent phonon motion on the dephasing of an optical transition in a semiconductor.<sup>35</sup> Also, valuable information on the interaction between an optical transition and the solvent environment could be gained through photon echo peak-shift measurements performed by de Boeij *et.al.*<sup>36,37</sup> Here, the interaction of the optical transition with varying solvent environments could be observed in a chromophor in solution along with the development of vibrational wave packets, coupled to the optical transition. With the theoretical framework provided by the group of Mukamel, infrared photon echo experiments are reaching the equivalent of multidimensional NMR techniques in gaining structural information of polyatomic molecules by utilizing the vibrational states of the system.<sup>38</sup> This was achieved in the group of Hochstrasser by resolving the infrared echo signal in time with a heterodyn gating technique.<sup>39,40</sup> With

this complex structural information of peptides can be attained. Further complex biological systems have also been addressed with these spectroscopic methods in the group of Fleming. Here, photon echo experiments were carried out in order to investigate the energy transfer between different types of pigments in photosystem II, which constitutes one of the light harvesting units in photosynthesis.<sup>41</sup>

Third-order optical processes have also been employed as a probe mechanism of transient states in femtosecond time-resolved experiments. In the group of Zewail, degenerate four-wave mixing (DFWM) was first established as a probe mechanism on this timescale.<sup>42</sup> Here, *pump*-DFWM and *pump-control*-DFWM schemes utilize one or two auxiliary laser pulses to prepare the molecular dynamics that are interrogated by a time delayed DFWM process. By comparing the results to classical time-resolved *pump-probe* experiments, that employ laser induced fluorescence as the probe signal, the transient population monitored by the DFWM process could be determined.

The experiments presented in this work utilize the ultrashort timescale, made available by state of the arts femtosecond laser technology, for exploring the coupling between nuclear and electronic motion in a polyatomic molecule. For this, a spectroscopic method must be used, that is capable of disentangling the effects of different forms of nuclear motion on a particular electronic transition in a polyatomic molecule. Specifically in this work, the capability of third-order, optical processes to address this problem is explored.

Experiments will first be presented, that determine the selectivity of third-order, spectroscopic schemes such as the coherent Raman techniques and degenerate four-wave mixing with respect to the electronic potential on which nuclear dynamics are initiated and interrogated. These experiments are performed on the well characterized molecular system of gaseous iodine in order to guarantee for a clear interpretation of the state selectivity of these methods. For this purpose, CCD broadband detection of the spectrally dispersed signal is introduced to this form of time-resolved spectroscopy. The analysis of the different spectral channels in the signal shows the state selectivity of the coherent Stokes, and coherent anti-Stokes Raman process as well as the degenerate four-wave mixing, which are simultaneously generated by the spectrally broad femtosecond laser pulses employed in the degenerate four-wave mixing experiment.

With the knowledge gained from these experiments, coherent anti-Stokes Raman

scattering, is applied to the coupling of nuclear and electronic motion in the molecular system of *all-trans*  $\beta$ -carotene in solution. This molecular system is chosen for the experiments due to its significant role in photosynthesis as an auxiliary light harvesting system as well as an energy and triplet quencher in photo-system II. The coupling of nuclear motion to electronic transitions is an important element in the mechanism with which  $\beta$ -carotene fulfills its role in photosyntheses, making this molecular system particularly relevant for addressing this subject. Specifically, the population flow from the first excited singlet state ( $S_1$ ) to the electronic ground state ( $S_0$ ), facilitated through the  $S_1/S_0$  internal conversion, and the subsequent internal vibrational energy redistribution and vibrational cooling processes are monitored selectively with respect to the different forms of nuclear motion in  $\beta$ -carotene. This is realized by exciting  $\beta$ -carotene into the second excited singlet state ( $S_2$ ) state with an auxiliary pump laser pulse and interrogating the population recovery into the electronic ground state by means of a time delayed, coherent anti-Stokes Raman process. This spectroscopic scheme is referred to as a *pump-CARS* scheme in analogy to the classical *pump-probe* scheme in time-resolved spectroscopy. Here, the profound enhancement of the CARS signal intensity in the case of a Raman resonance to a specific vibrational mode is utilized as an intensity filter that amplifies the signal from the vibrational modes of interest, making the contributions from other vibrational modes negligible. This filter allows for the population flow in a specific vibrational mode to be monitored as the radiationless electronic transition between the  $S_1$  and  $S_0$  state takes place. This spectroscopic scheme opens the possibility to observe the type of nuclear motion coupled to the  $S_1/S_0$  internal conversion and with this, identify the reaction coordinate of this electronic transition.

The  $S_1/S_0$  internal conversion in  $\beta$ -carotene is further explored with respect to the influence of the vibrational energy of modes engaging in this radiationless electronic transition. For this, time-resolved transient gratings are employed which constitute a further third-order spectroscopic technique. Here, gratings of  $S_2$  state population are induced into solutions of  $\beta$ -carotene and the population flow in the  $S_1$  state is monitored by elastic Bragg scattering of a probe laser from the transient grating. In order to characterize the dynamics of vibrationally hot modes in the  $S_1$  state participating in the  $S_1/S_0$  internal conversion, the spectral position of the probe laser is shifted out of the red flank of the  $S_1$  state absorption. This makes the interrogation

of the population decay in these hot modes possible and allows for the influence of the vibrational energy on the rate with which this electronic transition takes place to be monitored.

The experimental work presented in the following chapters is aimed at presenting time-resolved, third-order spectroscopic methods as a powerful tool for addressing complex molecular problems such as the coupling of nuclear and electronic degrees of freedom. It is shown in the following that the utilization of Raman as well as optical resonances gives time-resolved, third-order optical spectroscopy a high selectivity with respect to the type of molecular dynamics observed in the transient signal.





# Chapter 2

## Theory

### 2.1 Time-Resolved, Third-Order Optical Spectroscopy

Time-resolved, four-wave mixing spectroscopy (FWM) in the form of coherent Raman techniques and photon echo has proven to be a powerful tool in the study of molecular dynamics.<sup>9,19,21,22,34</sup> The many degrees of freedom inherent to third-order optical processes allow for numerous aspects of elementary molecular dynamics to be explored. In the following, the formalism necessary for the description of third-order optical interactions is presented in a time-resolved scenario using third-order perturbation theory in the weak field limit.<sup>9,31–33,43–46</sup> Double-sided Feynman diagrams are presented to further illustrate the third-order interaction.<sup>21,47–49</sup> Specifically for this, degenerate four-wave mixing (DFWM), which constitutes the most general form of four-wave mixing, will first be presented by describing the interaction of the three pulsed laser fields, employed for this process, with an electronic two-state system. Here, the different states prepared in the molecular sample by the successive interaction of the three pulsed laser fields are described in order to demonstrate the role of each individual laser pulse and furthermore to present the relevant molecular states that are propagated in this third-order optical process. This general description will then be expanded to the coherent Raman techniques and transient gratings. The molecular states prepared, propagated and interrogated by introducing different scenarios of variable time delays between the laser pulses involved in these two forms of FWM will be discussed at the end of this chapter.

### 2.1.1 Perturbation Theory for Third-Order Interactions

In the following, third-order perturbation theory in the weak field limit is presented for the description of the FWM processes that are applied in the experimental work presented in chapters 4 and 5.<sup>9, 31–33, 45, 46</sup> In order to introduce the four-wave mixing process, degenerate four-wave mixing, (DFWM) will be presented in the framework of a two-level electronic system in this section. Here, the sequence of diagrams in Fig. 2.1 to 2.5 shows DFWM in the transient grating picture along with the potential energy scheme and the relevant double-sided Feynman diagrams. These three representations of the process will be discussed in order to introduce the formalism of third-order optical interactions.

The DFWM process is driven by the interaction of a molecular ensemble with the electric field,  $E_i(t)$  of three independent laser pulses with  $i = 1, 2, 3$ ,

$$\mathbf{E}_i(t) = \mathbf{E}_i f_i(t) e^{-i(\mathbf{k}_i \cdot \mathbf{x}_i - \omega_i t)} + c.c. \quad (2.1)$$

In the case of DFWM, the three pulses have the same angular frequency,  $\omega_1 = \omega_2 = \omega_3$ , that are in resonance to an optical transition in the molecular system. The laser pulses possess different spatial orientation in the sample described by the wave vectors  $\mathbf{k}_1 \neq \mathbf{k}_2 \neq \mathbf{k}_3$  that meet phase-matching conditions,  $\mathbf{k}_{\text{FWM}} = \mathbf{k}_1 - \mathbf{k}_2 + \mathbf{k}_3$ , where  $\mathbf{k}_{\text{FWM}}$  represents the wave vector of the coherent FWM signal. The considerations necessary for the phase-matching conditions of different FWM techniques are described in detail in section 3.2. Furthermore,  $f_i(t)$  is the temporal envelope function given by a Gaussian centered around  $t_i$ , which represents the relative time delay between the three lasers and  $\mathbf{E}_i$  represents the polarization vector. For the theoretical discussion of FWM in this chapter, the temporal profile of the laser pulses are assumed to be delta functions. The time point of interaction of the first pulse with the sample is defined as time zero with  $t_1 = 0$  and the other delay times are defined as  $\Delta t_{12} = t_2 - t_1$  and  $\Delta t_{23} = t_3 - t_2$ . The time-dependent perturbation of the molecular ensemble,  $W(t)$ , introduced by the electric field of the laser pulses, can be expressed with the interaction of the electric field with the transition dipole moment,  $\boldsymbol{\mu}$  of the system,

$$W(t) = -\boldsymbol{\mu} \cdot \mathbf{E}_i(t). \quad (2.2)$$

This allows for the formulation of the time-dependent Schrödinger equation for the electronic two level system as:

$$i\hbar \frac{\partial}{\partial t} |\Psi(t)\rangle = (H_0 + W(t)) |\Psi(t)\rangle \quad (2.3)$$

$$H_0 = \begin{pmatrix} (T + V_e) & 0 \\ 0 & (T + V_g) \end{pmatrix}. \quad (2.4)$$

Here,  $H_0$  represents the unperturbed Hamiltonian of the molecular system which is described by the kinetic energy  $T$ , and the potential energy  $V_g$  and  $V_e$  of the adiabatic electronic ground state and excited state of the two level system. Furthermore,  $|\Psi(t)\rangle$  is the total state vector of the molecular system. When considering an electronic two-level system, the total state vector can be fully described by the electronic ground state,  $|g(t)\rangle$  and the excited electronic state  $|e(t)\rangle$  which allows for the vector of  $|\Psi(t)\rangle$  and the matrix of the dipole moment,  $\mu_{eg}$  that couples the two adiabatic electronic states to be written as:

$$|\Psi(t)\rangle = \begin{pmatrix} |e(t)\rangle \\ |g(t)\rangle \end{pmatrix}; \quad \mu = \begin{pmatrix} 0 & \mu_{eg} \\ \mu_{ge} & 0 \end{pmatrix}. \quad (2.5)$$

According to time-dependent perturbation theory, an ansatz for the solution of the total state vector in equation 2.3 can be formulated as the sum of  $N$ -th order state vectors,  $|\Psi^{(N)}(t)\rangle$  that are generated by  $N$  perturbations through interactions with the electric field of a laser pulse,

$$|\Psi(t)\rangle = \sum_{N=0}^{\infty} |\Psi^{(N)}(t)\rangle. \quad (2.6)$$

In order to discuss the character of a  $N$ -th order state,  $|\Psi^{(N)}(t)\rangle$  each of the three successive interactions of the three laser pulses in the DFWM process with the molecular ensemble will be described individually along with the state  $|\Psi^{(N)}(t)\rangle$  that is prepared and propagated by the respective interaction.<sup>9,31,32,45,46</sup> For this discussion, double-sided Feynman diagrams will be used to illustrate the interactions with the ensemble and characterize the states that are propagated for each progressive interaction of a laser pulse with the molecular ensemble (Fig. 2.1 to 2.5).<sup>21,47,48</sup> The double-sided Feynman diagram consists of two vertical time lines describing the time evolution of the *bra*-state (right vertical line) and *ket*-state (left vertical line), where

time evolves by following the time lines from the bottom towards the top. Interactions with the electric field of a laser pulse are shown as diagonal arrows intersecting the time line at the time point of the interaction with the system. The arrows are labelled with the wave vector,  $\mathbf{k}_i$  of the laser pulse, that interacts with the system. Here, interactions that represent induced absorption processes have a positive slope while interactions describing induced emission processes are represented by arrows with a negative slope. The FWM signal is represented as an arrow with a wavy line.

### 2.1.2 Pulse 1: Induction and Propagation of a First-Order Polarization

In the Feynman diagram of Fig. 2.1, the first interaction of the molecular ensemble with the laser pulse,  $\mathbf{k}_1$  at  $t_1 = 0$  is shown, where an interaction with the unperturbed system generates the first-order state,  $|\Psi^{(1)}(t)\rangle = |e^{(1)}(t), \mathbf{k}_1\rangle$  via an absorption process that is coupled in phase to the electronic ground state  $|\Psi^{(0)}(t)\rangle = |g^{(0)}(t)\rangle$ .<sup>a</sup> This is also shown in Fig. 2.1 in the potential energy diagram of the electronic two-level system and furthermore, the propagation of the electric field of laser pulse  $\mathbf{k}_1$  through the sample space is represented in the plane wave approximation as light and dark regions that indicate the oscillations of the electric field along the direction of propagation,  $\mathbf{x}$  in a “binary fashion.” Once the laser pulse  $\mathbf{k}_1$  stops interacting with the system, the first-order polarization,  $P^{(1)}(t)$  that was induced in the sample by the laser field, develops in time. The expression for this polarization and with this the molecular states that are prepared and propagated by this first perturbation can be developed under consideration of equation 2.6:

$$P^{(1)}(t) = \langle \Psi(t) | \mu | \Psi(t) \rangle \quad (2.7)$$

$$P^{(1)}(t) = \left\langle \sum_{N=0}^1 \Psi^{(N)}(t) | \mu | \sum_{N'=0}^1 \Psi^{(N)}(t) \right\rangle \quad (2.8)$$

$$P^{(1)}(t) = \langle e^{(1)}(t, \mathbf{k}_1) | \mu | g^{(0)}(t) \rangle + cc. \quad (2.9)$$

<sup>a</sup>In the following, the time-dependent state vectors  $|g(t, r, R)\rangle$  and  $|e(t, r, R)\rangle$ , which are a functions of time,  $t$ , the electronic coordinates,  $r$  and the nuclear coordinates,  $R$ , will be noted as  $|\psi^{(N)}(t, \mathbf{k}_i)\rangle$ , where the spatial coordinates are omitted for simplicity, the superscript in parenthesis,  $(N)$  denotes the order of perturbation of the states and the wave vector,  $\mathbf{k}_i$  symbolizes the laser pulse,  $i$  that prepares the respective state.

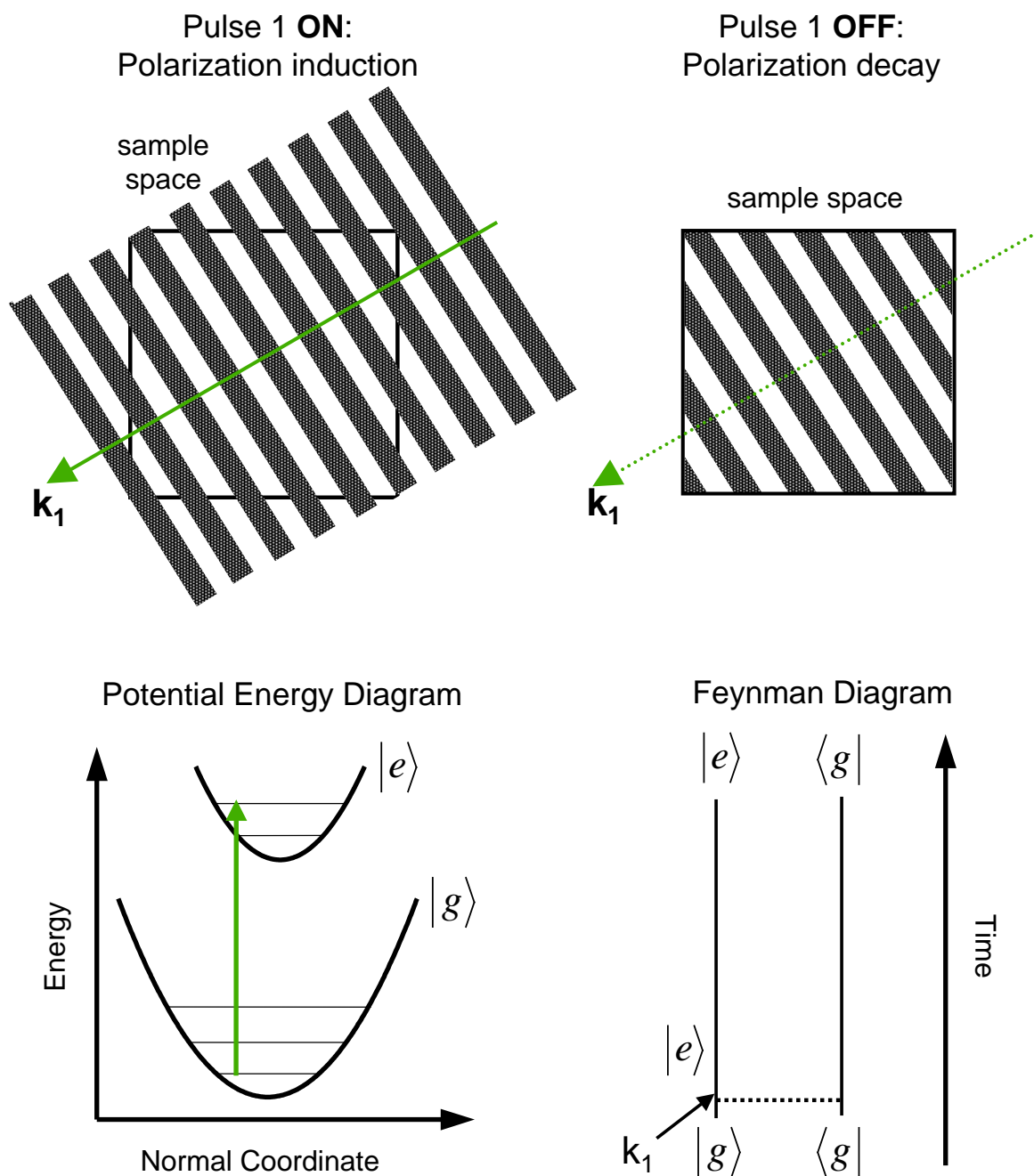


Figure 2.1: Interaction of the first of three laser pulses in the DFWM process, ( $\mathbf{k}_1$ ) represented by the transient grating picture in the sample space, a potential energy diagram of the respective molecular system and a double-sided Feynman diagram. Details concerning the formalism of these representations can be found in the text.

The diagonal elements in equation 2.8,  $(\langle e^{(1)}(t, \mathbf{k}_1) | \mu | e^{(1)}(t, \mathbf{k}_1) \rangle$  and  $\langle g^{(0)}(t) | \mu | g^{(0)}(t) \rangle$  vanish since the matrix of the transition dipole moment in equation 2.5 does not contain diagonal elements. This simplifies the expression to equation 2.9. With this, the polarization is characterized by the development of the electronic ground and excited state in time, which can be seen by following the time lines of the *bra* and *ket* in the respective double-sided Feynman diagram (Fig. 2.1), that show the evolution of these two states parallel to one another. Since the polarization is prepared by an optically coherent laser pulse the ground and excited electronic states are coupled in their phase. The phase-coupled time evolution of these states can be seen clearly by separating the time-dependent from time-independent terms of the polarization. For the electronically excited state,  $|e^{(1)}(t, \mathbf{k}_1)\rangle$ , the time-dependent terms consist of the time-dependent phase factor,

$$\vartheta_e(t) = e^{-i(E_e t/\hbar) + \phi_e(t)} \quad (2.10)$$

and a time-dependent coefficient,  $c_e(t)$  of the stationary state,  $|e^{(1)}\rangle$ ,

$$c_e(t) = c_e(0)e^{-t/2T_{1,e}}. \quad (2.11)$$

Here  $c_e(0)$  is the coefficient at  $t = 0$  and  $T_{1,e}$  is the time-constant that describes the lifetime of the excited state.<sup>b</sup>

$$\begin{aligned} |e(t, \mathbf{k}_1)\rangle &= \vartheta_e(t) \cdot c_e(t) \cdot |e^{(1)}\rangle \\ |e(t, \mathbf{k}_1)\rangle &= e^{-i(E_e t/\hbar) + \phi_e(t)} \cdot c_e(0)e^{-t/2T_{1,e}} |e^{(1)}\rangle. \end{aligned} \quad (2.12)$$

The electronic ground state,  $|g^{(0)}(t)\rangle$  can be treated in an analog fashion. Using this type of expansion for the electronic ground and excited state to develop the expression for the first-order polarization in equation 2.9 gives,

$$P^{(1)}(t) = e^{-i(E_e t/\hbar) + \phi_e(t)} \cdot e^{i(E_g t/\hbar) + \phi_g(t)} \cdot c_e^*(0)e^{-t/2T_{1,e}} \cdot c_g(0)e^{-t/2T_{1,g}} \cdot \langle g^{(0)} | \mu | e^{(1)} \rangle + cc. \quad (2.13)$$

The time-constant for the total dephasing,  $T_2$  can be defined by unifying all the time constants in the exponential terms of equation 2.13. This includes  $T_1$  from the

---

<sup>b</sup>stationary state vectors,  $|e(r, R)\rangle$  and  $|g(r, R)\rangle$  are denoted as  $|\psi^{(N)}\rangle$ , where the electronic and nuclear coordinates,  $r$  and  $R$  are omitted for simplicity and the superscript in parenthesis,  $N$  denotes the order of perturbation.

time-dependent coefficients,  $c_e^*(t)$  and  $c_g(t)$  in equation 2.11, and the phases,  $\phi_i(t)$  in the time-dependent phase factor,  $\vartheta_i(t)$  of equation 2.10. The phenomenological damping due to the loss in the phase relationship, given by  $\phi_i(t)$ , is described by the time constant for the pure dephasing  $T_2^*$ . This loss of coherence is the result of interactions of the molecular system with the environment such as collisions. These interactions cause fluctuations in the energy of the molecular states and lead to a non-periodic development of the phase factor,  $\vartheta_i(t)$  as time evolves which is described by varying values for  $\phi_i(t)$  as a function of time. With these two damping mechanisms of the coherence, the time constant  $T_2$  for the total dephasing time is defined as:<sup>50</sup>

$$\frac{1}{T_2} = \frac{1}{2(T_{1g} + T_{1e}) + T_2^*} \quad (2.14)$$

By using the definition for  $T_2$  to simplify equation 2.13, the behavior of the polarization as time develops after the first laser pulse,  $\mathbf{k}_1$  can be written as:

$$P^1(t) = e^{-t/T_2} \cdot e^{-i(\Delta E_{eg}t/\hbar)} \cdot c_g^*(0) \cdot c_e(0) \cdot \langle g^{(0)} | \mu | e^{(1)} \rangle + cc. \quad (2.15)$$

As time evolves after the first pulse, the induced polarization is dampened with the total dephasing time,  $T_2$  which unifies the population relaxation time,  $T_1$  from the coefficients  $c_i(t)$  of the respective electronic states and the phase relaxation,  $T_2^*$ , that describes the loss of the phase relationship between the two electronic states through interactions with the environment.<sup>21, 50-52</sup> Furthermore, the second term in equation 2.15 shows that the polarization oscillates with the angular frequency ( $\omega_{eg} = \Delta E_{eg}/\hbar$ ) that is resonant to the angular frequency,  $\omega_1$  of the laser pulse that induces the polarization. This can be observed as an emission of a coherent optical wave in direction  $\mathbf{k}_1$  from the sample after the laser pulse has stopped interacting with the sample.<sup>51</sup>

### 2.1.3 Pulse 2: Formation and Propagation of a Population Grating

Figures 2.2 and 2.3 show the two possible scenarios when the second laser pulse,  $\mathbf{k}_2$  interacts with the polarization prepared by the first perturbation of the system. For both scenarios, the transient grating picture shows the importance of considering the pure dephasing of the phase coupled states in the first-order polarization, described

by  $T_2^*$ . Since the second pulse transverses the sample space with a different spatial orientation, described by  $\mathbf{k}_2$ , a phase sensitive interference pattern, which is referred to as an optical grating, is induced in the sample space (see top of Fig. 2.2 and 2.3).<sup>53</sup> In the phase-sensitive interference of the first-order polarization generated by pulse  $\mathbf{k}_1$  and the electric field of pulse  $\mathbf{k}_2$ , two possible states can be prepared. In the first case, the second laser pulse,  $\mathbf{k}_2$  transfers electronically excited state molecules back into the ground state through an induced emission. This prepares the second-order state  $|g^{(2)}(t)\rangle$  which is described by the potential energy scheme and the Feynman diagram in Fig. 2.2. In the second case, that takes place parallel to this induced emission, the potential energy scheme and the Feynman diagram in Fig. 2.3 illustrate the second laser pulse,  $\mathbf{k}_2$  pumping molecules from  $|g^{(0)}(t)\rangle$  into the electronically excited state through an absorption process. This prepares the first-order state  $|e^{(1)}(t)\rangle$ . The complete description of the second-order polarization,  $P^{(2)}(t)$  expanded according to equation 2.6 includes the expression for both scenarios described above,

$$P^{(2)}(t) = \langle e^{(1)}(t, \mathbf{k}_2) | \mu | e^{(1)}(t, \mathbf{k}_1) \rangle + \langle g^{(0)}(t) | \mu | g^{(2)}(t, \mathbf{k}_1, \mathbf{k}_2) \rangle + cc. = 0. \quad (2.16)$$

The equation above shows that a second-order polarization cannot be induced in an electronic two-level system in a centro-symmetric environment since symmetry considerations make all the elements in equation 2.16 go to zero. Due to this, the states prepared by  $\mathbf{k}_1$  and  $\mathbf{k}_2$  cannot be observed via a coherent emission from the sample.

Despite this, the time evolution of states prepared by  $\mathbf{k}_1$  and  $\mathbf{k}_2$  can be analyzed by developing the expressions for the time-dependent probability,  $\mathcal{W}(t)$  of these states.<sup>43,44,46</sup> For the second case, the Feynman diagram in Fig. 2.3 shows the phase coupled evolution of two first-order excited states prepared by pulses  $\mathbf{k}_1$  and  $\mathbf{k}_2$ , respectively. The propagation of the probability in the time after pulse  $\mathbf{k}_2$  interacts with the sample at  $\Delta t_{12} = t_2 - t_1$  can be expanded according to equation 2.12:

$$\mathcal{W}_e(t) = \langle e^{(1)}(t, \mathbf{k}_2) | e^{(1)}(t, \mathbf{k}_1) \rangle \quad (2.17)$$

$$\mathcal{W}_e(t) = e^{-t/2T_{1e}} e^{-(t+\Delta t_{12})/2T_{1e}} \cdot c_e^*(0)c_e(0) \cdot \langle e^{(1)} | e^{(1)} \rangle + cc. \quad (2.18)$$

$$\mathcal{W}_e(t) = e^{-t/T_{1e}} e^{-\Delta t_{12}/2T_{1e}} \cdot c_e^*(0)c_e(0) \cdot \langle e^{(1)} | e^{(1)} \rangle + cc. \quad (\text{for } t > \Delta t_{12}) \quad (2.19)$$

In this expansion the time-dependent phase factors,  $\vartheta(t)$  can be neglected since the identical phase velocity of  $|e^{(1)}(t, \mathbf{k}_1)\rangle$  and  $|e^{(1)}(t, \mathbf{k}_2)\rangle$  cause these terms to cancel



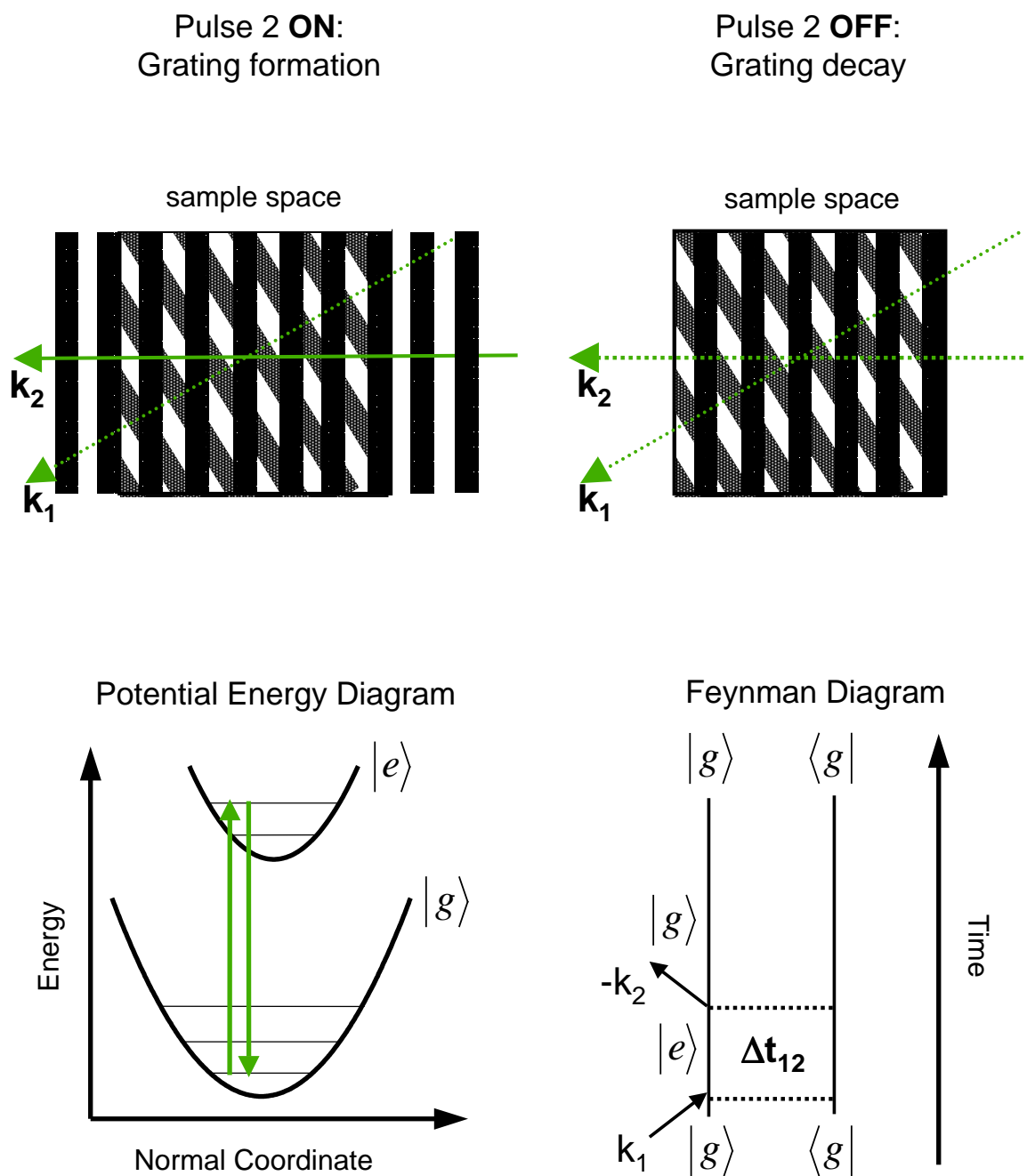


Figure 2.2: Interaction of the second of three laser pulses in the DFWM process, ( $\mathbf{k}_2$ ) represented by the transient grating picture in the sample space, a potential energy diagram of the respective molecular system and a double-sided Feynman diagram. The representations show one of the two possible scenarios for the interaction of ( $\mathbf{k}_2$ ) with the sample. Details concerning the formalism of these representations can be found in the text.

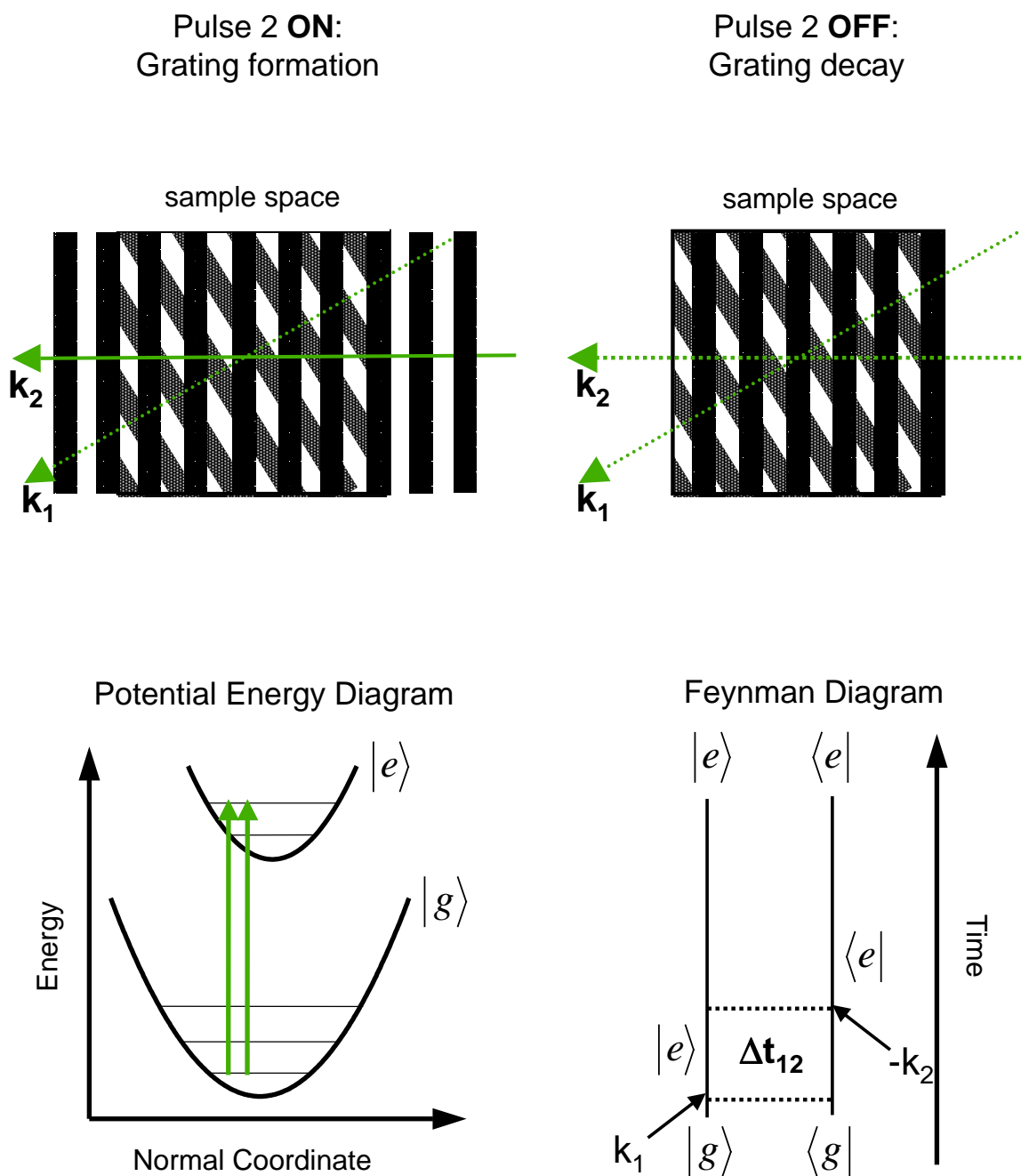


Figure 2.3: Interaction of the second of three laser pulses in the DFWM process, ( $\mathbf{k}_2$ ) represented by the transient grating picture in the sample space, a potential energy diagram of the respective molecular system and a double-sided Feynman diagram. The representations show one of the two possible scenarios for the interaction of ( $\mathbf{k}_2$ ) with the sample. Details concerning the formalism of these representations can be found in the text.

out due to the complex conjugation. Here, the time-dependent coefficient of the respective states are unified in equation 2.19 according to:

$$c_e^*(t)c_e(t) = c_e^*(0)c_e(0) \cdot e^{-t/T_{1e}} e^{-\Delta t_{12}/2T_{1e}}. \quad (2.20)$$

The second exponential term describes the population decay of the state prepared by  $\mathbf{k}_1$  in the time,  $0 < t < \Delta t_{12}$ . This factor becomes time-independent for a fixed value of  $\Delta t_{12}$ . Equation 2.19 shows that the time evolution of the population for the time  $t > \Delta t_{12}$  is given by the decay of the population in the electronically excited state, described by  $T_{1e}$ . Analog considerations can be made for probability density of the second order state  $|g^{(2)}(t)\rangle$  evolving with  $|g^{(0)}(t)\rangle$ .

$$\mathcal{W}_g(t) = \langle g^{(0)}(t) | g^{(2)}(t, \mathbf{k}_1, \mathbf{k}_2) \rangle \quad (2.21)$$

$$\mathcal{W}_g(t) = e^{-t/2T_{1g}} e^{-(t+\Delta t_{12})/2T_{1g}} \cdot c_g^*(0)c_g(0) \cdot \langle g^{(0)} | g^{(2)} \rangle + cc. \quad (2.22)$$

$$\mathcal{W}_g(t) = e^{-t/T_{1g}} e^{-\Delta t_{12}/2T_{1g}} \cdot c_g^*(0)c_g(0) \cdot \langle g^{(0)} | g^{(2)} \rangle + cc. \quad (for\ t > \Delta t_{12}) \quad (2.23)$$

The transient grating picture in Fig. 2.2 and 2.3 can give further insight into the state prepared by the second laser pulse  $\mathbf{k}_2$ . Here, it can be seen that the optical grating formed by the polarization induced by  $\mathbf{k}_1$  and the electric field of  $\mathbf{k}_2$  will show regions of constructive and destructive interference in the sample space. In the regions of constructive interference, the high field intensity will lead to a high yield in population difference between the electronic ground and excited state while regions of destructive interference will show a low yield. This means, the optical grating translates to a repetitive modulation of the population difference between electronic ground and excited state in the sample space, which is referred to as a population grating.<sup>34,53,54</sup> As shown in equation 2.19 and 2.23, this grating will decay with the population difference between the electronic excited and ground state, described by the time constant  $T_1$ .

### 2.1.4 Pulse 3: Induction of a Third-Order Polarization and Bragg Scattering

The interaction of the third pulse  $\mathbf{k}_3$  at  $t = t_3$  with the population grating described above will again lead to a polarization of the sample. This third-order polarization,  $P^{(3)}(t)$  can be induced through the interaction of  $\mathbf{k}_3$  with either the first-order excited state  $|e^{(1)}(t, \mathbf{k}_2)\rangle$  prepared by  $\mathbf{k}_2$  or the second-order ground state

$|g^{(2)}(t, \mathbf{k}_1, \mathbf{k}_2)\rangle$  prepared by  $\mathbf{k}_1$  and  $\mathbf{k}_2$ . These two scenarios are shown in the Feynman diagrams of Fig. 2.4 and 2.5, and can be correlated to the two terms that describe the third-order polarization induced by  $\mathbf{k}_3$ :

$$P^3(t) = \langle e^{(1)}(t, \mathbf{k}_2, \mathbf{k}_3) | \mu | g^{(2)}(t, \mathbf{k}_1) \rangle + \langle g^{(0)}(t) | \mu | e^{(3)}(t, \mathbf{k}_1, \mathbf{k}_2, \mathbf{k}_3) \rangle + cc. \quad (2.24)$$

This polarization can be observed as a coherent emission which constitutes the DFWM signal in the phase-matched direction  $\mathbf{k}_{DFWM} = \mathbf{k}_1 - \mathbf{k}_2 + \mathbf{k}_3$ . The time-development of  $P^{(3)}(t)$  can be described analog to  $P^{(1)}(t)$  in equation 2.15 but this expansion is not relevant for the experiments presented in this work, since the intensity of the DFWM signal,  $I_{DFWM}$  in the phase-matched direction is detected with a quadrature detector by integrating over the full temporal response after pulse  $\mathbf{k}_3$  has interacted with the sample at  $t = t_3$ .<sup>31,32,45,46</sup>

$$I_{DFWM} \propto \int_{t_3}^{\infty} |P^{(3)}(t)|^2 dt. \quad (2.25)$$

Again, the transient grating model in Fig. 2.4 and 2.5 gives a picture of the induction of a coherent emission from  $P^{(3)}(t)$  that allows for further understanding of the state prepared by  $\mathbf{k}_3$ . Here, the interaction of pulse  $\mathbf{k}_3$  with the sample is described as a scattering of  $\mathbf{k}_3$  off the population grating prepared by pulses  $\mathbf{k}_1$  and  $\mathbf{k}_2$ . Since the scattering takes place off a grating structure in the sample space, a coherent wave front can propagate out of the sample in an angle,  $\theta$  relative to the grating that satisfies the Bragg conditions  $\lambda_3 = 2a \cdot \sin \theta$ , where  $a$  gives the spatial distance between two points in the grating and  $\lambda_3$  the wavelength of  $\mathbf{k}_3$ .<sup>53</sup>

## Summary

The role of the three laser pulses  $\mathbf{k}_1$ ,  $\mathbf{k}_2$  and  $\mathbf{k}_3$  in the DFWM process and the states prepared and propagated by the interaction of these laser pulses with the sample have been developed above in order to introduce time-resolved FWM. It was shown that the interaction of three laser pulses offer two time windows for allowing the molecular dynamics to develop in time, which is illustrated in Fig. 2.6. In the time window,  $\Delta t_{12} = t_2 - t_1$  between pulse  $\mathbf{k}_1$  and  $\mathbf{k}_2$ , the first-order polarization develops in time which is characterized by equation 2.15 with a damping according to the total dephasing time,  $T_2$ . A variable delay time,  $\Delta t_{12}$  with a fixed delay time between pulse  $\mathbf{k}_2$  and  $\mathbf{k}_3$  allows for the evolution of  $P^{(1)}(t)$  to be observed directly in the

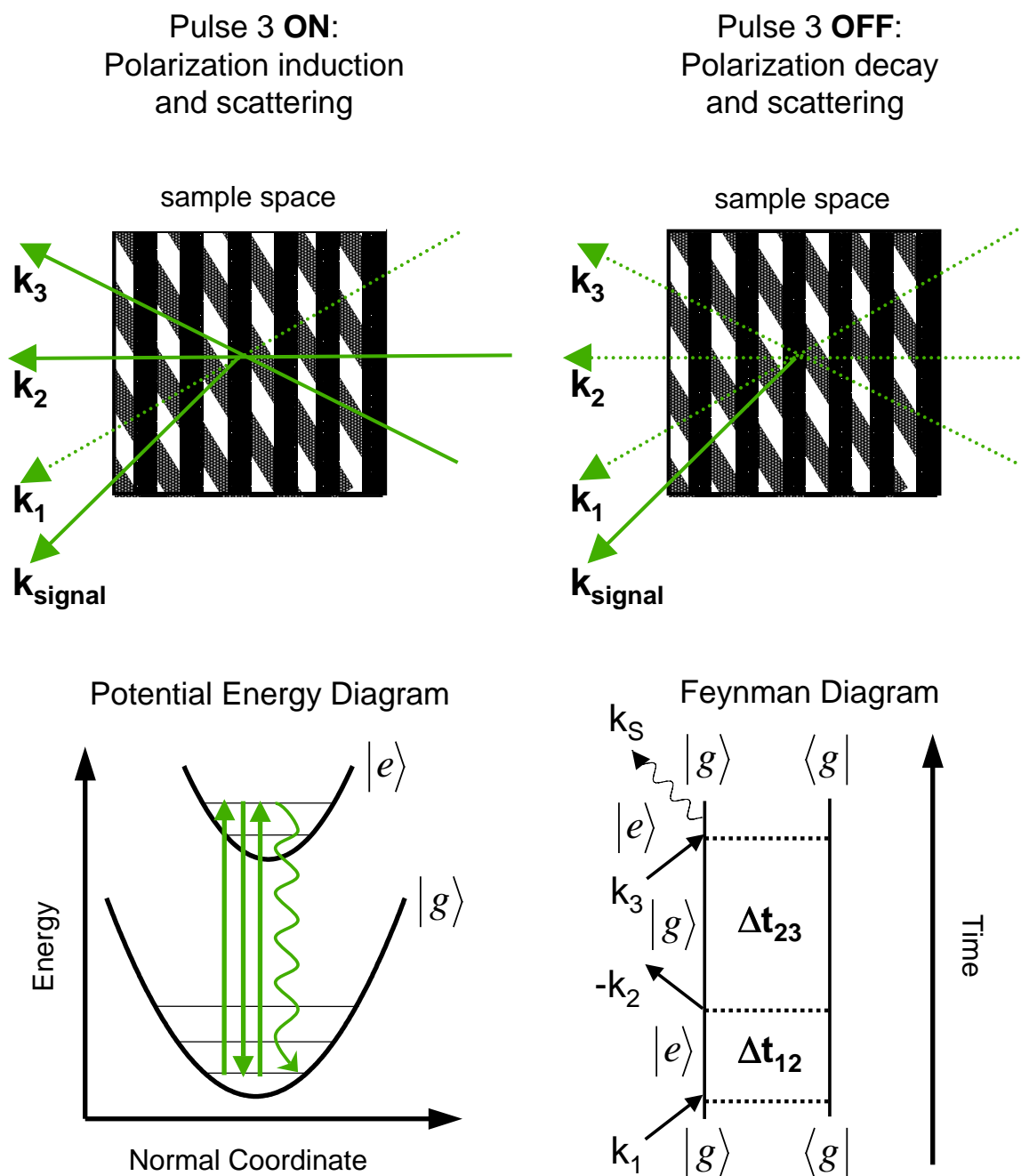


Figure 2.4: Interaction of the third of three laser pulses in the DFWM process, ( $\mathbf{k}_3$ ) represented by the transient grating picture in the sample space, a potential energy diagram of the respective molecular system and a double-sided Feynman diagram. The representations show one of the two possible scenarios for the interaction of ( $\mathbf{k}_3$ ) with the sample. Details concerning the formalism of these representations can be found in the text.

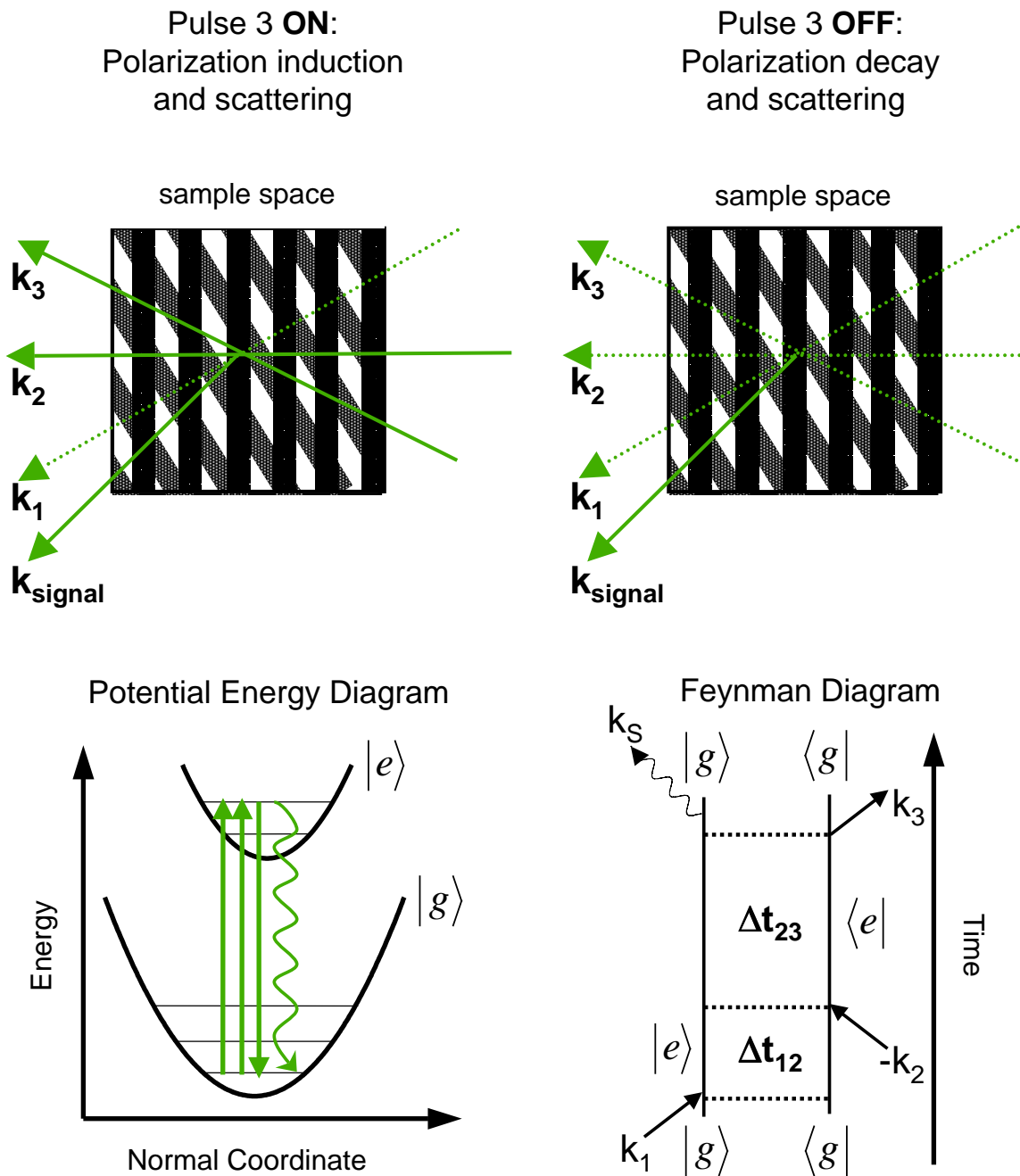


Figure 2.5: Interaction of the third of three laser pulses in the DFWM process, ( $\mathbf{k}_3$ ) represented by the transient grating picture in the sample space, a potential energy diagram of the respective molecular system and a double-sided Feynman diagram. The representations show one of the two possible scenarios for the interaction of ( $\mathbf{k}_3$ ) with the sample. Details concerning the formalism of these representations can be found in the text.

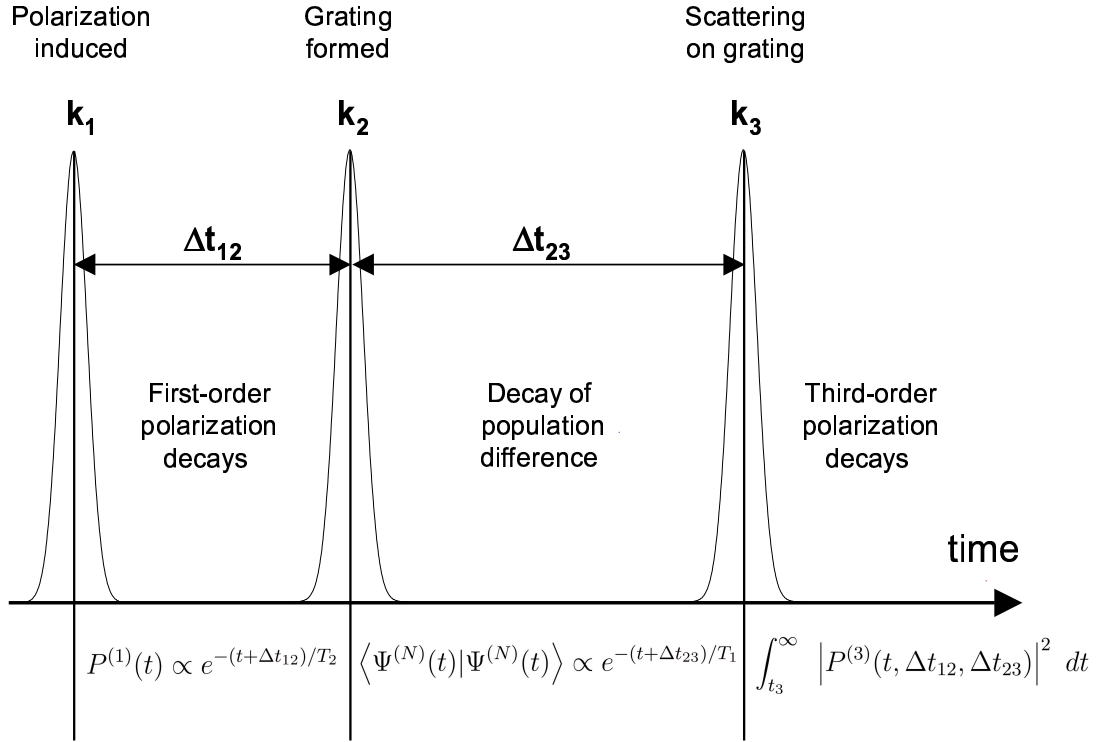


Figure 2.6: Schematic representation of the temporal sequence of the three laser pulses involved in the DFWM process ( $\mathbf{k}_1, \mathbf{k}_2, \mathbf{k}_3$ ), separated by the delay times,  $\Delta t_{12}$  and  $\Delta t_{12}$ , respectively. The figure shows the states prepared by each pulse and the relaxation processes that take place in the time that separates the pulses.

analog behavior of  $P^{(3)}(\Delta t_{12})$  integrated over time in the phase-matched direction  $\mathbf{k}_{\text{DFWM}} = \mathbf{k}_1 - \mathbf{k}_2 + \mathbf{k}_3$ . It must be mentioned, that for these phase matching conditions, the damping of the first-order polarization according to  $T_2$  only holds true for a homogeneous ensemble. In the case of an inhomogeneous ensemble, the first-order polarization will dephase much faster if the spectral bandwidth of the laser pulses is large enough to cover the inhomogeneous linewidth of the respective transition. Assuming an inhomogeneous ensemble with a Gaussian distribution, the first-order polarization will dephase quadratically with time constant  $T_2'$  described by:

$$P^{(1)}(t) \propto e^{-2t/T_2'}. \quad (2.26)$$

This is due to the superposition of states within the inhomogeneous ensemble, encompassed by the spectral profile of the laser pulses, that possess slightly different

phase velocities. This problematic can be solved with a different phase-matching,  $\mathbf{k}_{\text{DFWM}} = -\mathbf{k}_1 + \mathbf{k}_2 + \mathbf{k}_3$ , which is used in photon echo experiments. Here, the phase-conjugation of  $-\mathbf{k}_1$  and  $\mathbf{k}_3$  allows for the inhomogeneous part of the phase development, taking place after  $-\mathbf{k}_1$ , to be rephased by  $\mathbf{k}_3$ . With this, it is possible to determine the homogeneous, total dephasing time,  $T_2$  despite the presence of an inhomogeneous ensemble. A precise description of this technique will not be given here since these phase-matching conditions were not applied in this work. Detailed descriptions of the photon echo technique can be found in the literature.<sup>19,21,34,52</sup>

The second time window available to DFWM experiments,  $\Delta t_{23} = t_3 - t_2$  allows for the population gratings prepared by  $\mathbf{k}_1$  and  $\mathbf{k}_2$  to develop in time. This is the time window that will primarily be utilized in the experiments presented in this work. The development of a transient population grating in time is described by equation 2.19 and 2.23, where the population flow is given by the time constant  $T_1$ . This development of a transient population can be observed in the analog behavior in  $P^{(3)}(\Delta t_{23})$  integrated over time after the interaction of the ensemble with  $\mathbf{k}_3$ , as shown in Fig. 2.6.

In this introduction to the FWM process, the molecular system was simplified to a electronic two-level system. In section 2.3.1, the influence of the vibrational structure in the participating electronic states, on the third-order polarization will be discussed in the framework of a wave packet formalism. This is relevant for the experiments presented in this work since the broadband nature of the femtosecond pulses allows for the coherent superposition of multiple vibrational eigenstates within an electronic potential.

## 2.2 Classification of Four-Wave Mixing Techniques

Degenerate four-wave mixing (DFWM) was used in the previous section for the introduction of the FWM scheme. In this general form of the FWM, all the laser pulses possess the same frequency making them indistinguishable in their temporal sequence, apart from their phase-conjugation. By introducing different color schemes into the FWM process, the pulses become differentiable, allowing for the variation of their temporal sequence as well as the phase-matching conditions in the FWM process. This makes the selective preparation and probing of different molecular states



possible. The time sequence and beam geometry in a multi-color FWM scheme allows for the classification of the two general categories of FWM, which are the coherent Raman techniques and virtual photon echos.<sup>21,54</sup> In the following two sections, the coherent Raman techniques in the form of coherent anti-Stokes Raman scattering (CARS) and coherent Stokes Raman scattering (CSRS) as well as virtual photon echo in the form of transient gratings (TG) will be introduced by presenting the color scheme and the role of the different colored lasers in their temporal sequence. The three laser pulses which were introduced as  $\mathbf{k}_1$ ,  $\mathbf{k}_2$  and  $\mathbf{k}_3$  in the DFWM process are labelled according to their function in these two forms of FWM as *pump*, *Stokes* and *probe* lasers. Furthermore, the specific molecular state that can be characterized with these two techniques will be presented by showing how the molecular dynamics are propagated and monitored in the respective transient signal.

### 2.2.1 Time-Resolved Coherent anti-Stokes Raman Scattering

In Fig. 2.7, the optical processes associated with time-resolved coherent anti-Stokes Raman scattering (CARS) are shown in potential energy diagrams along with the relevant double-sided Feynman diagrams for this FWM process.<sup>28,30,31,45,46,55-57</sup> The potential energy diagrams in this figure, show the CARS process consisting of two lasers ( $\mathbf{k}_1$ ,  $\mathbf{k}_3$ ) possessing the same color, which are referred to as *pump*-lasers and a third pulse ( $\mathbf{k}_2$ ) which is red-shifted in color relative to the *pump*-lasers and referred to as the *Stokes* laser. In the case of *resonance*-CARS, the *pump* lasers are tuned to be resonant with an electronic transition in the molecular system, while the *Stokes* laser is tuned so that the energy difference,  $\Delta\omega = \omega_{pu} - \omega_S$  corresponds to the energy of a Raman transition in the electronic ground state as shown in Fig. 2.7.<sup>55,58,59</sup> In the time-resolved CARS scheme applied in this work, one of the *pump* pulses ( $\mathbf{k}_1$ ) and the *Stokes* pulse ( $\mathbf{k}_2$ ) interact simultaneously with the molecular sample. The interaction of the second *pump* pulse,  $\mathbf{k}_3(\Delta t)$  with the sample is varied in time relative to the *pump*/*Stokes* pulse pair. The timing of the second *pump* pulse is described by the parametric delay time,  $\Delta t$ .

For the case that the *pump*/*Stokes* pulse pair interacts first with the sample ( $\Delta t > 0$ ), three possible Feynman diagrams can be formulated that lead to the formation of a third-order polarization (**A-C** in Fig. 2.7). Experimental works in the

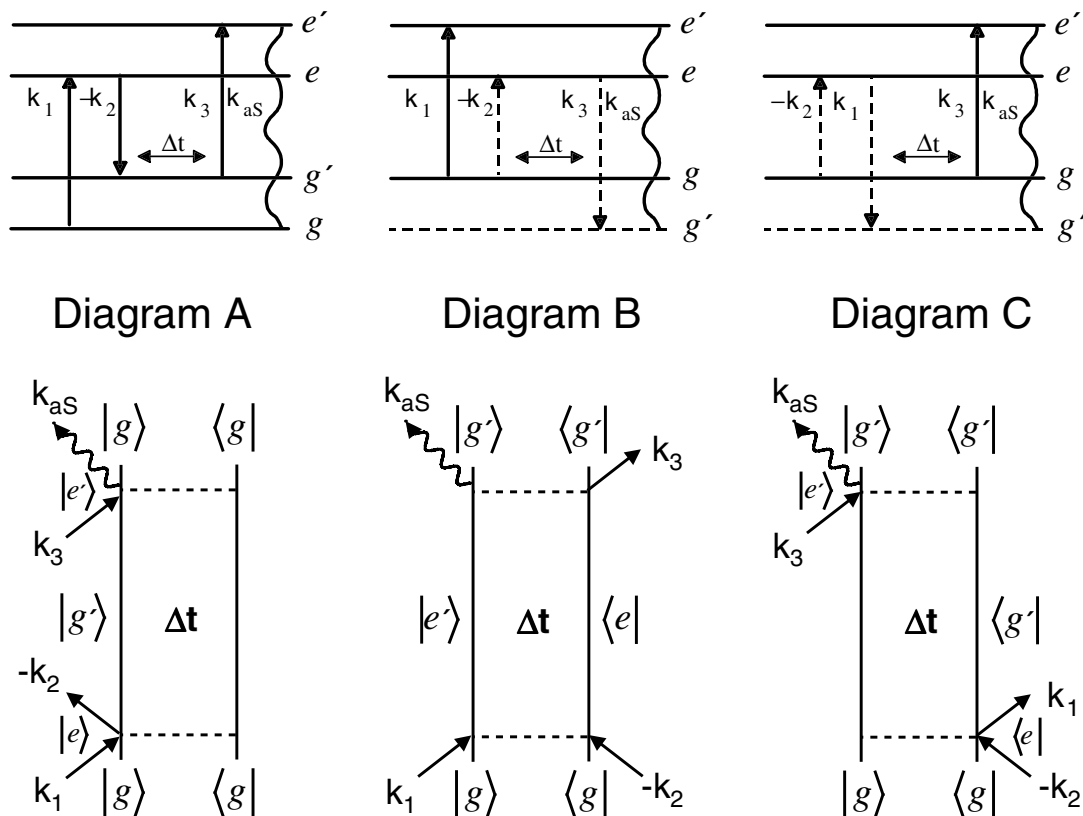


Figure 2.7: Diagrams **A-C** show three possible optical processes in the color scheme of a CARS experiment in a schematic potential energy diagram (top), and double-sided Feynman diagram (bottom) representation. Diagram **A** shows a process that is in full resonance with molecular states (solid horizontal lines), while diagrams **B** and **C** utilize virtual states (dashed horizontal lines)

literature and results presented in this work, as well as theoretical considerations, show that diagram **A** describes the optical process that primarily contributes to the third-order polarization in the color scheme of CARS while the contribution of the processes described by diagram **B** and **C** can be neglected.<sup>28-32,56,57</sup> Briefly, the selection of diagrams that contribute to the CARS signal is founded in the necessity of processes described by diagrams **B** and **C** to utilize virtual states rather than being in full resonance to the quantum states offered by the respective molecular system. The lack of the Raman resonance makes processes of this type ineffective and therefore, they do not contribute significantly to the CARS signal intensity. Diagram **A** shows

the only process that is in resonance to the molecular states of the system in all four optical transitions and will therefore primarily describe the CARS process. Here, the interaction of the *pump* ( $\mathbf{k}_1$ ) and *Stokes* pulse ( $\mathbf{k}_2$ ) projects the initial ensemble  $|g^{(0)}\rangle$  into an excited vibrational state in the electronic ground state  $|g'^{(2)}\rangle$ , via the electronically excited state  $|e^{(1)}\rangle$ .<sup>c</sup> This state develops in time until the second *pump* pulse ( $\mathbf{k}_3$ ) probes this state at a parametric delay time,  $\Delta t$ . The probing of this state is realized by projecting it into a vibrationally excited state in the excited electronic state,  $|e^{(3)}\rangle$  and thereby inducing the third-order polarization between this state and  $|g^{(0)}\rangle$  that has developed in time during  $\Delta t$ . As shown in the potential energy diagram describing the CARS process and the Feynman diagram **A** (Fig. 2.7), the third-order polarization is given by the anti-Stokes transition,  $\mathbf{k}_{as}$  which is blue shifted relative to the wavelength of the *pump* lasers and described by the transition dipole moment,  $\mu_{aS}$ :

$$P^{(3)}(\Delta t) = \langle g^{(0)}(\Delta t) | \mu_{aS} | e^{(3)}(\Delta t) \rangle + cc. \quad (2.27)$$

Here,  $|e^{(3)}(\Delta t)\rangle$  results out of the interaction of  $|g'^{(2)}(\Delta t)\rangle$  and the electric field of the time-variable *pump* pulse  $E_{pu}$  at  $\Delta t$ :

$$P^{(3)}(\Delta t) = \langle g^{(0)}(\Delta t) | \mu_{aS} | (\mu E_{pu}(\Delta t) | g'^{(2)}(\Delta t) \rangle) \rangle + cc. \quad (2.28)$$

$$P^{(3)}(\Delta t) = \langle g^{(0)}(\Delta t) | \mu_{aS} | e' \rangle \langle e' | \mu E_{pu}(\Delta t) | g'^{(2)}(\Delta t) \rangle + cc. \quad (2.29)$$

The identity operator,  $|e'\rangle \langle e'|$  is used to expand the expression in equation 2.28. The influence in the development of the population grating of coherent Raman modes in the ground state potential on the CARS signal as a function of the delay time,  $\Delta t$  between the *pump*/*Stokes* pulse pair and the time variable *pump* pulse can be seen when the time-dependent coefficients  $c_g^*(\Delta t)$  and  $c_{g'}(\Delta t)$  for  $|g^{(0)}(\Delta t)\rangle$  and  $|g'^{(2)}(\Delta t)\rangle$ , are expanded out of the integration over the stationary terms in analogy to the description of the first-order polarization in equations 2.13 and 2.15 in section 2.2.1. For this, the coefficients are expanded according to:

$$c_g^*(\Delta t) c_{g'}(\Delta t) = c_g^*(0) c_{g'}(0) e^{-(t+\Delta t)/2(T_{1,g} + T_{1,g'})}. \quad (2.30)$$

<sup>c</sup>In the following, the explicit notation of state vectors as a function of time is omitted for simplicity. The states that develop in time from  $t = 0$  to  $t = \Delta t$  are noted as a function of the *parametric delay time*,  $\Delta t$ . The time evolution of these states are derived by  $|\psi(t = \Delta t)\rangle = U(0, \Delta t) |\psi(t = 0)\rangle$ , where  $U(0, \Delta t)$  represents the propagation operator that develops the state from  $t = 0$  to  $t = \Delta t$ .<sup>44</sup> Furthermore, states denoted with a prime, represented excited vibrational states within the particular electronic state (or in the case of a process that does not fulfill a Raman resonance the prime denotes a virtual state).

The time constant for the total dephasing,  $T_2$  gives the unified time constants for the lifetime of the excited vibrational states,  $T_1$  and the time constant for the phenomenological loss of phase coherence,  $T_2^*$  between the respective coherent states,

$$\frac{1}{T_2} = \frac{1}{2(T_{1,g} + T_{1,g'})} + \frac{1}{T_2^*}. \quad (2.31)$$

By using the definitions above to expand the third-order polarization in equation 2.29, the expression for the coherent anti-Stokes signal as a function of the parametric delay time,  $\Delta t$  can be developed as follows:

$$\begin{aligned} I_{CARS}(\Delta t) &= \int_{t_3}^{\infty} |P^{(3)}(t, \Delta t)|^2 dt \\ &= \int_{t_3}^{\infty} \left| \langle c_g^*(\Delta t) g^{(0)} | \mu_{aS} | e' \rangle \langle e' | \mu E_{pu}(\Delta t) | c_{g'}(\Delta t) g'^{(2)} \rangle \right|^2 dt \\ &= \int_{t_3}^{\infty} \left| \langle c_g^*(0) e^{-(t+\Delta t)/2T_{1,g}} g^{(0)} | \mu_{aS} | e' \rangle \langle e' | \mu E_{pu}(\Delta t) | c_{g'}(0) e^{-(t+\Delta t)/2T_{1,g'}} g'^{(2)} \rangle \right|^2 dt \\ &= \int_{t_3}^{\infty} \left| c_g^*(0) c_{g'}(0) e^{-\Delta t/T_2} \cdot \langle e^{-t/2T_{1,g}} g^{(0)} | \mu_{aS} | e' \rangle \langle e' | \mu E_{pu}(\Delta t) | e^{-t/2T_{1,g'}} g'^{(2)} \rangle \right|^2 dt \\ &= |c_g^*(0) c_{g'}(0) e^{-\Delta t/T_2}|^2 \cdot \int_{t_3}^{\infty} \left| \langle e^{-t/2T_{1,g}} g^{(0)} | \mu_{aS} | e' \rangle \langle e' | \mu E_{pu}(\Delta t) | e^{-t/2T_{1,g'}} g'^{(2)} \rangle \right|^2 dt. \end{aligned} \quad (2.32)$$

When the integration over time,  $t$  is carried out from  $t_3$  to infinity and the stationary term from the integration is represented by an amplitude factor,  $A$  the proportionality of the CARS intensity to the square of the dephasing of the Raman modes in the electronic ground state can be seen:

$$I_{CARS}(\Delta t) = |A \cdot c_g^*(0) c_{g'}(0)|^2 e^{-2\Delta t/T_2}. \quad (2.33)$$

With this, the CARS signal monitors the development in the coherence of ground state vibrational modes as function of the parametric delay time,  $\Delta t$ . The description of the CARS process given above can further be illustrated by applying the transient grating picture to the time-resolved CARS process. Here, the interaction of the *pump/Stokes* pulse pair with the molecular system prepares a grating of Raman modes. The relaxation of this grating is described by the total dephasing time,  $T_2$  and not only by the population relaxation,  $T_1$  since the electric fields with the difference frequency  $\Delta\omega = \omega_{pu} - \omega_S$  act on the molecule. In the case of a Raman resonance

of this difference frequency to a vibrational transition in the molecular system, the optically coherent fields will drive the respective vibrational mode coherently and this coherence will decay when the laser fields are turned off and the system develops in phase during the delay time,  $\Delta t$ .<sup>60</sup> When the second *pump* laser interacts with this grating of Raman modes, it is scattered inelastically off the grating under Bragg conditions, leading to the coherent, anti-Stokes transition that generates the signal in the phase-matched direction.

## 2.2.2 Time-Resolved Coherent Stokes Raman Scattering

Figure 2.8 shows the potential energy diagrams and relevant double-sided Feynman diagrams for time-resolved coherent Stokes Raman Scattering (CSRS). At first, this FWM technique appears very similar to CARS but the process shows a much higher complexity than CARS in its interpretation. Since CSRS only plays a minor role in the experiments presented in this work, the full complexity of the process will not be described here. A complete discussion of the CSRS process in comparison to process such as CARS and DFWM can be found in other works.<sup>28–30,45,46,56,57,61</sup>

Briefly, in analogy to the CARS process, two *pump* lasers possess the same color ( $\mathbf{k}_1, \mathbf{k}_3$ ) while the *anti-Stokes* laser ( $\mathbf{k}_2$ ) is blue shifted relative to the wavelength of the *pump* lasers. The difference frequency between the *anti-Stokes* laser and the two *pump* lasers,  $\Delta\omega = \omega_{aS} - \omega_{pu}$  corresponds to a Raman transition in the electronic ground or excited state. Time-resolution is achieved by allowing the *pump/anti-Stokes* pulse pair ( $\mathbf{k}_1, \mathbf{k}_2$ ), to interact simultaneously with the sample while the second *pump* pulse,  $\mathbf{k}_3(\Delta t)$ , is delayed relative to the pulse pair by  $\Delta t$ . For this configuration, the Feynman diagrams **B** and **C** in Fig. 2.8 show the relevant contributions to the CSRS signal. Here all optical transitions are in resonance to the quantum state of the system, while diagram **A** utilizes virtual states and will therefore not contribute significantly to the CSRS signal.<sup>28–32,56,57</sup>

Diagrams **B** and **C** show the formation and propagation of an excited electronic state,  $|e^{(1)}(\Delta t)\rangle$  and an electronic ground state,  $|g^{(2)}(\Delta t)\rangle$ , respectively. These states develop in the delay time,  $\Delta t$  similar to DFWM described in section 2.1.1. Both ground and electronic excited state dynamics will be observed in the transient signal as a function of  $\Delta t$  and must both be considered in the expression for the third-order polarization of the CSRS process. Here, diagram **B** is described by the first term

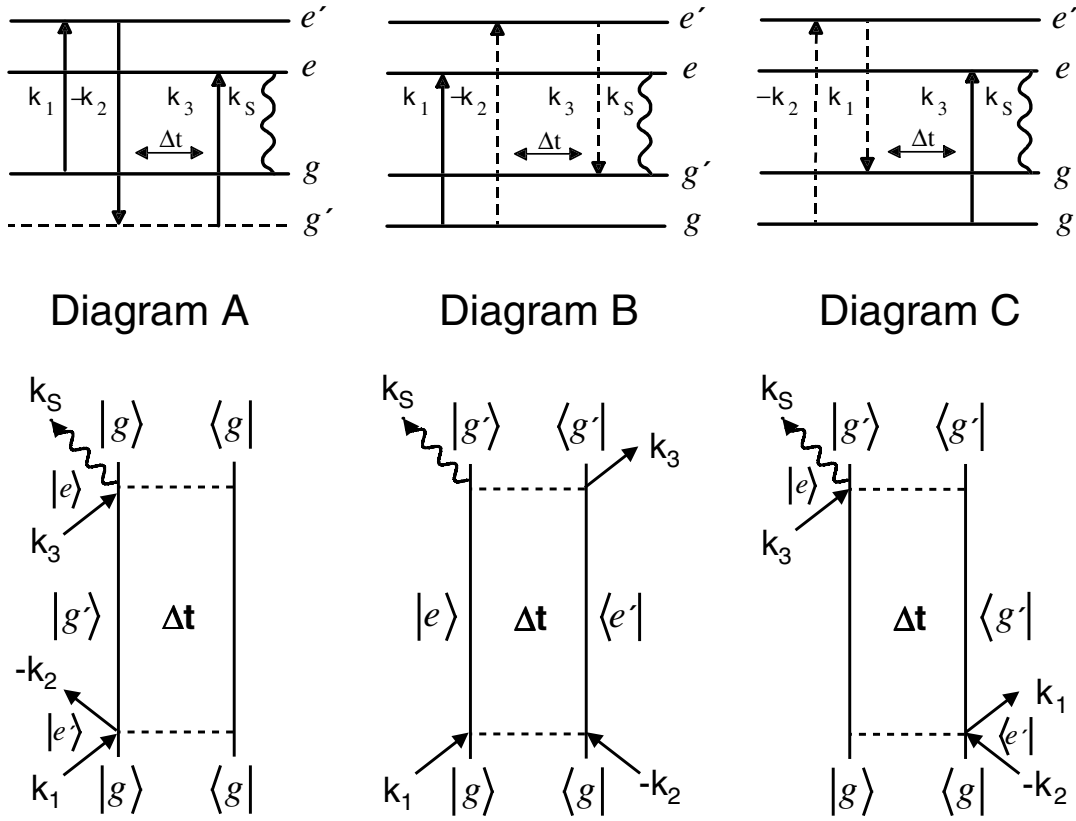


Figure 2.8: Diagrams **A-C** show three possible optical processes in the color scheme of a CSRS experiment in a potential energy diagram (top), and double-sided Feynman diagram (bottom) representation. Diagrams **B** and **C** show processes that are in full resonance with molecular states (solid horizontal lines), while diagrams **A** utilize virtual states (dashed horizontal lines)

in equation 2.35, where the dynamics of the electronically excited state,  $|e^{(1)}\rangle$  are interrogated by projecting into  $|g^{(2)}\rangle$  with the time variable *pump* laser,  $(\mathbf{k}_3(\Delta t))$ . Diagram **C** contributes to the second term of equation 2.35, where the dynamics of the electronic ground state,  $|g^{(2)}\rangle$  are interrogated by projecting  $|g^{(0)}\rangle$  into  $|e^{(1)}\rangle$  with the time variable *pump* laser,  $(\mathbf{k}_3(\Delta t))$ . For both cases, the third-order polarization is given by the *Stokes* transition, which is spectrally red shifted to the wavelength of the *pump* lasers and described by the transition dipole moment for the Stokes transition,  $\mu_S$ . With similar considerations that were made for the formulation of the CARS signal, the third-order polarization of CSRS process can be developed as follows:

$$P^{(3)}(\Delta t) = \langle e^{(1)}(\Delta t) | \mu_S | g'^{(2)}(\Delta t) \rangle + \langle g'^{(2)}(\Delta t) | \mu_S | e^{(1)}(\Delta t) \rangle + cc. \quad (2.34)$$

$$P^{(3)}(\Delta t) = \langle e^{(1)}(\Delta t) | \mu_S | (\mu E_{pu}(\Delta t) | e'^{(1)}(\Delta t) \rangle) \rangle + \langle g'^{(2)}(\Delta t) | \mu_S | (\mu E_{pu}(\Delta t) | g^{(0)}(\Delta t) \rangle) \rangle + cc. \quad (2.35)$$

It should be mentioned that the the first and second term in equation 2.34 are not complex conjugate terms. The states  $|g'^{(2)}(\Delta t)\rangle$  and  $|e^{(1)}(\Delta t)\rangle$  in each term are prepared by different laser pulses and show a different time evolution.<sup>d</sup> If the relevant time-dependent coefficients,  $c_e^*(\Delta t)$  and  $c_{e'}(\Delta t)$  for the first term and  $c_{g'}^*(\Delta t)$  and  $c_g(\Delta t)$  for the second term in equation 2.35 are expanded out of the respective state, equation 2.36 can be derived in the same manner as equation 2.33 in the previous section describing the CARS process. With this, it can be shown that the intensity of CSRS as a function of the delay time,  $\Delta t$  monitors a superposition of the coherence developing in time in the vibrational modes of the electronically excited and electronic ground state:

$$I_{CSRS}(\Delta t) = |A_1 \cdot c_e^*(0)c_{e'}(0)|^2 e^{-2\Delta t/T_{2,e}} + |A_2 \cdot c_{g'}^*(0)c_g(0)|^2 e^{-2\Delta t/T_{2,g}}. \quad (2.36)$$

Here, the coherent Raman modes dephase according to the respective time constant,  $T_{2,i}$  where the lifetime of the electronically excited state also contributes to the total dephasing of the electronically excited state Raman mode.

### 2.2.3 Transient Gratings

Figure 2.9 shows the relevant double-sided Feynman diagram along with a potential energy diagram for the realization of a transient grating scheme (TG) in the form used for the experiments described in this work.<sup>21, 34, 46, 53, 54, 62</sup> Here, the first two lasers interacting with the sample ( $\mathbf{k}_1, \mathbf{k}_2$ ) possess the same color and are referred to as *pump* lasers, while the third laser ( $\mathbf{k}_3$ ) is variable in its color and is referred to as the *probe* laser. In the transient grating scheme, the first two *pump* pulses ( $\mathbf{k}_1, \mathbf{k}_2$ ) interact simultaneously with the sample, preparing a transient grating of electronic ground and excited state molecules, as described in section 2.1.1 for the DFWM process by equations 2.19 and 2.23. The *probe* pulse ( $\mathbf{k}_3(\Delta t)$ ) is delayed in

<sup>d</sup>In the first term of equation 2.34, describing diagram B in Fig.2.8, the second order-ground state can be written as  $|g'^{(2)}(\Delta t, \mathbf{k}_2, \mathbf{k}_3)\rangle$  and the first-order excited state is given by  $|e^{(1)}(\Delta t, \mathbf{k}_1)\rangle$ . In the second term of equation 2.34, describing diagram C in Fig.2.8, the second order-ground state can be written as  $|g'^{(2)}(\Delta t, \mathbf{k}_1, \mathbf{k}_2)\rangle$  and the first-order excited state is given by  $|e^{(1)}(\Delta t, \mathbf{k}_3)\rangle$ .

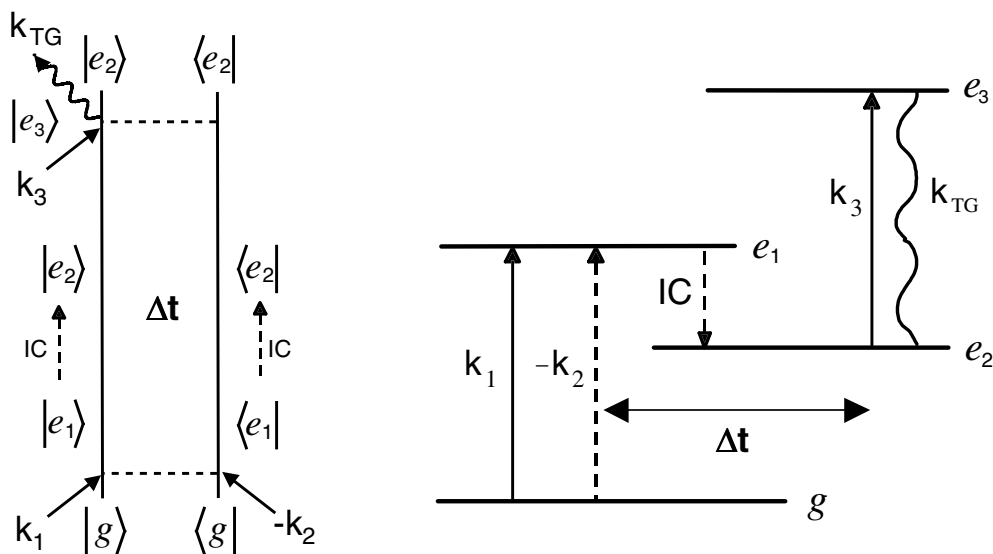


Figure 2.9: Potential energy diagram (right), and double-sided Feynman diagram (left) showing the relevant optical process in the color scheme of a transient grating experiment that utilizes the optical resonance of an electronically excited state that is spectrally shifted outside the resonance of the electronic ground state.

time by  $\Delta t$  relative to the *pump* lasers, in order to interrogate the dynamics of the transient population. By choosing the color of the *probe* pulse to be in resonance with an electronic transition that can only be accessed by an excited state, it is possible to selectively observe the development in this excited state population while the dynamics of the electronic ground state do not contribute to the transient signal. The precise experimental realization of this strategy is presented in section 5.4.1. Briefly, the excited state prepared by the *pump* lasers relaxes via internal conversion into an energetically lower lying electronic dark state  $|e_2\rangle$ , that possess an optical transition to a further electronic state  $|e_3\rangle$ . This optical transition is red shifted to the ground state absorption. By tuning the *probe* pulse to a resonance that selectively interrogates this secondary excited state population, the double-sided Feynman diagrams that describe the interrogation of the electronic ground state as shown in Fig. 2.3 and 2.5 for the DFWM process can be neglected and the transient grating process can be described by the diagram in Fig. 2.9 and the respective complex conjugate form.



The influence of the development in the secondary transient excited state population,  $|e_2\rangle$  on the TG signal as a function of the delay time of the *probe* laser pulse,  $\mathbf{k}_3(\Delta t)$  can be developed by following the Feynman diagram in Fig. 2.9. The two *pump* lasers prepare an electronically excited state,  $|e_1\rangle$  that relaxes into a secondary electronically excited state,  $|e_2\rangle$ . This state develops in time until the interaction with *probe* pulse induces the third-order polarization at  $\Delta t$  and projects  $|e_2\rangle$  into a further electronic state,  $|e_3\rangle$ . This polarization is given by the dipole transition described by  $\mu$ , between the respective states:

$$P^{(3)}(\Delta t) = \langle e_2^{(1)}(\Delta t) | \mu | e_3^{(2)} \rangle + cc. \quad (2.37)$$

Here,  $|e_3^{(2)}\rangle$  results out of the interaction of  $|e_2^{(1)}(\Delta t)\rangle$  and the electric field of the *probe* pulse,  $E_{probe}$  at  $\Delta t$ :

$$P^{(3)}(\Delta t) = \langle e_2^{(1)}(\Delta t) | \mu | \left( \mu E_{probe}(\Delta t) | e_2^{(1)}(\Delta t) \rangle \right) \rangle + cc. \quad (2.38)$$

$$P^{(3)}(\Delta t) = \langle e_2^{(1)}(\Delta t) | \mu | e_3 \rangle \langle e_3 | \mu E_{probe}(\Delta t) | e_2^{(1)}(\Delta t) \rangle + cc. \quad (2.39)$$

The identity operator,  $|e_3\rangle\langle e_3|$  is used to expand the expression in equation 2.38. It can then be shown that the TG signal as a function of the delay time,  $\Delta t$  is dampened quadratically with the decay of the excited electronic state  $|e_2\rangle$  by further expanding equation 2.39 with the time-dependent coefficients for this state, ( $c_{e_2}^*(\Delta t)$  and  $c_{e_2}(\Delta t)$ ) and separating them out of the integration over the stationary terms, in analogy to the procedure shown in the expansion of the CARS polarization in equation 2.28 of section 2.7. Here the phase development described by  $T_2^*$  must not be considered since the two *pump* lasers prepare the same state making the population development described by  $T_1$  the only relevant time constant:

$$c_{e_2}^*(\Delta t)c_{e_2}(\Delta t) = c_{e_2}^*(0)c_{e_2}(0)e^{-(t+\Delta t)/T_1}, \quad (2.40)$$

It is shown in section 5.4 that  $T_1$  is not a simple damping constant as shown for simplicity above, but rather complicated interplay of population flow into  $|e_2\rangle$  through an internal conversion, vibrational cooling within  $|e_2\rangle$  and depopulation of this state by means of a further internal conversion.

Using equation 2.39, the transient grating signal,  $I_{TG}$  can be expressed as:

$$\begin{aligned}
I_{TG}(\Delta t) &= \int_{t_3}^{\infty} |P^{(3)}(t, \Delta t)|^2 dt \\
&= \int_{t_3}^{\infty} \left| \left\langle c_{e_2}^*(\Delta t) \cdot e_2^{(1)} \mid \mu \mid e_3 \right\rangle \left\langle e_3 \mid \mu E_{probe}(\Delta t) \mid c_{e_2}(\Delta t) \cdot e_2^{(1)} \right\rangle \right|^2 dt \\
&= \int_{t_3}^{\infty} \left| \left\langle c_{e_2}^*(0) e^{-(t+\Delta t)/2T_1} \cdot e_2^{(1)} \mid \mu \mid e_3 \right\rangle \left\langle e_3 \mid \mu E_{probe}(\Delta t) \mid c_{e_2}(0) e^{-(t+\Delta t)/2T_1} \cdot e_2^{(1)} \right\rangle \right|^2 dt \\
&= \int_{t_3}^{\infty} \left| c_{e_2}^*(0) c_{e_2}(0) e^{-\Delta t/T_1} \cdot \left\langle e^{-t/2T_1} \cdot e_2^{(1)} \mid \mu \mid e_3 \right\rangle \left\langle e_3 \mid \mu E_{probe}(\Delta t) \mid e^{-t/2T_1} \cdot e_2^{(1)} \right\rangle \right|^2 dt \\
&= \left| c_{e_2}^*(0) c_{e_2}(0) e^{-\Delta t/T_1} \right|^2 \cdot \int_{t_3}^{\infty} \left| \left\langle e^{-t/2T_1} \cdot e_2^{(1)} \mid \mu \mid e_3 \right\rangle \left\langle e_3 \mid \mu E_{probe}(\Delta t) \mid e^{-t/2T_1} \cdot e_2^{(1)} \right\rangle \right|^2 dt.
\end{aligned} \tag{2.41}$$

When the integration over time,  $t$  is carried out from  $t_3$  to infinity and the resulting expression is represented with an amplitude factor,  $A$  the quadratic proportionality of the signal to the population of the excited electronic state being probed can clearly be seen:

$$I_{TG}(\Delta t) = |A \cdot c_{e_2}^*(0) c_{e_2}(0)|^2 e^{-2\Delta t/T_{1,e_2}}. \tag{2.42}$$

The development leading to equation 2.42 can be described qualitatively in order to give a clearer picture of the transient grating scheme. The population prepared by the simultaneously acting *pump* pulses and scattering of the *probe* pulse can be seen as the scattering of a single laser pulse from a non-equilibrium population analog to a incoherent *pump-probe* scheme. Here the only fundamental difference to the classical *pump-probe* scheme is rooted in preparation of an excited **population grating** by the two *pump* lasers rather than the simple **population**, excited by the single *pump* laser in a *pump-probe* scheme. This allows for an elastic **Bragg scattering** of the *probe* pulse off the excited state population grating with the detection of an optically coherent signal (where the homodyne detection of a quadrature detector leads to a quadratic proportionality of the population to the signal intensity) rather than the **incoherent signal** of a *pump-probe* scheme (where the signal is linearly proportional to the population).<sup>53,54</sup>

## 2.3 Theoretical Treatment of Elementary Molecular Dynamics

In the previous section, the interactions leading to the induction of a third-order polarization into a molecular sample, along with the molecular states prepared and propagated in the process, were described. In the following, the theoretical description of elementary nuclear dynamics and their coupling to electronic degrees of freedom will be described. First, the concept of wave packets will be introduced and the capability to monitor this coherent form of nuclear motion in the time-resolved FWM signal will be shown. Furthermore, the basic concepts underlining the coupling of nuclear motion in polyatomic molecules to electronic degrees of freedom are treated. With this, the mechanism of radiationless transitions such as internal conversion between different electronic states will be described. These types of transitions are facilitated precisely by the coupling of nuclear and electronic motion under the breakdown of the Born-Oppenheimer approximation.

### 2.3.1 Wave-Packet Formalism of Coherent Vibrational States

The treatment of the temporal evolution of the states induced by the successive interaction of a molecular system with the three laser pulses of a FWM process in section 2.1.1 was limited to a two level electronic system that neglected the full vibrational structure within the respective electronic states. Since the spectral bandwidth of the femtosecond laser pulses employed in the experiments described in this work can be characterized with a FWHM of approximately  $200\text{-}250\text{ cm}^{-1}$ , the coherent superposition of multiple vibrational states within an electronic state is possible. The phase-coupled excitation of vibrational states to a nuclear wave packet allows for the vibrational dynamics taking place within the excited molecular system to be observed via their influence on the transient FWM-signal.<sup>9,31,32,46,63</sup>

The mechanism with which vibrational wave packets manifest themselves in the transient FWM-signal of a CARS, CSRS, DFWM and TG process will be shown by discussing the influence of a vibrational wave packet prepared in the electronic ground state,  $|g\rangle$  at  $t = 0$  by pulses  $\mathbf{k}_1$  and  $\mathbf{k}_2$  as described in the CARS process

of section 2.2.1. For this, the state vector  $|g\rangle$  of the electronic ground state is separated with respect to the nuclear and electronic degrees of freedom according to the Born-Oppenheimer approximation that will be discussed in detail in section 2.3.2:

$$|g(r, R)\rangle = \sum_v^{\infty} c_{g,v} |\varphi_{g,v}(R)\rangle |\psi_g(r, R)\rangle. \quad (2.43)$$

If laser pulses  $\mathbf{k}_1$  and  $\mathbf{k}_2$  possess the spectral bandwidth capable of simultaneously exciting multiple vibrational states within the ground state potential at  $t = 0$ , the coefficients,  $c_v$  of these vibrational states become a function of time. Furthermore, the phase,  $\phi_v(t)$  given in the time-dependent phase factors of these vibrational states,  $\vartheta_v(t) = e^{-i(v+1/2)\omega t + \phi_v(t)}$  are coupled by the optically coherent laser pulses. Here the energy of the vibrational states are given by the vibrational quantum number,  $v$  and the eigenfrequency of the bond,  $\omega$  according to,  $E_v = (v + 1/2)\hbar\omega$ . This coherent superposition of vibrational states leads to a modulation of the nuclear bond distance,  $R$  of the respective bond. This can be shown when the expression for the expectation value of the bond distance  $\langle R \rangle$  is evaluated by separating the stationary and time-dependent terms:<sup>43,44</sup>

$$\begin{aligned} \langle R(t) \rangle &= \left\langle \varphi(R, t) \left| \hat{R} \right| \varphi(R, t) \right\rangle \\ &= \left\langle \sum_{j=0}^{\infty} c_j(t) e^{-i(j+1/2)\omega t} |\varphi_j(R)\rangle \left| \hat{R} \right| \sum_{k=0}^{\infty} c_k(t) e^{-i(k+1/2)\omega t} |\varphi_k(R)\rangle \right\rangle \\ &= \sum_{j=0}^{\infty} \sum_{k=0}^{\infty} c_j(0) c_k(0) e^{-t/T_1/2} R_{jk} e^{i(j-k)\omega t}. \end{aligned} \quad (2.44)$$

Here,  $R_{jk}$  represent the matrix elements,  $\langle \varphi_j(R) | \hat{R} | \varphi_k(R) \rangle$  and the time-dependent coefficients in equation 2.44 are summarized according to:

$$c_j^*(t) c_k(t) = c_j^*(0) c_k(0) e^{-t/T_2} \quad ; \quad c_j^*(t) c_j(t) = c_j^*(0) c_j(0) e^{-t/T_1}. \quad (2.45)$$

Assuming a harmonic potential, symmetry considerations show that only for  $|j \pm k| = 1$  are the matrix elements  $R_{jk} \neq 0$ . Due to this, equation 2.44, that describes the expectation value of  $R$ , will oscillate with the eigenfrequency,  $\omega$  of the respective nuclear bond.

In the case described above, where  $\mathbf{k}_1$  and  $\mathbf{k}_2$  prepare a vibrational wave packet in the electronic ground state, the wave packet is interrogated after developing in time

during  $\Delta t$  by a further laser pulse  $\mathbf{k}_3$ . Here, the coherent vibrational states of the wave packet are projected into a vibrational state of the electronically excited state via the transition dipole. The electronic transition involved in this interrogation is sensitive to the nuclear coordinate,  $R$  due to the Franck-Condon factor of this transition. The modulation of the Franck-Condon factor due to  $R$  oscillating with  $\omega$  as time evolves, leads to a modulation in the strength of the dipole transition and therefore to oscillations in the FWM signal that correspond to the vibrational frequency of the respective nuclear bond.

### 2.3.2 Internal Conversion in Polyatomic Molecules

Fundamental to the theoretical description of radiationless, non-adiabatic transitions between two electronic states of a molecular system is the coupling between the nuclear and electronic degrees of freedom. It is the phenomenon of vibronic coupling that facilitates radiationless electronic transition and this will be described below as it presents itself in the time-independent Schrödinger equation of the total molecular system. The Born-Oppenheimer approximation and the adiabatic picture of electronic states will be discussed as a possibility of solving the total molecular problem in the time-independent Schrödinger equation and the limitations of this picture is presented in the view of non-radiative electronic transitions such as internal conversion. Following this, two established theoretical descriptions of internal conversion in the literature, given by the Engelman-Jortner model and the picture of conical intersections in the 2-state/2-mode model will be presented.<sup>1, 7, 9, 64, 65</sup>

Under a separation of the time-dependent and time-independent variables, the time-independent Schrödinger equation can be written as:

$$\begin{aligned} H_t |\Psi_t(r, Q)\rangle &= E_t |\Psi_t(r, Q)\rangle \\ [H - E_t] |\Psi_t(r, Q)\rangle &= 0 \end{aligned} \quad (2.46)$$

where the total Hamiltonian,  $H_t$  is given by:

$$H_t = T_e(r) + T_N(Q) + U(r, Q). \quad (2.47)$$

The total Hamiltonian is represented by the operators of the kinetic energy of electronic and nuclear motion,  $T_e(r)$  and  $T_N(Q)$ , the total coulombic interaction including the operators of nuclear/nuclear, electronic/electronic and nuclear/electronic coulombic interaction in,  $U(r, Q)$ . In this description the normal coordinate,  $Q$  with  $Q = Q_1, Q_2, Q_3 \dots Q_j$  is used instead of the coordinates of the nuclei,  $R$  and all electronic coordinates are represented by  $r$  with  $r = r_1, r_2, r_3, \dots r_k$ .

The time-independent Schrödinger equation, as shown in equation 2.46, cannot be solved since the Hamiltonian does not allow for a separation of the variables. A strategy for approaching this dilemma begins with first solving the electronic problem. For the solution, all the operators containing electronic coordinates are summarized in the electronic Hamiltonian,  $H_{elec}$ :

$$[H_{elec}] |\psi_n(r, Q)\rangle = V_n(Q) |\psi_n(r, Q)\rangle \quad (2.48)$$

$$[T_e(r) + U(r, Q) - V_n(Q)] |\psi_n(r, Q)\rangle = 0. \quad (2.49)$$

The electronic problem can be solved parametrically with respect to  $Q$  for the electronic states,  $|\psi_n(r, Q)\rangle$ . This yields the *adiabatic* electronic potential energy surfaces,  $V_n(Q)$  as a function of the nuclear displacement. In this adiabatic picture, the electrons respond instantaneously (adiabatically) to the changing nuclear configuration. With these electronic potentials, the time-independent Schrödinger equation for the total molecular problem can be approached. For this, the total state vector of the system is expanded in terms of the electronic states obtained from the electronic problem, which are weighted with a nuclear coefficient,  $|\varphi_n(Q)\rangle$ :

$$|\Psi(r, Q)\rangle = \sum_n |\varphi_n(Q)\rangle |\psi_n(r, Q)\rangle. \quad (2.50)$$

This expansion can be substituted into the Schrödinger equation for the total molecular problem,

$$\sum_n [T_e(r) + U(r, Q) + T_N(Q) - E_t] |\psi_n(r, Q)\rangle |\varphi_n(Q)\rangle = 0. \quad (2.51)$$

Equation 2.51 is multiplied with the full set of the electronic state vectors  $\langle \psi_m(r, Q) |$  for the integration over the electronic coordinates. The eigenvalues of the electronic Hamiltonian as a function of the nuclear displacement are known in the form of the adiabatic potential states,  $V_n(Q)$  which allows for the substitution in equation 2.51,

giving a set of coupled differential equations according to:

$$[T_N(Q) + V_n(Q) - E_t] |\varphi_n(Q)\rangle + \sum_m^{\infty} \langle \psi_m(r, Q) | T_N(Q) | \psi_n(r, Q) \rangle |\varphi_n(Q)\rangle = 0. \quad (2.52)$$

In the expression above,  $\langle \psi_m(r, Q) | T_N(Q) | \psi_n(r, Q) \rangle$  can explicitly written as:

$$\begin{aligned} \Lambda_{mn} &= \langle \psi_m(r, Q) | T_N(Q) | \psi_n(r, Q) \rangle \\ &= -\hbar^2 \sum_i \frac{1}{2M_i} \left[ \langle \psi_m(r, Q) | \frac{\partial^2}{\partial Q_i^2} | \psi_n(r, Q) \rangle + 2 \langle \psi_m(r, Q) | \frac{\partial}{\partial Q_i} | \psi_n(r, Q) \rangle \frac{\partial}{\partial Q_i} + \frac{\partial^2}{\partial Q_i^2} \right]. \end{aligned} \quad (2.53)$$

$\Lambda_{nm}$  is referred to as the *non-adiabatic coupling matrix* and it is precisely this matrix, that describes the coupling of nuclear and electronic degrees of freedom. Here, the diagonal elements,  $\Lambda_{nn}$  represent the influence of nuclear motion on the form of the adiabatic electronic potentials, while the off-diagonal elements,  $\Lambda_{mn}$  ( $m \neq n$ ) show the mixing of electronic states that are coupled via the motion of the nuclei.<sup>65</sup> In the case that the kinetic energy of the nuclei is small, the nuclei only show a small displacement out of their equilibrium position,  $Q_0$  leading to a small perturbation and coupling of the electronic states. This consideration forms the basis for the Born-Oppenheimer approximation, that can be explicitly formulated as:<sup>1,46,64</sup>

$$\langle \psi_m(r, Q) | \frac{\partial^l}{\partial Q_i^l} | \psi_n(r, Q) \rangle \approx 0. \quad (l = 1, 2) \quad (2.54)$$

With this approximation,  $\Lambda_{mn} = 0$  and the Schrödinger equation 2.52 can be solved giving the vibrational coefficients,  $|\varphi_n(Q)\rangle$ , which represent the nuclear state vectors and the respective eigenvalues of these vibrational states. In this strict *adiabatic* picture, the electronic states are *pure* states that exist independently of one another since the coupling mechanism via nuclear motion is turned off by the assumption made in the Born-Oppenheimer approximation. This approximation gives a good picture of the molecular states in the case that the electronic states are energetically well separated in relation to the vibrational energy,  $\hbar\omega_{vib}$  so that:<sup>7</sup>

$$\frac{\hbar\omega_{vib}}{V_m(Q_0) - V_n(Q_0)} \ll 1. \quad (2.55)$$

Necessary for the description of non-radiative electronic transitions such as internal conversion, which represents a radiationless transition between two electronic

states of the same parity, are cases for which the adiabatic picture in the framework of the Born-Oppenheimer approximation cannot strictly be applied. This is essential for the description of non-radiative electronic transitions since it is the off-diagonal elements,  $\Lambda_{mn}$  ( $m \neq n$ ) representing the mixing of electronic states, that facilitate these type of transitions. In a strict adiabatic description, non-radiative transitions such as internal conversion are not possible since the electronic states are *pure*, with no mechanism of coupling. As stated in equation 2.55, the energy difference between the electronic states in relation to the vibrational energy of the nuclei is an important criterion for evaluating the relevance of the off-diagonal elements responsible for the coupling. In the following, two theories of internal conversion are presented that describe a weak vibronic coupling between energetically well separated electronic states and strong coupling in the intersection of two electronic states. The first case is treated by the Engelman-Jortner model where the transition takes place between energetically well separated electronic potentials.<sup>4,10</sup> Here, the molecular states that are derived out of the adiabatic picture are still representative and are therefore used in the evaluation of the radiationless electronic transition. The second case of strongly coupled electronic states is described by the conical intersection in the 2-mode/2-state model where the respective potential energy surfaces of the electronic states intersect one another, causing the adiabatic picture to fully break down.<sup>5,9,65</sup>

### A. Engelman Jortner Model of Radiationless Transitions

In the case of an internal conversion between the two electronic states  $|\psi_m\rangle$  and  $|\psi_n\rangle$ , that show a large energetic separation in relation to the vibrational states of the molecular system, the molecular states derived from the adiabatic picture together with weak vibronic coupling terms are used to describe this transition.<sup>4,10,64,66</sup> The basis for the rate constant of the internal conversion in this model is Fermi's Golden Rule, which describes the decay of an initial state into a bath of final states. When this principle is applied to the internal conversion between two electronic states, the rate of internal conversion is evaluated by (i) the strength of vibronic coupling between the participating electronic states through the *non-adiabatic coupling constant*,  $C$  and (ii) the Franck-Condon overlap,  $\langle\varphi_{mv}|\varphi_{nu}\rangle$  between the vibrational states within the initial and final electronic state. With this, the rate constant for an internal



conversion,  $k_{IC}$  in the statistical limit can be expressed as:

$$k_{IC} = \frac{2\pi}{\hbar} C^2 \sum_u \sum_v B_v |\langle \varphi_{mu} | \varphi_{nv} \rangle|^2 \delta(\Delta E + E_u - E_v) \quad (2.56)$$

$$C^2 = \sum_i \left| \hbar \omega_i \left\langle \psi_m \left| \frac{\partial}{\partial Q_i} \right| \psi_n \right\rangle \right|^2 \quad (2.57)$$

when the Kroneckers Delta is included in the expression to guarantee the conservation of energy. Here,  $\Delta E$  represents the energy difference between the electronic states in the equilibrium configuration of the nuclei,  $\Delta E = V_m(Q_0) - V_n(Q_0)$ , and  $E_v$  and  $E_u$  give the energy of the vibrational states within the respective electronic state.  $B(v)$  represents the distribution function of the respective vibrational states,  $|\varphi_{nv}\rangle$  in the initial electronic state,  $|\psi_n\rangle$ . The angular frequencies of the normal modes,  $\omega_i$  are obtained from the adiabatic picture.

In this description, specific normal modes can be given different roles in facilitating the electronic transition. Here, normal modes that show large contributions to the non-adiabatic coupling constant,  $C$  are labelled with the term *promoting modes*, since these modes provide the essential necessity for a rapid electronic transition by creating a strong interaction between the participating electronic states. Normal modes that show a large nuclear displacement in the equilibrium configuration,  $\Delta = Q_{0,m} - Q_{0,n}$  are referred to as *accepting modes*, since the advantageous Franck-Condon argument allow for the population of the initial electronic state to primarily flow into these normal modes in the final electronic state. In the case of a predominate accepting mode, it can be shown that equation 2.56 can be simplified to:

$$k_{IC} = \frac{2\pi}{\hbar} C^2 \frac{1}{\sqrt{2\pi(\Delta E)\hbar\omega}} \exp\left(-\frac{1}{2}\Delta^2\right) \exp\left(-\frac{\gamma(\Delta E)}{\hbar\omega}\right) \quad (2.58)$$

$$\gamma = \ln\left(\frac{2(\Delta E)}{\Delta^2\hbar\omega}\right) - 1. \quad (2.59)$$

From equation 2.58 it can be seen, in the case of a primary accepting mode, that the rate of an internal conversion will primarily be described by an exponential drop in the rate constant with a growing energy gap,  $\Delta E$  between the participating electronic states. It has been shown in experimental work, that this tendency adequately predicts the behavior of the rate constant for the internal conversion between the first excited and electronic ground state of polyene analogs of  $\beta$ -carotene with varying energy gaps between the participating electronic states.<sup>67</sup>

## B. Conical Intersections in the 2-State/2-Mode Model

For the region in which two potential energy surfaces intersect one another, the strict adiabatic description breaks down since the energy of the nuclear motion is on the same order as the energy gap between the respective electronic states. This causes a strong coupling between these two forms of motion, which take place on similar time scales due to the equivalent energy spacing. Modern theoretical models have derived the potential energy surfaces for this case and the shape of the two potentials in this region of intersection is strongly dependent on the normal coordinates,  $Q$  for which the surface is plotted.<sup>5,8,9,65,68-71</sup> The potential energy of the electronic states, plotted as a function of the normal coordinate of two specific forms of nuclear motion in the molecular system, takes on the shape of a *conical intersection* as shown in Fig. 2.10. Here, the two specific forms of nuclear motion are represented by a normal mode referred to as the *tuning mode* with the coordinate  $Q_t$  and a further normal mode label as the *coupling mode* with the coordinate  $Q_c$ . An analog description uses the gradient difference vector,  $\mathbf{X}_1$  and the non-adiabatic coupling vector,  $\mathbf{X}_2$  to describe the respective coordinates.<sup>8</sup> It is exclusively for these two coordinates that the degeneracy of the electronic potential energy surfaces (PES) is lifted for nuclear configurations leading away from the apex point of the intersection. Here, the normal coordinate  $Q_c$  ( $\mathbf{X}_2$ ) contains all nuclear motion involved in the coupling of the two electronic states. For all other normal coordinates of the molecular system, the two electronic states are degenerate and do not exhibit the characteristic form of a conical intersection.

The classification of the normal modes as tuning (gradient difference vector) or coupling modes (non-adiabatic coupling vector) is based on the function of these normal modes in forming the conical intersection between the two PES. Here, the symmetry of the normal modes in relation to the symmetry of the electronic states involved, plays a crucial role in defining the different type of normal modes. This can best be seen when the basis set for the total vector state is changed from the adiabatic basis described in equation 2.52 to a *diabatic* basis. The necessity in changing to a diabatic basis lies in the difficulty of evaluating the wave function of the adiabatic states and the molecular parameters derived from them, since they show strong fluctuations in their value in the vicinity of the intersection.<sup>65,72</sup> For this, a diabatic basis

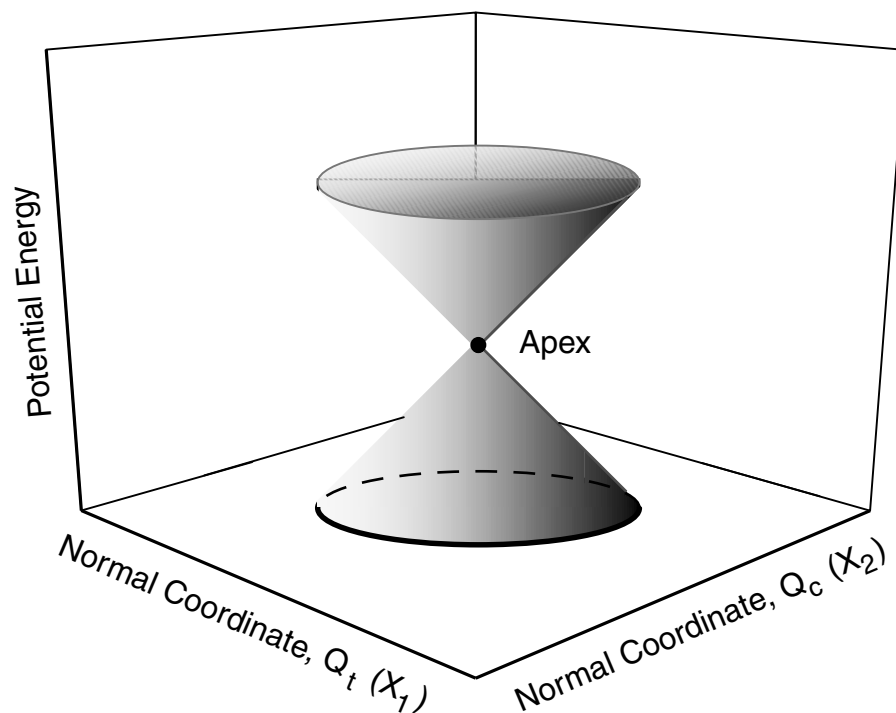


Figure 2.10: Schematic representation of the region in which two electronic states of a polyatomic molecular system intersect. The potential energy surface is plotted for nuclear coordinates of the normal modes referred to as the *tuning mode*,  $Q_t$  (or gradient difference vector  $\mathbf{X}_1$ ) and the *coupling mode* (or non-adiabatic coupling vector  $\mathbf{X}_2$ ). A precise description of these specific modes is given in the text.

is chosen so that the wave function and the molecular parameters derived from this basis are steady in the change of their value as a function of  $Q$  near the intersection. The theoretical considerations and the procedure in forming the diabatic basis are extremely complex and the relation to the adiabatic basis via symmetry operations goes past the scope of this work. This subject matter is described in detail in the literature.<sup>65, 73, 74</sup>

Here, the importance of symmetry considerations in defining the tuning and coupling mode will be limited to a brief discussion of the diabatic approach.<sup>65</sup> Important for the symmetry consideration is the difference in the treatment of the potential energy in the adiabatic and diabatic picture. In the adiabatic picture, the potential energy of the electronic states is diagonal in its matrix representation shown by equations 2.50 to 2.52, since the basis is orthogonal. In contrast to this, the matrix of the

electronic potentials is not diagonal in the diabatic picture which allows off-diagonal elements to contribute to the shape of the potential energy of the electronic states as a function of the nuclear coordinate in the electronic problem. Assuming that the two converging electronic states,  $|\psi_m^g\rangle$  and  $|\psi_n^u\rangle$  possess gerade (g) and ungerade (u) symmetry, respectively, then it can be seen from symmetry considerations that normal modes with gerade symmetry ( $Q_g$ ) will only influence the *energy* of the electronic states in the diagonal elements of the potential energy matrix, while the normal modes with ungerade symmetry ( $Q_u$ ) will only contribute to the *coupling* of the electronic states in the off-diagonal elements of the potential energy matrix.

$$\left\langle \psi_n^u \left| \frac{\partial H_{elec}}{\partial Q_g} \right| \psi_n^u \right\rangle \neq 0, \quad \left\langle \psi_m^g \left| \frac{\partial H_{elec}}{\partial Q_g} \right| \psi_m^g \right\rangle \neq 0, \quad \left\langle \psi_m^g \left| \frac{\partial H_{elec}}{\partial Q_g} \right| \psi_n^u \right\rangle = 0 \quad (2.60)$$

and,

$$\left\langle \psi_n^u \left| \frac{\partial H_{elec}}{\partial Q_u} \right| \psi_n^u \right\rangle = 0, \quad \left\langle \psi_m^g \left| \frac{\partial H_{elec}}{\partial Q_u} \right| \psi_m^g \right\rangle = 0, \quad \left\langle \psi_m^g \left| \frac{\partial H_{elec}}{\partial Q_u} \right| \psi_n^u \right\rangle \neq 0. \quad (2.61)$$

From this picture, the gerade modes, that “tune” the energy of the electronic states are labelled as tuning modes ( $Q_g \equiv Q_t$ ). The ungerade modes, that couple the electronic states represent coupling modes ( $Q_u \equiv Q_c$ ). When the diabatic electronic matrix is diagonalized through symmetry operations, the diagonal adiabatic matrix shows the shape of the conical intersection for the coordinates of the tuning and coupling mode.

In summary, it is the influence of the nuclear motion along the normal coordinate of the tuning mode on the energy of the both PES (lowering the energy of the upper electronic state and the raising the energy of the lower lying PES) that allow both electronic states to converge in the apex of the double cone in Fig. 2.10. On the other hand, it is the strong mixing of both electronic states due to the nuclear motion of the coupling mode that causes both PES to converge in the apex along this coordinate. Both effects lead to the characteristic shape of the conical intersection, that merge the two electronic states. This can be reformulated in an analog picture with the

definitions of the gradient difference vector,  $\mathbf{X}_1$  and the non-adiabatic coupling vector,  $\mathbf{X}_2$  giving the slope of the PES along the respective coordinate:<sup>8,68</sup>

$$\mathbf{X}_1 = \frac{\partial(V_m - V_n)}{\partial Q_t} \quad (2.62)$$

$$\mathbf{X}_2 = \left\langle \psi_m \left| \frac{\partial H_{elec}}{\partial Q_c} \right| \psi_n \right\rangle. \quad (2.63)$$

The conical intersection as described above facilitates the non-radiative transition between the two participating electronic states. Here the apex of the intersection is compared in the literature to the saddle point of a barrier reaction in a thermally induced chemical reaction.<sup>68</sup> While the saddle point represents a critical configuration with respect to the nuclear coordinates of the system in the pathway from reactants to products, the apex of the conical intersection also presents a bottleneck nuclear configuration in the space of the tuning and coupling mode for the transition between the two electronic potentials. Here, the slope of the excited state potential is steep, which causes a large acceleration of the nuclear motion in this region. Due to this, the transition between two electronic potentials via a conical intersection is assumed to take place within the time of a vibrational period. A longer time scale for the rate of population transfer between the respective PES is ascribed to an energy barrier on the PES of the initial state that lies in the pathway along the nuclear coordinates to the point of the conical intersection. Since the conical intersection can be separated from the point on which the molecule is prepared (in the case of a photoinduced excitation the Franck-Condon region of the excited electronic potential), these energy barriers on the PES of the initial state slow down the rate of the transition between the initial and final electronic state.



# Chapter 3

## Experimental Setup

In this chapter, the experimental realization of time-resolved four-wave mixing spectroscopy will be discussed. The chapter begins with the description of the femtosecond laser systems employed for generating the laser pulses that are required for the experiments. Here, the procedure for attaining and characterizing femtosecond laser pulses with variable time sequences and tunable wavelengths in the visible spectrum is presented. Special emphasis will be made on the beam geometry that is necessary for realizing the phase-matching conditions of the different FWM techniques applied in this work. Furthermore, the detection scheme will also be given special notice. The advantages of a multichannel detection scheme of the dispersed broadband signals with a CCD detector will be presented.

### 3.1 Generation and Characterization of Femtosecond Laser Pulses

In the following, two lasers systems will be presented that were used for the generation of the femtosecond laser pulses employed for the experiments in this work. The description will be brief since the process of acquiring femtosecond laser pulses with adequate parameters for molecular spectroscopy is described in detail in the literature.<sup>22,60,75,76</sup> The two laser systems described below can be classified into a system offering high pulse energy with a low repetition rate of 1 kHz and a second laser system offering low pulse energy with a high repetition rate of 100 kHz. For the experiments carried out with gas phase samples presented in chapter 4, the low

molecular density calls for a high pulse energy in order to attain an adequate signal intensity. For the experiments performed on condensed-phase samples presented in chapter 5, the high repetition rate of the 100 kHz system was utilized since the high molecular density of these samples allows for the use of low energy pulses.

### 3.1.1 1 kHz Laser System

The laser system used for the gas-phase experiments operates at 1 kHz, giving laser pulses with a FWHM of 70-80 fs and several  $\mu\text{J}$  per pulse. These pulses are tunable in their central wavelength between 450-700 nm. The components responsible for generating these laser pulses are given by a femtosecond oscillator, a stretcher, a regenerative amplifier, a compressor and two optical parametric amplifiers as shown in Fig.3.1.

The *femtosecond oscillator* is a Kerr-lens mode-locked, Titanium:Sapphire oscillator (MIRA, Coherent) pumped with an 8 W argon ion laser (Innova 300, Coherent) operating in the multi-line mode. The oscillator shows a laser transition at 800 nm and generates femtosecond laser pulses at 76 MHz with a FWHM of approximately 60 fs and 10 nJ per pulse. Higher energy pulses are attained from these pulses with an amplifier system (MXR/CPA 1000, Clark) consisting of a Stretcher, Amplifier and Compressor unit. Here the pulses from the oscillator are lengthened in time to a FWHM of approximately 200 ps by means of dispersion introduced through multiple reflections off a holographic grating in the *stretcher* unit. These pulses are coupled into a *regenerative amplifier*, which is a Titanium:Sapphire oscillator pumped with a frequency doubled Nd:YAG laser (MXR/ORC 1000, Clark) at 1 kHz with approximately 10 mJ per pulse. The cavity of the amplifier is blocked by a Pockels cell in order to avoid independent lasing of the amplifier. Single pulses from the stretcher are coupled into the cavity by means of the Pockels cell that is triggered by the Nd:YAG laser at 1kHz. The Pockels cell opens the cavity of the amplifier to allow the pulses coming from the stretcher to propagate for several round trips in the amplifier. The pulses are coupled out of the amplifier after attaining maximal amplification due to multiple trips through the active medium of the amplifier. The amplified pulses are directed into the *compressor* that compensates the dispersion introduced to the pulses in the stretcher. This is achieved by multiple reflections off a holographic grating, which yields pulses possessing a FWHM of approximately 80 fs and an energy of



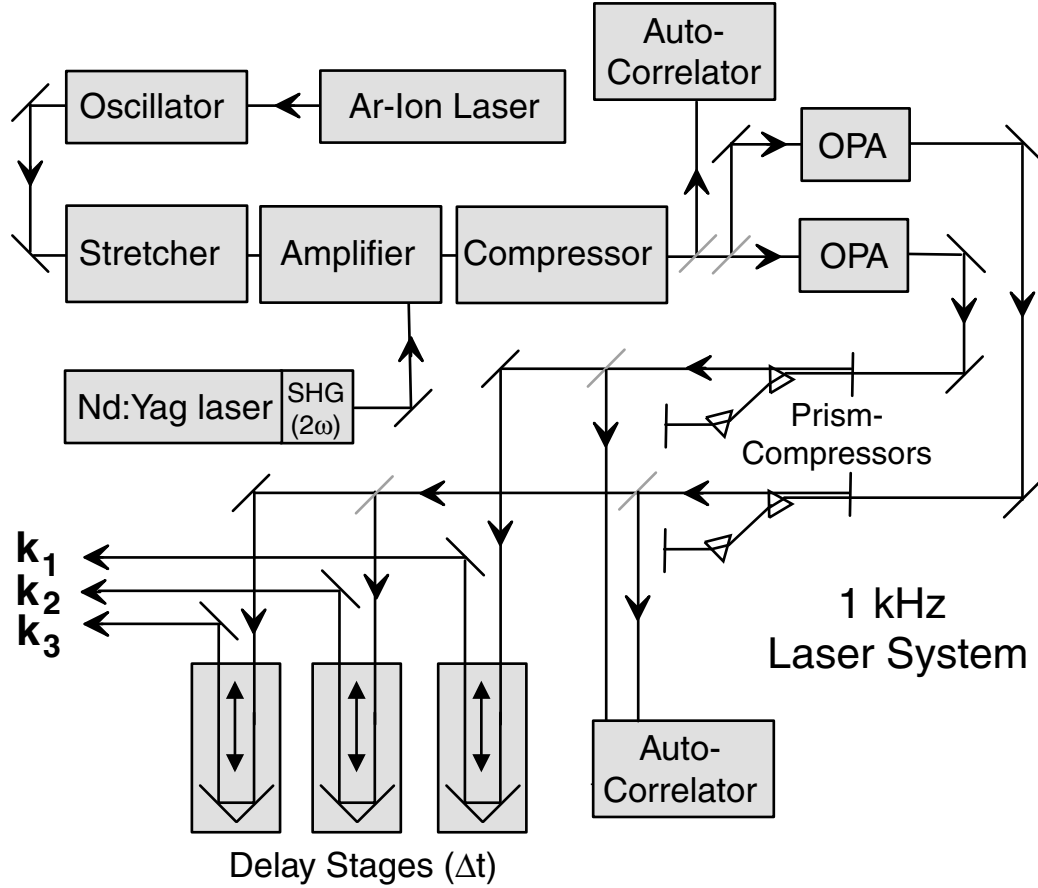


Figure 3.1: Laser system operating at a repetition rate of 1 kHz, generating laser pulses with a FWHM of 70-80 fs and several  $\mu\text{J}$  per pulse. The OPAs allow for a tunability of the central wavelength between 450 to 700 nm. For details see text.

about 1.0 mJ per pulse due to the amplification process. The laser pulses show a repetition rate of 1 kHz as a result of the timing of the Pockels cell in the amplifier and a central wavelength at 800 nm given by the unamplified oscillator.

With the help of a 50:50 beam splitter, these pulses are used to pump two *optical parametric amplifiers*, OPA (TOPAS, Light Conversion).<sup>75,77</sup> The OPAs utilize a difference-frequency generation performed with the pump pulses from the amplifier system,  $\omega_{\text{pump}}$  for attaining a signal,  $\omega_{\text{signal}}$  and idler,  $\omega_{\text{idler}}$  pulse with frequencies according to:

$$\omega_{\text{pump}} = \omega_{\text{signal}} + \omega_{\text{idler}}. \quad (3.1)$$

Multiple passes of the pump pulses allow for an amplification of this process. The

difference-frequency generation in combination with the frequency doubling of the signal, ( $2\omega_{signal}$ ) and sum frequency of the signal with the pump at 800 nm, ( $\omega_{signal} + \omega_{pump}$ ) allows for laser pulses to be attained with wavelengths that are tunable between 450 to 700 nm. The *signal* and *idler* also allow for a large region of the IR spectrum to be accessed, which was not utilized for the experiments in this work. The dispersion that accompanies the non-linear processes involved in generating the variable wavelengths in the OPAs is compensated with a double prism-arrangement (dispersive medium: BK7) in the standard configuration.<sup>60</sup> After compression, the OPAs yield laser pulses with a FWHM of approximately 70 fs with several  $\mu\text{J}$  of energy per pulse. The temporal profile of these pulses was characterized with an autocorrelator (MXR/AC 150, Clark), and the spectral profile of the pulses was recorded with the help of a monochromator (SpectraPro 500, Acton) and a CCD detector (SDS 9000, Photometrics), which is described in section 3.3. With the appropriate beam splitter, the laser pulses from the two OPAs are split into three independent beams after the prism compressors and the relative timing of the pulses is controlled by three delay stages (MT-85, MICOS) equipped with retroreflectors as shown in Fig. 3.1.

### 3.1.2 100 kHz Laser System

The laser system used for the condensed-phase experiments presented in chapter 5 generates laser pulses at a repetition rate of 100 kHz with a FWHM of 60-70 fs and 50-100 nJ per pulse. The wavelengths of the pulses are tunable between 450 and 700 nm. The system consists of a Kerr-lens, mode-locked Titanium:Sapphire oscillator, a Titanium:Sapphire amplifier unit with a compressor and two white-light optical parametric amplifiers as shown in Fig. 3.2. Here, a 25 W argon ion laser (Sabre, Coherent), operating in the multi-line mode, is used to pump the oscillator (MIRA, Coherent) with 8 W and the amplifier unit (RegA 9000, Coherent) with 17 W. The *oscillator* shows a laser transition at 800 nm and generates femtosecond laser pulses at 76 MHz repetition rate with a FWHM of approximately 60 fs and 10 nJ per pulse. With a 70:30 beam splitter, 30 % of the power from the oscillator is directed into the *amplifier*. An opto-acoustic modulator allows single laser pulses from the oscillator to be coupled into and out of the cavity of the amplifier with a repetition rate of 100 kHz. The Q-switch, which is also realized by an opto-acoustic modulator, opens the cavity exclusively for the time that the pulses propagate in the amplifier

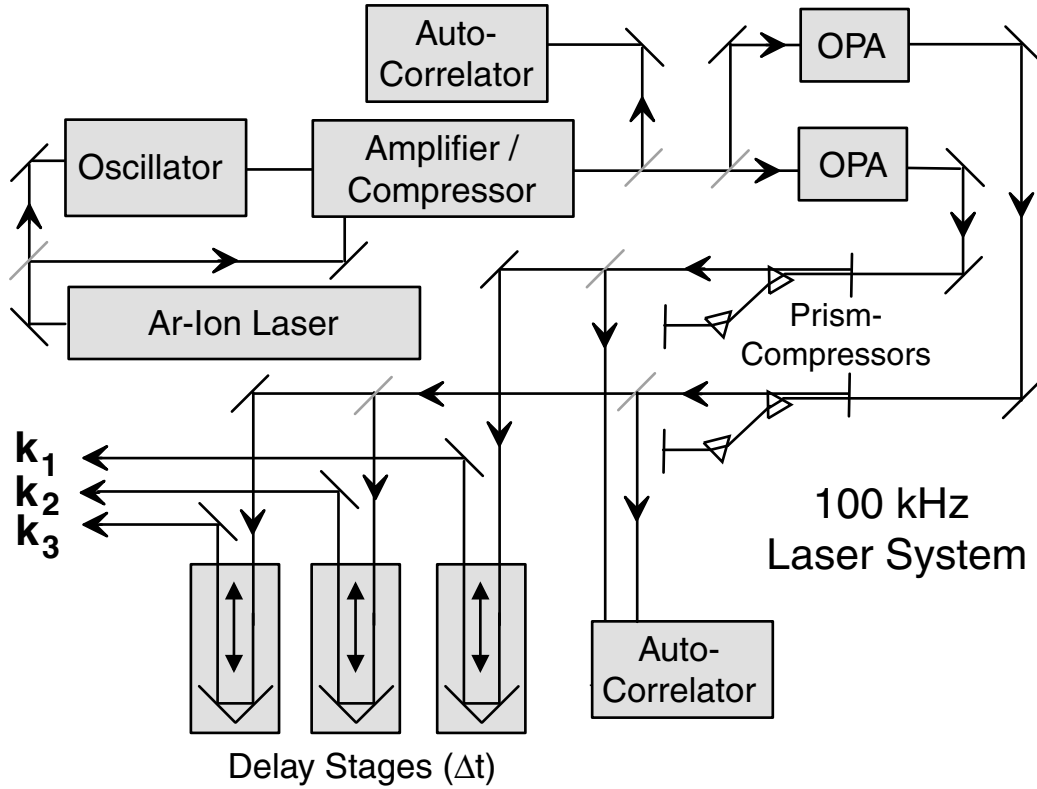


Figure 3.2: Laser system operating at a repetition rate 100 kHz, generating laser pulses with a FWHM 60-70 fs and 50-100 nJ per pulse. The OPAs allow for a tunability of the central wavelength between 450 to 700 nm. For details see text.

in order to avoid independent lasing of the amplifier. Dispersion is introduced into the laser pulses with each of the approximately 30 round trips in the cavity. This dispersion is adequate for stretching the pulses in their temporal profile and keeping the intensity of the laser pulses below the damage threshold of the optics as they are amplified by multiple passes through the active medium in the amplifier cavity. After coupling out of the amplifier, the temporal profile of the laser pulses is compressed, by compensating the dispersion introduced in the amplification process, with multiple reflections off a holographic grating.

The amplification process yields laser pulses with approximately  $8 \mu\text{J}$  per pulse at a repetition rate of 100 kHz and the compression yields a FWHM of 120 fs at a central wavelength of 800 nm, given by the wavelength of the unamplified oscillator. These pulses are used to pump 2 white-light *optical parametric amplifiers* (OPA

9400, Coherent). The OPAs produce laser pulses with variable wavelengths in the visible spectrum with 50 to 100 nJ per pulse. This is accomplished through a second harmonic generation and a white-light generation in the OPAs using the pulses from the amplifier. By utilizing a sum-frequency generation of the second harmonic pulses and variable IR components of the white-light pulses, tunable wavelengths between 450 and 700 nm can be generated. The dispersion introduced by these non-linear processes is compensated after the OPAs by two double prism-compressors (dispersive medium: BK7) in the standard configuration.<sup>60</sup> This yields laser pulses with a FWHM of approximately 60-80 fs. The pulses are characterized in their temporal profile with an autocorrelator (Femtoscope MC-2, BMI) and the spectral profile is acquired with a combination of a monochromator (SpectraPro 500, Acton) and a CCD detector (LN/CCD512SB, Princeton Instruments) described in section 3.3. With the appropriate beam splitter, the laser pulses from the two OPAs are split into three independent beams after the compression and the relative timing of the pulses is controlled by three delay stages (OWIS) equipped with retroreflectors as shown in Fig. 3.2.

## 3.2 Phase-Matching for Four-Wave Mixing Schemes

In chapter 2, the theoretical aspects of the four wave-mixing techniques (FWM) employed in this work were described. These four-wave mixing schemes were introduced with the most general form of FWM, represented by degenerate four-wave mixing (DFWM). The FWM techniques were then classified according to their color schemes into the coherent Raman techniques and virtual photon echos in the form of transient gratings. Here the same sequence will be followed for the discussion of the phase-matching conditions necessary for the experimental realization of these FWM techniques.<sup>21,53,54,78</sup> Special emphasis is put on the description of the phase-matching conditions, since the different types of FWM are not only characterized by different color schemes of the laser pulses presented in chapter 2. Also essential for realizing different FWM processes are the phase-matching conditions that selectively allow for an elastic or inelastic scattering off the different types of gratings induced into the sample space with the respective FWM technique. The varying phase-matching

conditions for the different FWM techniques are realized by using different phase-matching masks for the beam geometry, which will be presented in the following.

The beam geometry, phase-matching mask and wave vector diagram for the experimental setup used in a DFWM experiment are shown in panels A-C of Fig. 3.3. In the schematic representation of the beam geometry depicted in panel C, it can be seen that the three lasers, denoted by their respective wave vector,  $\mathbf{k}_1$ ,  $\mathbf{k}_2$  and  $\mathbf{k}_3$  are focused into the sample space in a non-colinear configuration by lens 1. The mask used to attain this type of beam geometry is shown in panel A of Fig. 3.3. In panel B, the phase-matching achieved with this non-colinear configuration is depicted with the wave vectors of the lasers and signal, involved in the DFWM process. Here, the phase matching conditions for a given FWM process call for the sum of the wave vectors to cancel. This allows for the direction of the signal, given by the respective wave vector,  $\mathbf{k}_{\text{DFWM}}$  to be derived:

$$\begin{aligned} 0 &= \mathbf{k}_1 + \mathbf{k}_3 - \mathbf{k}_2 - \mathbf{k}_{\text{DFWM}} \\ \mathbf{k}_{\text{DFWM}} &= \mathbf{k}_1 - \mathbf{k}_2 + \mathbf{k}_3. \end{aligned}$$

In panel A and C it can be seen that the beam geometry, given by the mask in panel A, allows for the maximum spatial separation of the DFWM signal,  $\mathbf{k}_{\text{DFWM}}$  from the lasers that generate the signal. This configuration is referred to in the literature as a folded-*BOXCARS* geometry.<sup>78-80</sup> In this configuration, the signal is spatially separated from the laser pulses in the vertical and horizontal axis in the plane perpendicular to the propagation of the laser pulses. After generating the signal in the sample space, the three laser pulses and the signal are brought into a parallel, non-colinear configuration with the help of a second lens. By using a second mask that only allows for the signal to pass, the DFWM signal can be separated off from the laser pulses and detected background free.

Similar configurations were applied for the realization of the two subcategories of FWM given by the coherent Raman techniques in the form of coherent anti-Stokes Raman scattering (CARS) and virtual photon echos in the form of transient gratings (TG). Panels A to F of Fig. 3.4 show the phase-matching mask, wave vector diagram and a picture of the lasers and signal projected onto a white screen after propagating through the sample space (given by a glass platelet for this demonstration) for a CARS and TG process. Here, the phase-matching strategy for the CARS and TG process

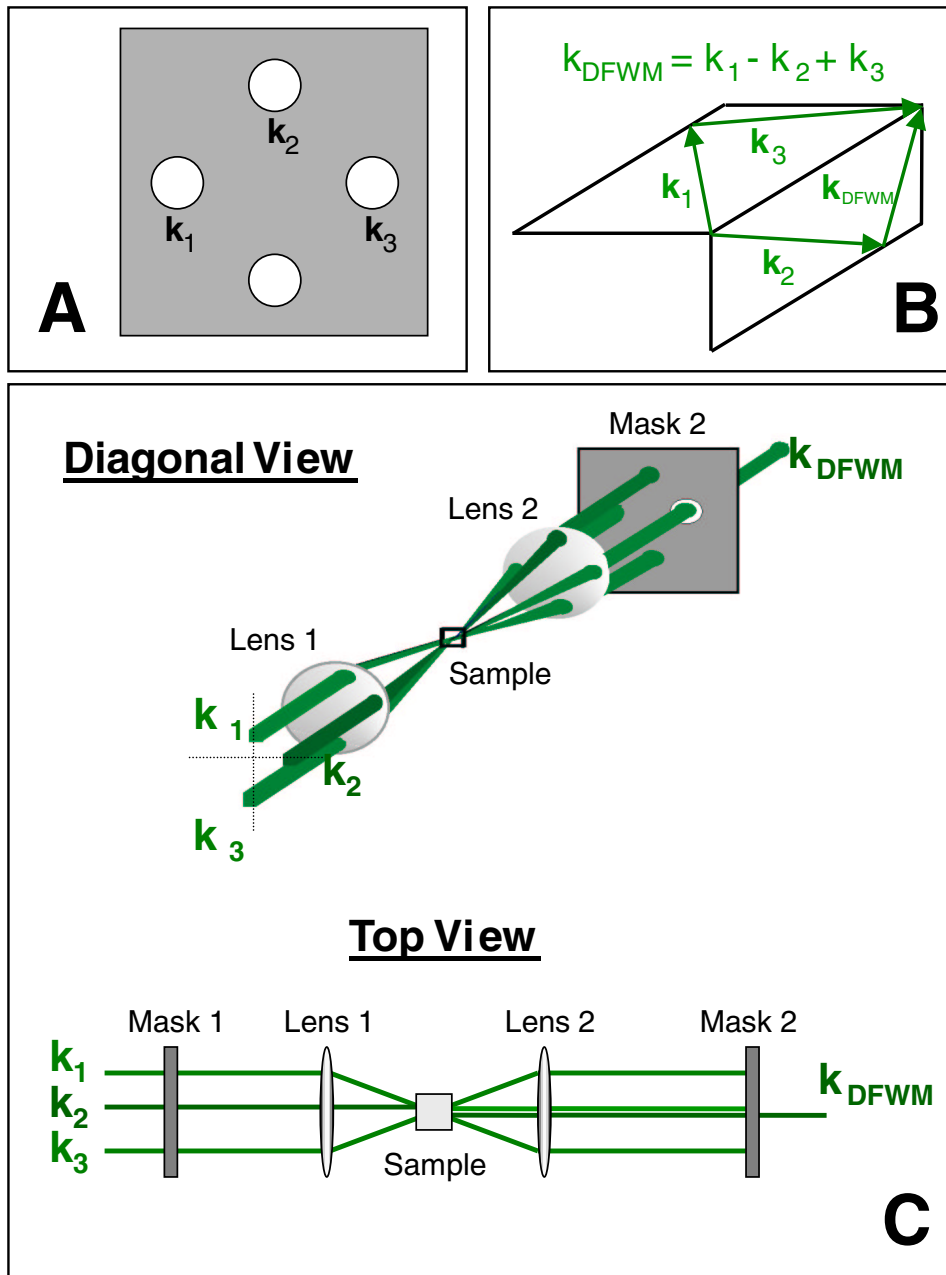


Figure 3.3: **A.** Phase-matching mask 1, used to bring the three laser pulses, involved in generating the DFWM signal, in a non-collinear configuration by letting the lasers pass through the respective holes of the mask in a parallel configuration. **B.** Wave vector diagram illustrating the phase-matching achieved in the DFWM process with the mask in diagram A. **C.** Diagonal and top view of the beam configuration used to achieve the phase-matching for a DFWM process.

is given by an inelastic and elastic scattering off the optical gating. For the CARS scheme, panel B and C of Fig. 3.4 show that the phase-matching mask brings the two *pump* lasers ( $\mathbf{k}_1$  and  $\mathbf{k}_3 \equiv \mathbf{k}_{\text{pu}}$ ) into the same plane, and the *Stokes* laser ( $\mathbf{k}_2 \equiv \mathbf{k}_S$ ) and the *anti-Stokes* signal ( $\mathbf{k}_{\text{aS}}$ ) into the same plane, which is perpendicular to the plane of the *pump* lasers. Since the *Stokes* laser is in the same plane as the *anti-Stokes* signal, the red-shifted wavelength of the *Stokes* laser relative to the color of the *pump* lasers only allows for an inelastic scattering of the second *pump* lasers in the form of the blue-shifted *anti-Stokes* signal to be phase-matched. The phase-matching condition for the *anti-Stokes* signal is realized in the form:

$$\mathbf{k}_{\text{aS}} = \mathbf{k}_{\text{pu}} - \mathbf{k}_S + \mathbf{k}_{\text{pu}}.$$

In the case of the transient grating configuration, panels E and F of Fig. 3.4 show that the phase-matching mask in panel D brings one of the *pump* laser ( $\mathbf{k}_1 \equiv \mathbf{k}_{\text{pu}}$ ) into the same plane as the *probe* lasers ( $\mathbf{k}_3 \equiv \mathbf{k}_{\text{probe}}$ ). The *probe* laser is variable in its color relative to the *pump* lasers and is shown here spectrally red-shifted. This forces the second *pump* laser ( $\mathbf{k}_2 \equiv \mathbf{k}_{\text{pu}}$ ) to be in the same plane as the signal and the transient grating signal ( $\mathbf{k}_{\text{TG}}$ ) is only phase matched for the elastic scattering of the *probe* laser:

$$\mathbf{k}_{\text{TG}} = \mathbf{k}_{\text{pu}} - \mathbf{k}_{\text{pu}} + \mathbf{k}_{\text{probe}}.$$

This can be seen by the identical color of the probe laser and signal shown in the picture of the lasers and signal in panel F of Fig. 3.4. This is in contrast to the CARS scheme in panel C of Fig. 3.4, where the signal is spectrally blue-shifted relative to the *pump* lasers.

In summary, the phase-matching conditions for the different FWM techniques can be realized with the help of different beam geometries, given by the respective phase-matching mask. This allows for the two subcategories of FWM to be realized by phase-matching the elastic or inelastic scattering of the respective laser off the induced grating.

### 3.3 CCD Broadband Detection

Due to the broadband nature of the femtosecond pulses employed in the experiments, different wavelengths within the spectral profile of the laser pulses can si-

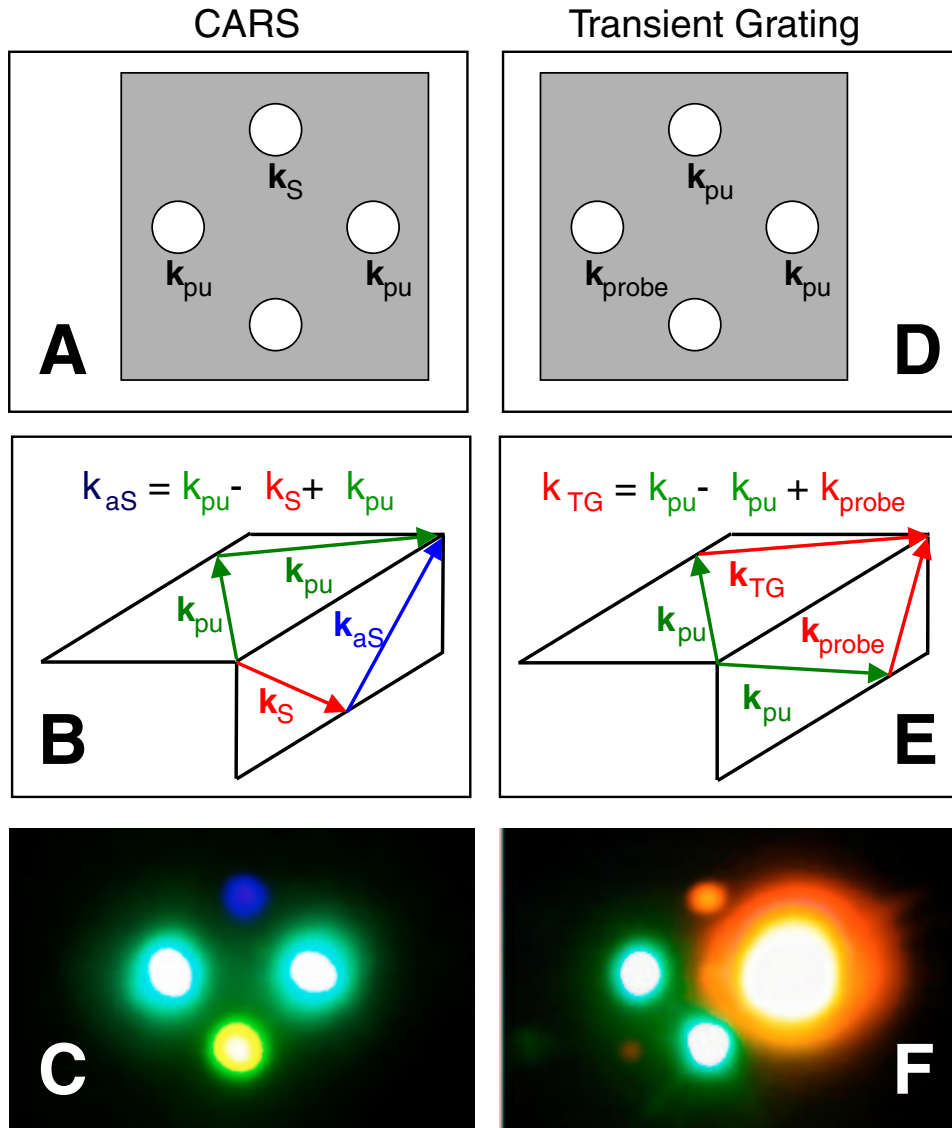


Figure 3.4: **A.** Phase-matching mask for realizing a CARS process. **B.** Wave vector diagram for the phase-matching of the lasers and signal involved in a CARS process. **C.** Photograph of the lasers and signal of a CARS process projected onto a white screen after passing the sample space. Here, the blue sifted anti-Stokes signal results from the phase matching of an inelastic scattering of a *pump* laser off the induced grating. **D.** The phase matching mask for realizing a TG process. **E.** Wave vector diagram for the phase-matching of the lasers and signal involved in a TG process. **F.** Photograph of the lasers and signal of a TG process projected onto a white screen after passing the sample space. The identical color of the signal and *probe* pulse results from the phase matching of an elastic scattering of the *probe* laser off the induced grating.



multaneously access a variety of quantum states within the molecular systems of interest. For the work presented in chapter 4, different FWM processes are generated in the sample since the spectral profile exceeds the vibrational quantum spacing in the molecular system. In chapter 5, different quantum states of the molecular system are simultaneously interrogated with the broadband pulses and these states show different dynamics. In both cases, the spectral components of the broadband signal reflect the varying dynamics generated and interrogated by the spectrally broad laser pulses.

In order to characterize the dynamics at different spectral positions of the broadband FWM signals, the combination of a monochromator and a multichannel CCD camera was employed for the detection. Here, the monochromator (SpectraPro 500, Acton) allows for a spatial separation of the FWM signal into its spectral components, which can be detected simultaneously with a multichannel CCD detector when the exit slit is removed. For this, the spatially dispersed signal from the monochromator is projected onto the silicon chip of the CCD camera, which is divided into  $256 \times 1024$  pixels (SDS 9000, Photometrics) or  $512 \times 512$  pixels (LN/CCD512SB, Princeton Instruments) with the dimensions of  $26 \times 26 \mu\text{m}$  for each pixel. The columns of pixels, that are parallel to the orientation of the former exit slit, are calibrated with respect to the spatial dispersion of the monochromator by determining the positions of the atomic lines of Hg/Cd, Ne, K and Rb spectral lamps on the chip.<sup>81</sup> It is possible to group an optional amount of calibrated pixels together to form spatially larger detection units. The signal detected in these larger units is the sum of the signal intensity recorded in the individual pixels. This technique is referred to as *binning* and allows for a higher signal to noise ratio due to a lower read out noise when the pixels are read out together. Here, two types of binning can be distinguished: (*i*) vertical binning, where columns are grouped together with the same orientation as the former exit slit of the monochromator and (*ii*) horizontal binning, where the pixels (or pixel columns) are put together at the cost of the spectral resolution. For the measurements discussed here, all vertical columns are binned together since the spectral information only varies in the horizontal axis. A horizontal binning was chosen that proved to be the best compromise between signal to noise ratio in the time domain transients and the spectral resolution necessary for the experiment.

At a fixed delay time,  $\Delta t$  of the time variable laser pulse in the respective FWM

technique, a mechanical shutter opens and allows the chip to be exposed for approximately 100 to 1000 ms. With a laser system running at a repetition rate of 1 kHz, this allows the CCD camera to accumulate about  $10^2$  to  $10^3$  signal pulses, while the CCD in combination with a 100 kHz laser system integrates over approximately  $10^4$  to  $10^5$  signal shots before closing the shutter. The accumulated signal on the silicon chip is read out for each spectrally calibrated column of pixels. Following the read out, the relative timing of the variable laser pulse that introduces the time resolution in the experiment, is moved to a new delay time value and this procedure is repeated for all desired delay times. With this, the full spectrum of the FWM signal is attained as a function of the variable delay time,  $\Delta t$  involved in the respective FWM technique.

## Chapter 4

# The State Selectivity of Femtosecond Time-Resolved Four-Wave Mixing

In the following, an experimental scheme that combines femtosecond time-resolved degenerate four-wave mixing (DFWM) performed on gaseous iodine with a broadband multichannel CCD detection is presented.<sup>82</sup> The femtosecond laser pulses, employed in generating the four-wave mixing signal, possess a spectral bandwidth that exceeds the energy spacing of the vibrational states accessed in molecular iodine. This opens the possibility of generating a variety of multi-color schemes such as CARS and CSRS parallel to the DFWM process, since the necessary wavelengths for these multi-color schemes are included in the bandwidth of the laser pulses. The different FWM processes will show themselves at different spectral positions of the broadband signal and a CCD multichannel detector allows for the dynamics generated by these processes to be characterized simultaneously by the broadband detection of the spectrally dispersed signal. The simultaneous generation and detection of a CARS, CSRS and DFWM process in a time-resolved scheme allows for a direct comparison of the molecular states that are prepared, propagated and interrogated by these processes under identical experimental conditions.

## 4.1 Methodology of Time-Resolved Degenerate Four-Wave Mixing

General aspects of the experimental realization of time-resolved DFWM have been described in chapter 3 and the theoretical treatment of this FWM process was given in chapter 2. Briefly, three laser pulses ( $\mathbf{k}_1$ ,  $\mathbf{k}_2$  and  $\mathbf{k}_3$ ) with identical parameters ( $\lambda = 573$  nm, FWHM = 80 fs, 2  $\mu$ J) are focused into a sample of gaseous iodine, enclosed in a vacuum sealed cuvette with a cell length of 1.0 cm. The sample is heated to 80°C resulting in a vapor pressure of approximately 20 hPa. As shown in panel A of Fig. 4.1, the central wavelength of  $\lambda = 573$  nm for all three laser pulses is resonant with an electronic transition between the electronic ground state (X-state) and the excited electronic B-state in gaseous iodine. With an excitation wavelength of 573 nm, transitions from excited vibrational states in the electronic ground state can be neglected.<sup>28</sup> The excitation wavelength of  $\lambda = 573$  nm and a spectral pulse width of approximately 10 nm (FWHM) allows for the coherent excitation of 3 neighboring vibrational eigenstates centered around the vibrational quantum number  $v' = 27$  in the excited B-state of gaseous iodine.<sup>83</sup> For the electronic ground state, the bandwidth is adequate for the coherent superposition of the vibrational eigenstates with  $v'' = 0$  and  $v'' = 1$ .<sup>84,85</sup>

As shown in panel B of Fig. 4.1, time-resolution is achieved by allowing two of the three pulses to interact with the sample simultaneously, as a pulse pair ( $\mathbf{k}_1$ ,  $\mathbf{k}_2$ ), while the third pulse ( $\mathbf{k}_3 \equiv \mathbf{k}_3(\Delta t)$ ) is varied in time relative to this pulse pair. One can distinguish two scenarios with respect to the relative timing of the three laser pulses. In the first case, which will be denoted as negative delay times ( $\Delta t < 0$ ), the time variable laser pulse,  $\mathbf{k}_3(\Delta t)$  interacts with the molecular system first and initiates the molecular dynamics, which are probed by the pulse pair  $\mathbf{k}_1$  and  $\mathbf{k}_2$ . For positive delay times ( $\Delta t > 0$ ), the pulse pair ( $\mathbf{k}_1$ ,  $\mathbf{k}_2$ ) interacts with the sample first and prepares the dynamics that are probed by  $\mathbf{k}_3(\Delta t)$ . The signal, generated in the phase-matched direction,  $\mathbf{k}_{\text{DFWM}} = \mathbf{k}_1 - \mathbf{k}_2 + \mathbf{k}_3$  is coupled into a monochromator and the dispersed signal is detected with a multichannel CCD camera as described in section 3.3.

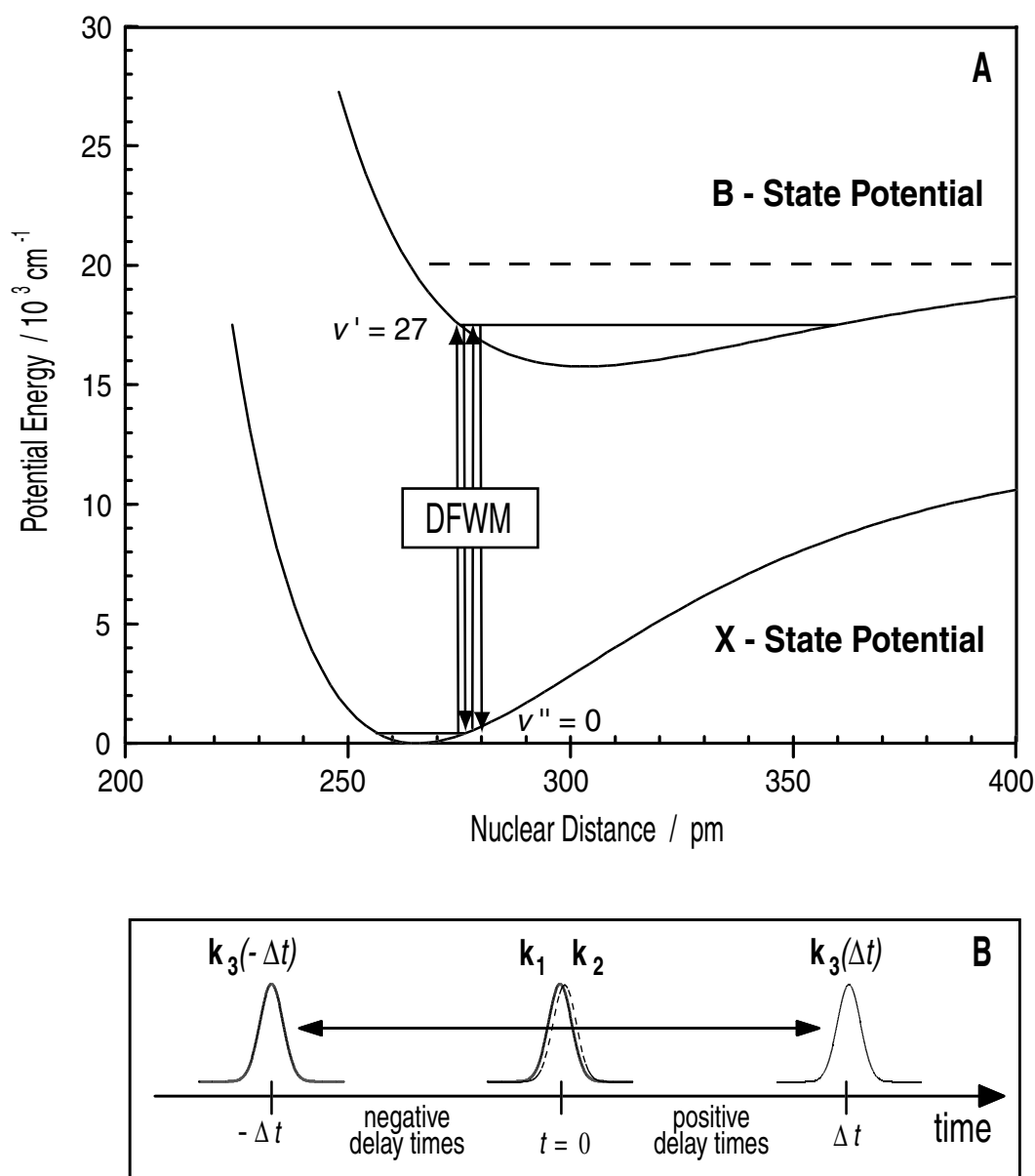


Figure 4.1: **A.** Potential energy diagram of gaseous iodine, showing the electronic transition between the electronic X and B-state utilized by the DFWM process at  $\lambda_1 = \lambda_2 = \lambda_3 = 573 \text{ nm}$ . **B.** Relative timing of the laser pulses denoted with the respective wave vector: For negative delay times ( $\Delta t < 0$ ), the time variable pulse ( $\mathbf{k}_3(\Delta t)$ ) prepares the dynamics that are interrogated by the pulse pair ( $\mathbf{k}_1, \mathbf{k}_2$ ). For positive delay times ( $\Delta t > 0$ ), the pulse pair interacts with the system first, initiating the dynamics probed by the time variable laser.

## 4.2 Experimental Results: CCD-Broadband Detection of Time-Resolved Four-Wave Mixing

The FWM signal intensity can be plotted as a function of the respective detection wavelength,  $\lambda_{det}$  and the delay time,  $\Delta t$  of the time variable laser pulse  $\mathbf{k}_3(\Delta t)$ . A contour plot of this type is shown in Fig. 4.2. The modulations of the intensity along the time axis can be seen across the full spectral width of the recorded FWM signal. In order to obtain a more detailed view of the time domain behavior of the signal, cross-sections of the contour plot along the time axis at a fixed detection wavelength are made. An analysis of the different dynamics observed within the FWM signals with the help of these cross-sections shows that there are three characteristic contributions within the spectral components of the signal pulse.

The spectral position of these three distinct contributions are marked in Fig. 4.2 and the dynamics are plotted in panels A-C in Fig. 4.3 for the central wavelength of the pulse ( $\lambda_{det} = 572.4$  nm), blue shifted from the central wavelength ( $\lambda_{det} = 566.6$  nm) and shifted to the red flank of the pulse ( $\lambda_{det} = 578.9$  nm). Generally, this change in the behavior of the signal with respect to the detection wavelength can be attributed to the polychromatic nature of the broadband fs laser pulses employed in the experiment. The different wavelengths incorporated in the spectral profile of the laser pulses allow for three different FWM processes, CARS, DFWM and CSRS, to be generated simultaneously in the sample. The identification of the three FWM processes at different wavelengths of the broadband signal can be made when the characteristic state-selectivity, that manifests itself in the preparation of vibrational wave packets on different electronic potentials of the molecular system, is compared to experiments in the literature, where these three FWM process are explicitly carried out on gaseous iodine.<sup>28-30</sup>

The detection at the central wavelength of the signal,  $\lambda_{det} = 572.4$  nm corresponds to a classical DFWM experiment, where the detection wavelength is equivalent to the central wavelength of the three laser pulses. The transient signal at this detection wavelength is shown in panel B of Fig. 4.3. For negative delay times ( $\Delta t < 0$ ), the development of a first-order polarization prepared by  $\mathbf{k}_3(\Delta t)$  can be observed, as described in section 2.1.2. This first-order polarization is modulated by a vibrational wave packet with a period of 355 fs, which corresponds to the vibrational period in the

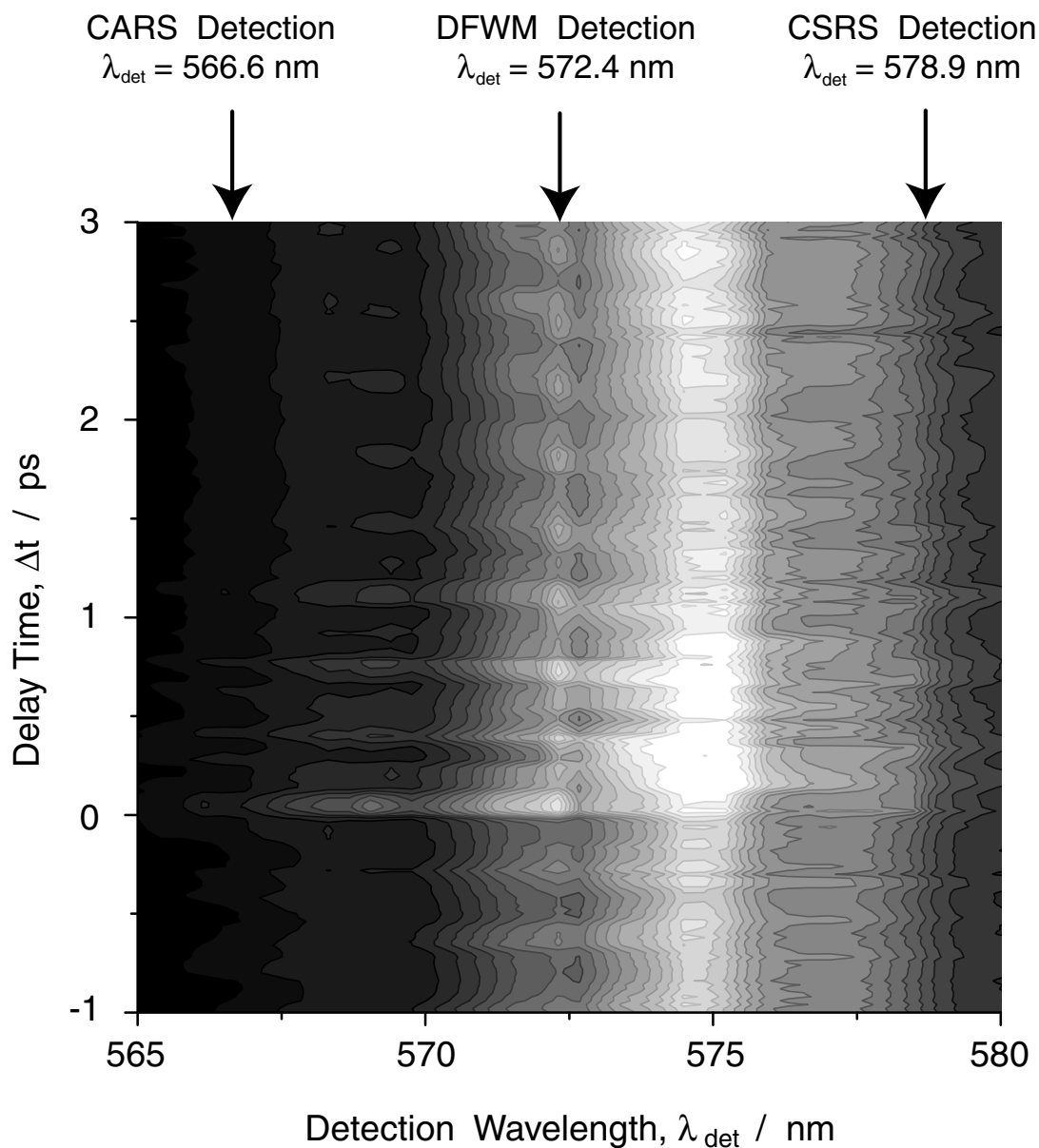


Figure 4.2: Contour plot of the DFWM intensity as a function of the delay time,  $\Delta t$  and the detection wavelength,  $\lambda_{det}$  acquired by CCD multichannel detection of the DFWM spectrum for varying delay times. Cuts made along the time axis show that the DFWM signal shows dynamics characteristic for DFWM as well as CARS and CSRS processes (See Fig. 4.3).

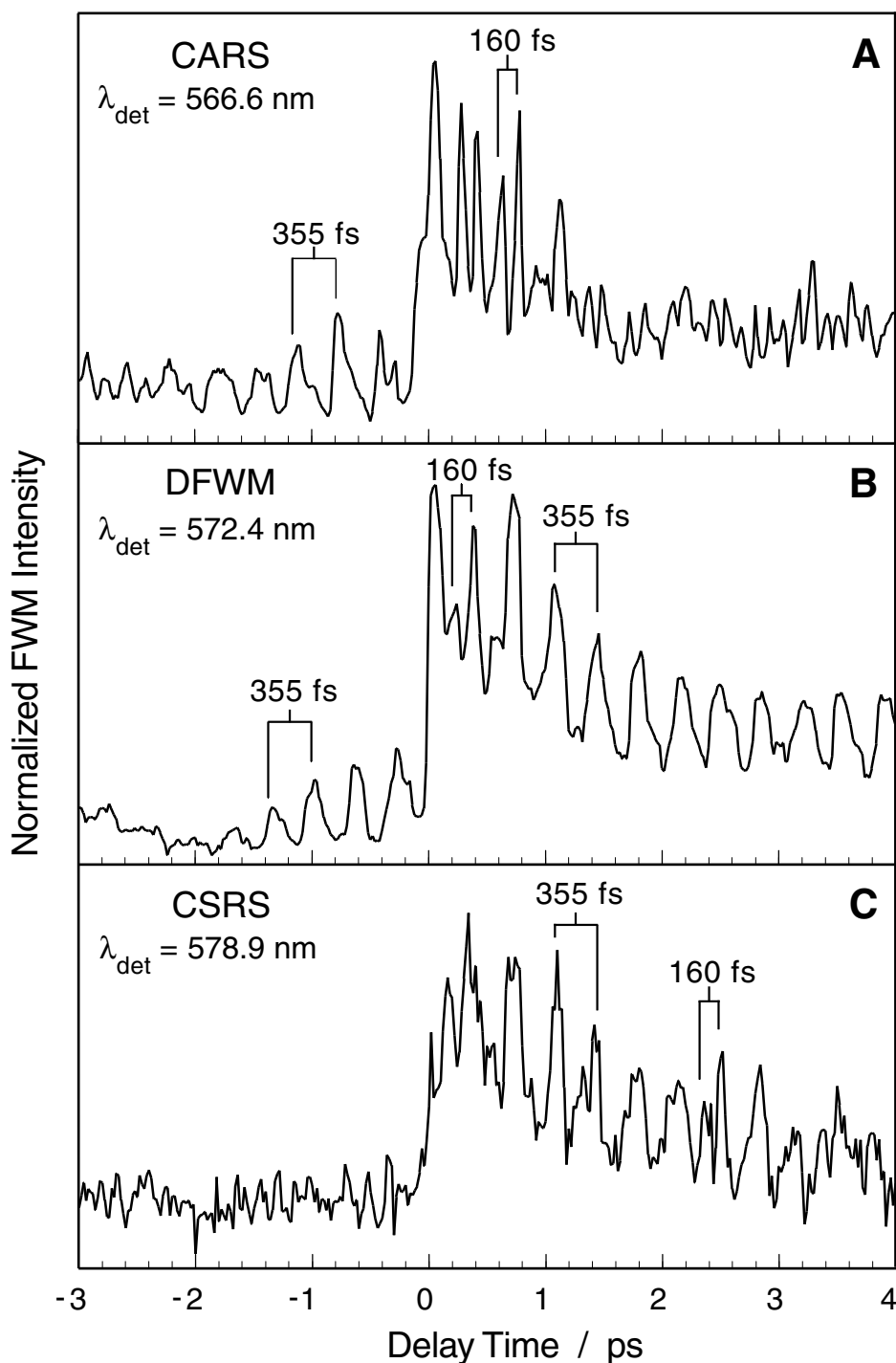


Figure 4.3: Diagrams **A-C** show three cross-sections made along the time axis of the contour plot in Fig. 4.2. **A.** At  $\lambda_{det} = 566.6 \text{ nm}$ , the dynamics reflect the state selectivity of a CARS process. **B.** At a detection wavelength of  $\lambda_{det} = 572.4 \text{ nm}$ , the observed dynamics are representative of a DFWM process. **C.** A shift to the red side of the FWM spectrum shows dynamics of a CSRS process at  $\lambda_{det} = 578.9 \text{ nm}$ .



excited B-state of iodine. This assignment is confirmed by the Fourier transformation of the transient for  $\Delta t < 0$  in panel C of Fig. 4.4. Here, the two peaks at 92 and 185  $\text{cm}^{-1}$ , give the energy spacing between two neighboring vibrational eigenstates ( $\Delta v' = 1$ ) and the first overtone ( $\Delta v' = 2$ ) accessed in the excited B state by a laser pulse with  $\lambda = 573 \text{ nm}$ .<sup>84,85</sup> The mechanism, with which vibrational wave packets manifest themselves in a FWM signal was described in section 2.3.1. For positive delay times ( $\Delta t > 0$ ), the transient shows the dynamics prepared by the pulse pair  $(\mathbf{k}_1, \mathbf{k}_2)$ . Here the superposition of oscillations can be seen that possess a period of approximately 160 fs, corresponding to the period of a vibrational wave packet in the electronic ground state of iodine, and oscillations of 355 fs showing dynamics that can be attributed to the excited B-state. Again, this assignment can be confirmed by the Fourier transformation in panel D of Fig. 4.4, which shows a peak at 211  $\text{cm}^{-1}$ , corresponding to the energy spacing of the vibrational eigenstates in the ground state around the vibrational quantum number  $v'' = 1$ .<sup>83</sup> The two peaks at 93 and 185  $\text{cm}^{-1}$  are representative of the excited B state as described above. These findings correspond to the state selectivity expected of the DFWM process described by theoretical and experimental work in the literature.<sup>28-30,45</sup> The two processes that take place in the interaction of the pulse pair,  $\mathbf{k}_1, \mathbf{k}_2$  with the sample, preparing a grating of molecules in the electronic ground and excited B-state, are shown in Figures 2.2 and 2.3 on page 15 and 16, respectively.

The transient behavior in the blue flank of the FWM signal at  $\lambda_{det} = 566.6 \text{ nm}$  is shown in panel A of Fig. 4.3. Here, different dynamics are observed in comparison to the transient at  $\lambda_{det} = 572.4 \text{ nm}$ . With a comparison to CARS experiments on gaseous iodine described in the literature, the dynamics observed at this detection wavelength can be attributed to the superposition of a CARS and DFWM process.<sup>28-30</sup> In the case of the CARS process, a wavelength near the maximum of the spectral profile of  $\mathbf{k}_1$  will act as a *pump* laser while the spectral region in the red flank of  $\mathbf{k}_2$  serves as a *Stokes* laser. The time variable laser,  $\mathbf{k}_3(\Delta t)$  acts as the second *pump* laser and the coherent anti-Stokes signal is generated in the blue flank of the signal. The oscillations at  $\Delta t < 0$  with a period of approximately 355 fs are the result of a first-order polarization modulated by the vibrational wave packet dynamics of the excited B-state. This is confirmed by the appropriate peaks in the Fourier transformation at 94 and 185  $\text{cm}^{-1}$  shown in panel A of Fig. 4.4. For  $\Delta t > 0$ , the transient and the Fourier transformation

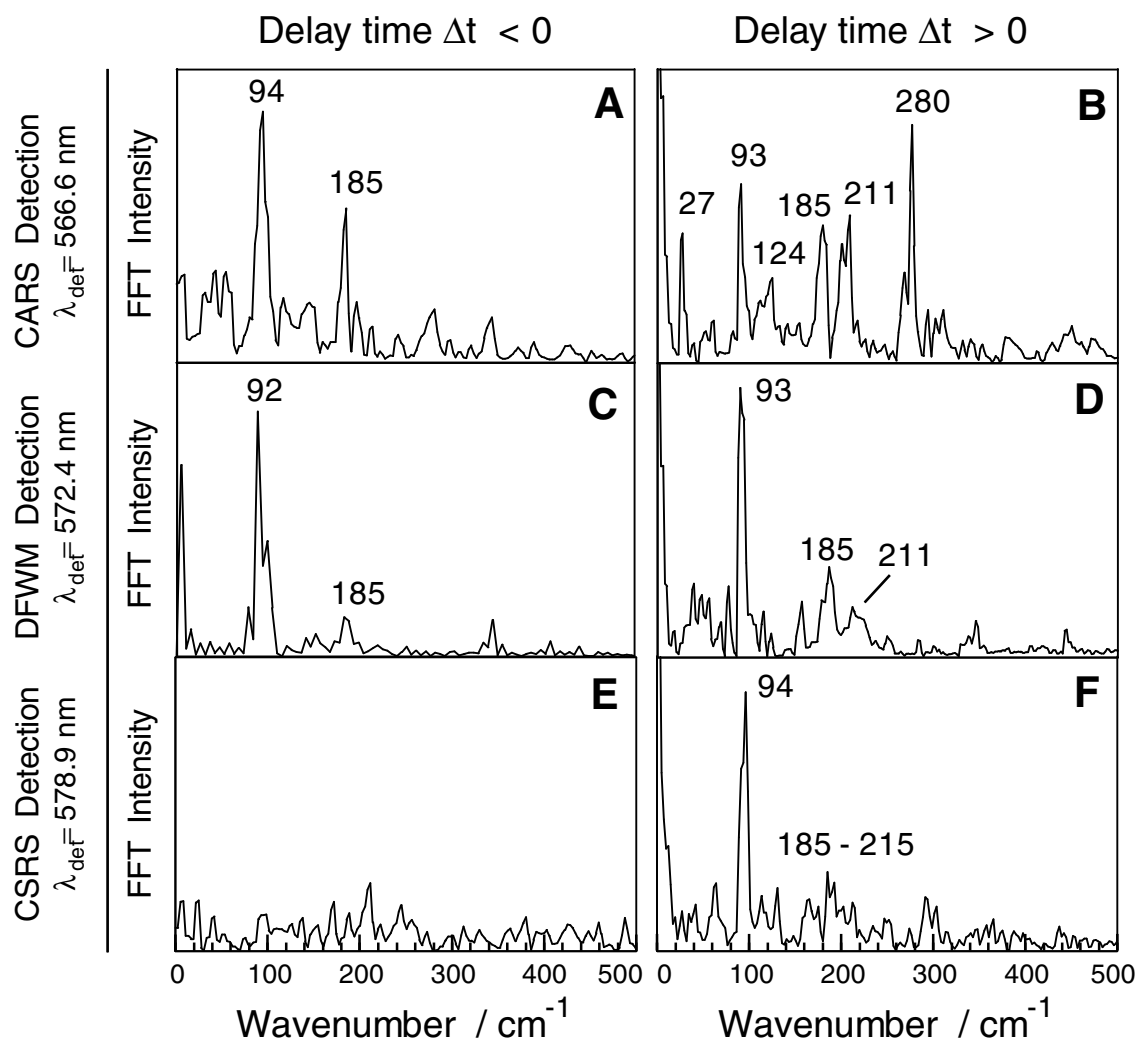


Figure 4.4: Fourier transformations of the transients in Fig. 4.3. Spectra **A** and **B** show the Fourier transformation for the CARS detection wavelength at  $\lambda_{det} = 566.6 \text{ nm}$  for the two possible temporal sequences of the laser pulses,  $\Delta t < 0$  and  $\Delta t > 0$ , respectively. Spectra **C** and **D** show the Fourier transformations for the DFWM detection wavelength at  $\lambda_{det} = 572.4 \text{ nm}$  and spectra **E** and **F** for the CSRS detection wavelength at  $\lambda_{det} = 578.9 \text{ nm}$  for the respective delay times.

show a much stronger contribution of the electronic ground state dynamics than the DFWM transient recorded at  $\lambda_{det} = 572.4$  nm, with oscillations of 160 fs and a corresponding peak in the Fourier transformation in panel B in Fig. 4.4 at  $211$   $\text{cm}^{-1}$ . This rising contribution of the ground state dynamics is attributed to the growing contribution of a CARS process. This will be discussed in greater detail in the section below. Furthermore, the Fourier transformation shows two peaks at 93 and  $185$   $\text{cm}^{-1}$  which cannot be attributed to a CARS process. These peaks are designated to a DFWM process driven by the blue flanks of the laser pulses, and reflect the dynamics of the excited B-state. The components at 27, 124 and  $280$   $\text{cm}^{-1}$  can roughly be assigned to the sum and difference frequencies between the frequency components of the CARS process at  $211$   $\text{cm}^{-1}$  and the components of the DFWM process at 93 and  $185$   $\text{cm}^{-1}$ .

A detection wavelength located on the red side of the signal at  $\lambda_{det} = 578.9$  nm also shows dynamics different than observed at the central wavelength of the signal. Here, the behavior of the transient signal, displayed in panel C of Fig. 4.3, shows the state selectivity that is characteristic of a coherent Stokes Raman scattering process (CSRS). For the CSRS process, a wavelength near the maximum of the spectral profile of  $\mathbf{k}_1$  will act as a *pump* laser while the spectral region in the blue flank of  $\mathbf{k}_2$  serves as an *anti-Stokes* laser. The time variable laser,  $\mathbf{k}_3(\Delta t)$  acts as the second *pump* laser and the coherent Stokes signal is generated in the red flank of the signal. For  $\Delta t < 0$ , the transient and the corresponding Fourier transformation show that virtually no dynamics are present for these delay times. This feature is characteristic of a CSRS process observed in previous experiments in the literature, where this FWM process was explicitly carried out on gaseous iodine.<sup>28-30</sup> At positive delay times,  $\Delta t > 0$  a superposition of ground state and excited B-state dynamics can be observed with oscillations possessing a period of approximately 160 and 355 fs, respectively. The Fourier transformation shows a peak at  $94$   $\text{cm}^{-1}$  which is representative of the excited-B state and a weak band in the region from 185 to  $215$   $\text{cm}^{-1}$  poorly resolves the contributions that are expected of the excited B state at approximately  $185$   $\text{cm}^{-1}$  and of the ground state at about  $211$   $\text{cm}^{-1}$ . This is the state selectivity expected for a Raman resonant CSRS process described in the literature.<sup>28-30</sup> The contribution of a DFWM process, driven by the red flank of the laser pulses superimposed on the CSRS process cannot be ruled out since both schemes possess the same state-

selectivity for this temporal sequence of the laser pulses. This will be discussed in greater detail in the following section.

### 4.3 Discussion: State-Selectivity of Different FWM Processes

The analysis of the broadband signal with the help of a CCD multichannel detection above shows the possibility of characterizing the time-domain behavior of the different spectral channels of an FWM processes. The comparison of the characteristic time-domain behavior at the specific spectral positions in the DFWM signal with the experiments in the literature, where CARS, CSRS and DFWM were explicitly carried out on gaseous iodine, allows for an identification of CARS and CSRS processes in the blue and red flank of the DFWM spectrum.

Of particular interest is the temporal sequence of the laser pulses that was classified as positive delay times ( $\Delta t > 0$ ) since the preparation of a molecular state by the a pulse pair ( $\mathbf{k}_1, \mathbf{k}_2$ ) brings the influence of a Raman resonances into the selectivity of the states prepared by the respective FWM process. As described in sections 2.2.1 and 2.2.2, the consideration of Raman resonances in the multi-color schemes of CARS and CSRS call for the comparison of schemes that utilize virtual states for the realization of these processes versus schemes that take place in resonance to the molecular states offered by the system.<sup>28,45,56,57,81</sup> In the DFWM, CARS and CSRS transients shown in Fig. 4.3 and the respective Fourier transformations in Fig. 4.4, the DFWM process for  $\Delta t > 0$  shows that there is no preference between preparation and interrogation of wave packets on the electronically excited and ground state potential. Since the utilization of Raman resonances is not possible for DFWM, there is no preference between the formation of ground state versus B-state population gratings, described in the Feynman diagrams of Figures 2.2 and 2.3 (see pages 15 and 16). Despite the possibility of Raman resonances in the CSRS process, the transient and Fourier transformation of this process for  $\Delta t > 0$  in panel C of Fig. 4.3 and panel F of Fig. 4.4, respectively, show wave packet dynamics in the excited B and ground state potential. This can be attributed to the scenarios given by the Feynman diagrams **B** and **C** in Fig. 2.8 on page 28, that are in full resonance to the states of the molecular system. Here the possibility of preparing and interrogating wave packets in the excited B-

state and the electronic ground state potentials is shown by the respective Feynman diagram. The contribution of Feynman diagram **A** to the CSRS process, showing a scenario that utilizes a virtual state is difficult to evaluate since both potentials are already accessed by the resonant processes given by diagram **B** and **C**.

For the CARS process, the Raman resonance allows for a higher selectivity than in the case of DFWM or CSRS. The Feynman diagrams **A-C** in Fig. 2.7 on page 24 describe the three possible scenarios for the color scheme of the CARS process for  $\Delta t > 0$ . While diagrams **B** and **C** show the necessity to utilize a virtual state, diagram **A** shows the preparation and interrogation of a wave packet in the electronic ground state in full resonance to the quantum states of the molecular system. The relevance of the Raman resonant process described by diagram **A** can be seen in the transient for the CARS detection at  $\lambda_{det} = 566.6$  nm in Fig. 4.3. Here, the strongest ground state contribution of all detection wavelengths can be seen in a vibrational period of 160 fs, characteristic of a wave packet in the electronic ground state. This is also evident in Fig. 4.5, where the continuous change in the dynamics, as the detection wavelength is varied from the central wavelength to the blue flank of the signal, shows an increasing ground state contribution. The vibrational period of 160 fs associated with the ground state potential is marked with arrows in the transients of Fig. 4.5, in order to emphasize the growing contribution of the CARS process for the blue-shifted detection wavelengths. The effect of a stronger CARS process can also be seen in the comparison of the Fourier transformations in Fig. 4.4. The amplitude of the band at approximately  $210\text{ cm}^{-1}$ , that corresponds to the energy spacing of the vibrational states of the ground state potential, is clearly stronger for the dynamics detected in the blue flank of the signal than at any other detection wavelength. The other bands in the Fourier transformation of the transient detected at  $\lambda_{det} = 566.6$  nm can be attributed to a DFWM process driven by the blue flanks of the laser pulses at this wavelength and sum and difference frequencies of CARS and DFWM processes. The possibility that these excited state dynamics are the result of a CARS process can be ruled out by comparisons to experiments in the literature, where a CARS process on gaseous iodine only shows dynamics in the electronic ground state for  $\Delta t > 0$ .

In summary, the generation of the coherent Raman processes of CARS and CSRS parallel to the DFWM process, allows for a direct comparison of these FWM schemes. This is valuable for the analysis of the state-selectivity, that presents itself in the

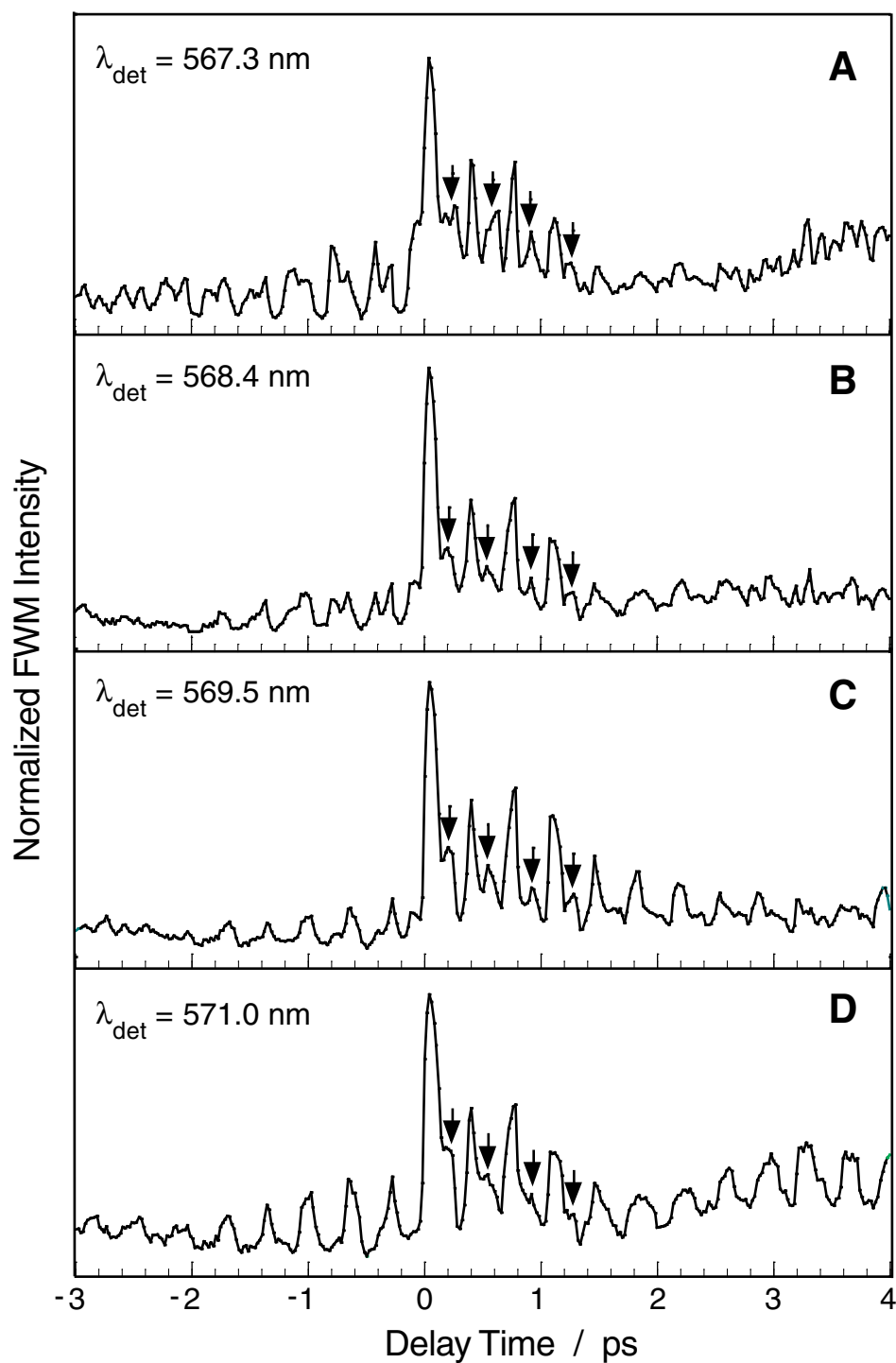


Figure 4.5: Diagrams A-D show four cross-sections made along the time axis of the contour plot in Fig. 4.2. The cross-sections illustrate the growing contribution of ground state dynamics as the detection is shifted from the central wavelength at  $\lambda_{\text{det}} = 572.4 \text{ nm}$  to the blue flank of the FWM signal. Arrows mark the oscillations that are exclusively the result of a wave packet in the electronic ground state of iodine.

preparation of vibrational wave packets on different electronic potentials of the molecular system. Here, the possibility of simultaneously generating all three FWM processes under controlled experimental conditions allows for slight changes in experimental parameters, such as the chirp, to be ruled out as a reason for the changing state-selectivity between the different FWM techniques. The agreement to experiments described in the literature, that show the selectivity of CARS dominated by the process described by Feynman diagram **A** in Fig. 2.7 on page 24, is the most significant result of the experiments presented above. This dominant contribution of a single Feynman diagram to the CARS process, shows the significance of a Raman resonances in comparison to processes that utilize virtual states. The concept, that Raman resonances lead to relevant contributions to the signal intensity of a FWM process while processes utilizing virtual states will not, was addressed in this chapter in the simple molecular system of gaseous iodine. This concept will further be developed in the next chapter, where this effect will be used to utilize CARS as a mode-selective probe of non-adiabatic dynamics.





## Chapter 5

# Non-adiabatic Transitions in Polyatomic Molecules

The mechanism of radiationless transitions between the electronic states of a molecular system has been the object of intensive theoretical and experimental studies in the field of molecular spectroscopy.<sup>4-11</sup> The precise mechanism with which two electronic states in a molecular system are coupled, facilitating a radiationless transition between these electronic states, is rooted in the breakdown of the Born-Oppenheimer approximation.<sup>1</sup> In section 2.3.2 of chapter 2, it was shown that the coupling of electronic and nuclear degrees of freedom is possible in regions where two potential energy surfaces approach one another energetically. Here, nuclear dynamics and electronic transitions will take place on similar time scales due to the equivalent energy spacing of the electronic and vibrational states involved. This mechanism of coupling calls for a revision of the adiabatic picture based on the Born-Oppenheimer approximation in which electronic states do not influence one another. In this case, the formulation of a non-adiabatic picture of electronic states coupled via nuclear motion is necessary.<sup>7,64,65</sup> In the non-adiabatic picture, the relevance of nuclear motion in radiationless transitions such as internal conversion is evident, since it is the mechanism that makes electronic transitions of this type possible.

It is precisely this coupling of nuclear motion to electronic transitions that plays a decisive role in numerous photochemical and photobiological processes such as vision and photosynthesis.<sup>12-14,41,86-89</sup> The nuclear motion involved in processes such as internal conversion defines the reaction coordinate along which photochemical reactions take place, and the degree of coupling will determine the rates of and therefore

the yields in the different product channels of photoinduced reactions.<sup>68,69,90,91</sup> In photobiological processes, it is the strong coupling of specific vibrational modes to an ultrafast electronic transition in the respective chromophore that allows for the high efficiency observed for these processes.<sup>15</sup> Here, the mechanisms that lead to statistical distributions such as internal vibrational energy distribution and cooling processes can be avoided due to the ultrafast time scale of the transition. With the above mentioned, the development of time resolved spectroscopic methods capable of exploring the role of nuclear motion in electronic transitions is of great interest. The following chapter will explore two different time-resolved, third-order optical spectroscopic methods for exploring the dynamic aspects of nuclear motion in radiationless electronic transitions using *all-trans*- $\beta$ -carotene, a molecule that plays a substantial role in photosynthesis.<sup>88</sup>

## 5.1 The System: $\beta$ -Carotene

It is the polyene backbone of *all-trans*- $\beta$ -carotene that presents the most dominate structural unit in this molecular system. This can clearly be seen in the molecular representation shown in panel A of Fig. 5.1, that displays the electronic ground state structure.<sup>92-94</sup> The polyene structure of  $\beta$ -carotene extends into the two cyclohexenyl-rings that are located at the ends of the polyene chain. Together with these ring units,  $\beta$ -carotene possesses a center of inversion explicitly shown in the representation of panel A of Fig. 5.1. Due to this, selection rules make Raman transitions for vibrational modes in the electronic ground state symmetry forbidden for ungerade modes. Vibrational modes with gerade symmetry are Raman-active and specific vibrational modes show a strong resonance enhancement for resonance Raman transitions due to the advantageous Franck-Condon factors. This can be seen in the resonance Raman spectrum of  $\beta$ -carotene in *n*-hexane solution (*vide infra*).

Here, the vibrational modes with large amplitude motion in the symmetric stretch mode of the C-C and C=C bonds in the polyene unit are clearly the Franck-Condon active modes for the Raman excitation that utilizes the  $S_2 \leftarrow S_0$  electronic resonance. In panel B of Fig. 5.1, transient absorption measurements performed by Kispert and coworkers on  $\beta$ -carotene in 3-menthylpentane glass at 20°K show the strong influence of the C=C symmetric stretch mode on the  $S_2 \leftarrow S_0$  optical transition 10 ps after

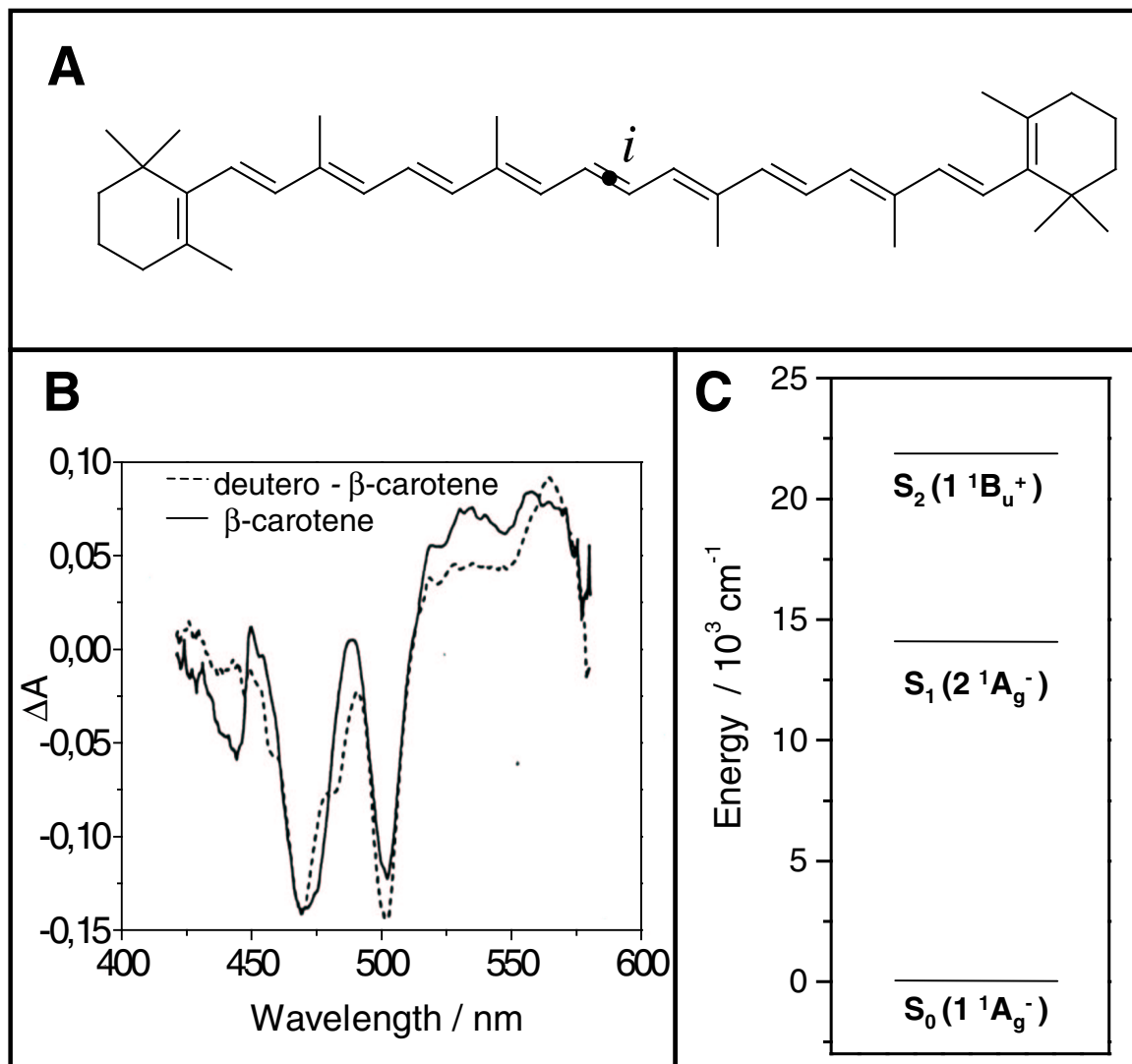


Figure 5.1: (A) Structural representation of *all-trans*- $\beta$ -carotene (B) Transient absorption spectrum of  $\beta$ -carotene in 3-methylpentane glass at 20°K measured 10 ps after photoexcitation into the  $S_2$  state by Kispert and coworkers.<sup>95</sup> The transient absorption shows the ground state bleach in the region from approximately 425 to 510 nm via the  $S_2 \leftarrow S_0$  optical transition and a transient absorption of the  $S_n \leftarrow S_1$  transition from 510 to 600 nm. (C) Schematic energy diagram of the electronic states of  $\beta$ -carotene relevant for the experiments presented in this work.

photoexcitation.<sup>95</sup> In the spectral region of the ground state bleach (425 to 510 nm), the vibronic structure which can be associated with the energy spacing of vibrational states of the C=C symmetric stretch mode can clearly be seen.

Panel C of Fig. 5.1 shows the energy diagram of the electronic states of  $\beta$ -carotene relevant for the experiments presented in this chapter. Here, the second excited singlet state,  $S_2$  ( $2B_u^+$ ) mentioned above, shows an energy of approximately  $22000\text{ cm}^{-1}$ . The energy of this electronic state varies strongly with the attributes of the solvent environment. Experiments described in the literature show that the  $S_2$  state is stabilized by polar solvents ( $22030\text{ cm}^{-1}$ , acetone), while the energy of this state is elevated by non-polar environments ( $22220\text{ cm}^{-1}$ , *n*-hexane).<sup>96</sup>

The precise energy of the first excited singlet state,  $S_1$  ( $2A_g^-$ ) has been the object of extensive research, since the symmetry of this state makes single-photon transitions to the electronic ground state forbidden, ruling out fluorescence and single-photon absorption measurements as methods for determining the energy of this state. Time-dependent measurements that utilize the energy gap rule in combination with the rate of  $S_1/S_0$  internal conversion determine the energy of this state at approximately  $14100\text{ cm}^{-1}$ .<sup>66,86</sup> Further experiments have shown that the energy of this state is insensitive to the polarity of the environment.<sup>97</sup> The  $S_1$  state exhibits a strong transient absorption to a set of poorly characterized electronic states referred to as  $S_n$  states. This  $S_n \leftarrow S_1$  absorption is red-shifted to the  $S_2 \leftarrow S_0$  transition, which can be seen in the transient absorption spectrum in panel B of Fig. 5.1 in the spectral region of 510 to 600 nm. Here, the  $S_1$  state is populated through internal conversion through the optically accessible  $S_2$  state. The  $S_1$  Raman spectrum has been measured in the groups of Hashimoto and Koyama, utilizing this  $S_n \leftarrow S_1$  electronic transition (*vide infra*).<sup>66,98,99</sup> Shifts in the  $S_1$  Raman bands relative to the Raman bands of the electronic ground state give insight into the role of specific modes in the coupling of the  $S_2$ ,  $S_1$  and  $S_0$  states, which will be discussed in detail in this chapter.

It is the electronic structure of  $\beta$ -carotene described above, that allows this molecule to fulfill a variety of essential functions in the process of photosynthesis.<sup>14,88,99</sup> The close proximity in energy of the  $S_2$  and  $S_1$  states in  $\beta$ -carotene to the  $Q_x$  and  $Q_y$  bands of chlorophyll A and B, allow for energy transfer between these two types of molecules via dipole/dipole coupling and electron exchange mechanisms. In photosystem II, one of the light harvesting units in photosynthesis,  $\beta$ -carotene and chlorophyll systems act

as the active chromophors. Here, the spatial proximity of these two types of molecules in this photo-system, together with the possibility of an energy exchange via the energy transfer channels described above, allow  $\beta$ -carotene and related carotenoids to act as (i) auxiliary light-harvesting pigments, with energy transfer to chlorophyll molecules, (ii) dissipators of excess photo-energy collected by chlorophyll units, (iii) photo-protectors via the quenching of chlorophyll triplet states and (iv) scavenger of singlet oxygen.<sup>88</sup> Here, the  $S_1/S_0$  internal conversion in  $\beta$ -carotene, which will be the object of the experiments described below, plays an important role in the mechanisms that allows  $\beta$ -carotene to fulfill these photobiological functions.

## 5.2 The Role of Specific Vibrational Modes During an Internal Conversion Process

In the experiments presented in chapter 4, time resolution and with this, the information about the dynamics of a molecular system, was attained by introducing a delay time between the lasers involved in the four-wave mixing scheme. In the following, the four-wave mixing scheme, in this case coherent anti-Stokes Raman scattering (CARS), is not resolved in time. Here, the three laser pulses involved in the CARS process interact simultaneously with the molecular system of interest and time resolution is attained by introducing a fourth, time variable laser pulse into the experimental scheme, that is independent of the CARS process. This configuration will be referred to in the following as a *pump-CARS* scheme, in analogy to the classical *pump-probe* scheme used in time-resolved spectroscopy. In the *pump-CARS* scheme, an *initial pump* laser pulse brings the molecular system into the state of non-equilibrium and initiates the dynamics that are interrogated with the CARS process, which fulfills the role of a probe mechanism. The use of a complicated, three-laser process such as CARS for a probe mechanism, versus the strategy of a single-laser probe that projects the time-dependent system into a set of final states, allowing for the detection of a time-dependent fluorescence, absorption, ion-signals, photoelectron, etc.<sup>16,17</sup> can be justified by the possibility of tuning the CARS probe to the energy of specific vibrational modes in the molecular system of interest. With this, the possibility of discriminating between the dynamics taking place within the individual vibrational modes of the system is introduced. Here, it is possible to extract information about

the role of individual modes in an radiationless transition such as internal conversion and gain direct insight into the precise mechanism of this type of transition.

The interest in gaining information about molecular dynamics that is specific to certain vibrational modes of polyatomic molecules has led to the development of different experimental strategies. A variety of experimental schemes allow for exploring processes such as internal conversion, photo-dissociations, electron transfer and cooling processes selectively with regards to the role of specific vibrational modes. Many techniques utilize Raman transitions for the interrogation of the transient species in order to attain mode specific information. In one possible scenario, the system is pumped into the state of non-equilibrium with a pump laser pulse and probed with a linear Raman transition. In the group of Zinth, vibrational relaxation processes in polyatomic molecules in the condensed phase were investigated on a femtosecond time scale by using an infrared laser pulses, resonant to the energy spacing of C-H stretching modes, in order to excited this form of nuclear motion.<sup>100</sup> The vibrationally excited states were probed with a second laser pulse utilizing a Raman transition that results in an anti-Stokes signal from the transient vibrational states. Here, the time scale of vibrational energy redistribution for specific modes could be determined, giving valuable information about the energy flow and relaxation processes in polyatomic molecules. In the group of Elsaesser, a similar experimental scheme on the picosecond time scale was used to explore the repopulation of vibrational modes after pumping *para*-nitroaniline into a charge transfer state.<sup>101</sup> This is achieved by observing the time-dependent anti-Stokes signal from different vibrational modes in the electronic ground state, which was generated by a time-delayed probe laser, that is in resonance to the electronic ground state absorption. Here, the kinetics of the different modes allows for determining the mechanism with which different vibrational modes are populated. These kinetics show the time scale of internal vibrational energy redistribution among the different vibrational modes.

Linear Raman transitions have also been used extensively to attain frequency-resolved measurements of transient electronic states. Here, the Raman shift and linewidth analysis of the Raman bands in excited electronic states give information about the role of the different vibrational modes in the relaxation processes such as internal conversion after photo-excitation. This type of experiments has been carried out by a number of groups but specifically for  $\beta$ -carotene, which is the molecular

system that will be explored with the experiments described in the following, the groups of Hashimoto and Koyama have utilized this type of experimental scheme to investigate the vibrational modes of the  $S_1$  state in  $\beta$ -carotene.<sup>66,99,102</sup>

There are also a number of experimental schemes described in the literature, that utilize nonlinear Raman interactions for exploring transient states and their vibrational dynamics. Recently, Aoki and Hashimoto used stimulated resonance Raman (SRR) transitions on the femtosecond time scale to explore the dynamics of the C=C symmetric stretch mode, involved in the relaxation processes when  $\beta$ -carotene is excited into the  $S_2$  state and relaxes back into its electronic ground state.<sup>103,104</sup> For this, three laser pulses interact with the system: the first pulse excites  $\beta$ -carotene into the  $S_2$  state, the second laser pumps a Raman transition in resonance to the  $S_1$  state absorption and a third, white light pulse, stimulates the Raman transition initiated by the second pump pulse. The population dynamics of the C=C symmetric stretch mode was monitored at the corresponding spectral position in the white light. Here, the dynamics of this mode in the  $S_1$  and  $S_0$  state could be examined for the relevant internal conversion and cooling processes taking place. In the group of Elsaesser, third-order Raman processes such as coherent anti-Stokes Raman scattering (CARS) were used to attain information about Raman shifts in excited electronic states.<sup>105</sup> For example, diphenylhexatriene was pumped into the  $S_2$  state and the wavenumber-resolved CARS spectrum of the  $S_1$  state is monitored as a function of the delay time between the initial pump laser pulse and the two lasers participating in the CARS process. Similar experiments were performed by Funk *et. al.* on the nanosecond time scale, where the CARS probe extracted spectral information about triplet states of polycyclical aromatic systems that were populated by pumping excited singlet states that undergo intersystem crossing.<sup>106</sup>

There are also a variety of experimental schemes that do not use Raman transitions for attaining mode-specific information of transient states. Here, time-resolved photoelectron spectroscopy has proven to be a powerful method for observing internal conversion selectively with respect to the nuclear dynamics coupled to this type of electronic transition.<sup>11</sup> For this, the dynamics taking place in the two non-adiabatically coupled electronic states can be monitored by projecting these states into the well characterized ion continuum. A pump laser prepares an excited electronic state that engages in an internal conversion to an energetically lower lying

electronic state. A second, time delayed laser pulse ionizes either of the two electronic states involved in the internal conversion process. If the two electronic states correlate to different, energetically well separated ion states according to Koopman's theorem, then the respective photoelectron spectra are energetically well separated. Due to this, the photon electron spectra clearly show the vibrational structure of the corresponding electronic states that were ionized. The dynamics taking place in the vibrational modes of either electronic state can be monitored at the respective spectral position of the photo-electron spectrum. Transient infrared absorption spectroscopy applied by the group of Sundström has also shown the capability of extracting valuable, mode-specific information from transient electronic states.<sup>107,108</sup> For this, a pump laser excites spheroidene into its  $S_2$  state, which shows a fast internal conversion into the  $S_1$  state. The  $S_1$  state is probed by a second probe laser that is resonant to the  $S_2 \leftarrow S_1$  absorption. The vibronic structure in the transient  $S_1$  infrared absorption spectrum together with the dynamics of the  $S_1$  state monitored at different wavelength in the absorption spectrum, give important information about the relative nuclear displacement of the  $S_2$ ,  $S_1$  and  $S_0$  states for different vibrational modes.

A significant experiment for establishing third-order interactions as a probe mechanism of transient states in a *pump-probe* scheme was performed in the group of Zewail.<sup>42</sup> In the experiment, degenerate four-wave mixing (DFWM) was used as a probe mechanism for probing the dissociation dynamics of sodium iodide in the gas phase. Here, the mechanism and state selectivity with which third order interactions interrogate vibrational states in transient populations was established. This was accomplished by the comparison of *pump*-DFWM and *pump-control*-DFWM schemes with classical *pump-probe* experiments using laser induced fluorescence in the detection of the probe step.

In the experiment presented in the following, vibrational modes in the electronic ground state of  $\beta$ -carotene will be monitored as they are repopulated subsequent to the  $S_1/S_0$  internal conversion with a *pump*-CARS strategy. The goal of this experiment is to establish the CARS process as a probe mechanism for molecular dynamics, capable of selectively interrogating the population flow taking place in a specific vibrational mode. The experiment further aims to attain information about the role of certain vibrational modes in the  $S_1/S_0$  internal conversion and with this, give a better



picture of the precise nuclear coordinates associated with this electronic transition.<sup>109</sup>

### 5.2.1 Methodology of the *Pump*-CARS Scheme

As shown in Fig. 5.2, the *pump*-CARS scheme is characterized by the use of four pulsed laser fields, one of which is used as an *initial pump* laser (**IP**) that initiates the dynamics in a molecular system by bringing it in a non-equilibrium state. Three further laser pulses, (**1-3**) serve as a *probe* mechanism of the dynamics excited by the *initial pump* by participating in a CARS process. For time-resolution, a variable time delay,  $\Delta t$  is introduced between the *initial pump* pulse and the three laser pulses of the CARS process, that interact simultaneously with the system. The four laser pulses are focused into a 0.1 mM solution of  $\beta$ -carotene in *n*-hexane, located in a rotating sample cell (100 Hz) with a cell length of 0.5 mm. The coherent anti-Stokes signal was monitored in the phase matched direction  $\mathbf{k}_{aS} = \mathbf{k}_1 - \mathbf{k}_2 + \mathbf{k}_3$  as described in section 3.2. The spectral position of the laser pulses involved in this experimental scheme are shown in Fig. 5.3, within the ground state absorption spectrum of  $\beta$ -carotene in *n*-hexane. Further details of the experimental setup used to realize the *pump*-CARS scheme are given in chapter 3.

As shown in Fig. 5.2, an *initial pump* laser (**IP** in Fig. 5.2,  $\lambda_{IP} = 400$  nm, FWHM = 250 fs, 400 nJ), is resonant to the  $S_2 \leftarrow S_0$  optical transition and the interaction of this laser with the sample brings the system in a non-equilibrium state by transferring population from the electronic ground state,  $S_0$  to the first optically accessible  $S_2$  state. The subsequent relaxation dynamics from the  $S_2$  into the  $S_1$  state and vibrational cooling within the  $S_1$  state, taking place after photo excitation of  $\beta$ -carotene with the *initial pump* laser, have been explored in this work with transient population gratings, described in sections 5.4 and in great detail with other experimental schemes described in the literature.<sup>96,108,110,111</sup> These works determine a time constant for the  $S_2/S_1$  internal conversion of  $\beta$ -carotene in *n*-hexane to  $\tau_{IC}(S_2/S_1) \approx 180$  fs and characterize the cooling processes in the  $S_1$  state with a global time constant of  $\tau(\text{cooling}) \approx 600 - 750$  fs.

The precise mechanism of the subsequent  $S_1/S_0$  internal conversion and the following vibrational cooling and internal vibrational energy redistribution (IVR) processes in the  $S_0$  state will be explored in this experiment by interrogating these dynamics, mode-selectively via a CARS probe process. This is accomplished by monitoring the

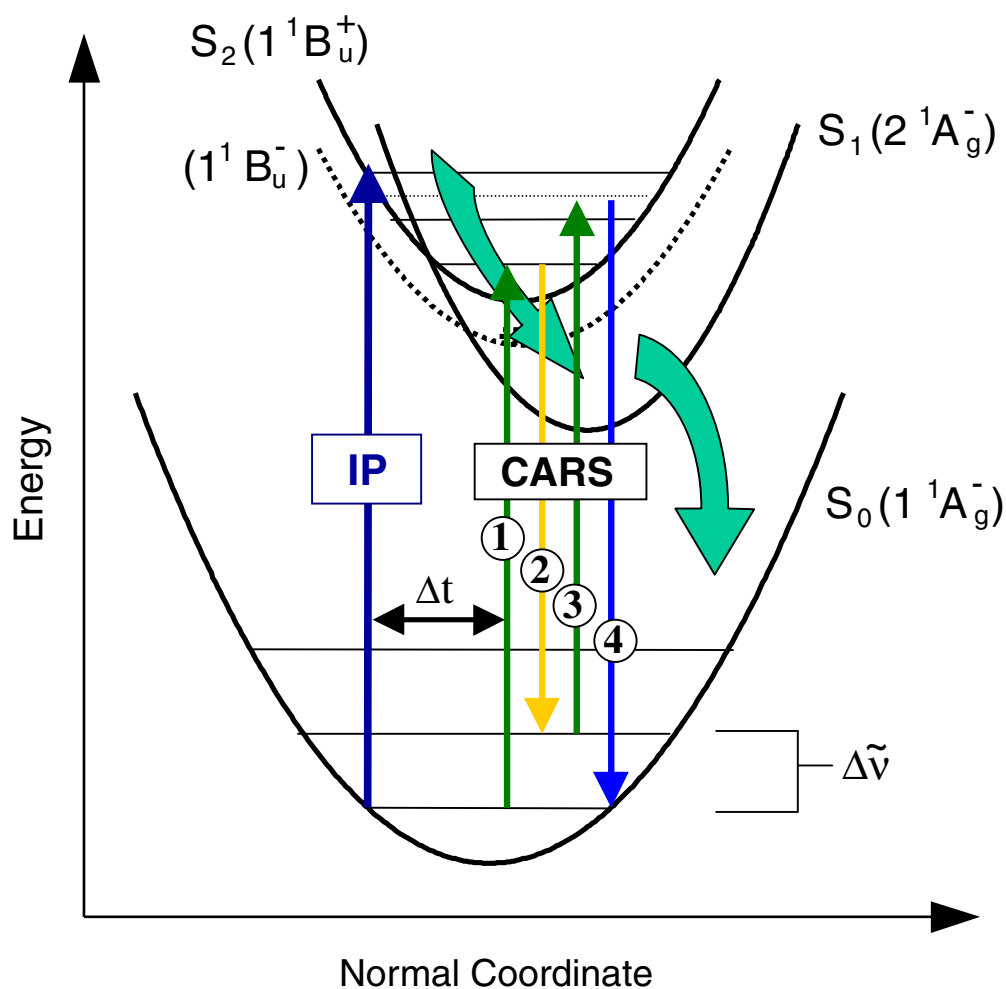


Figure 5.2: An *initial pump* laser, **IP** ( $\lambda_{IP} = 400$  nm, FWHM = 250 fs, 400 nJ), transfers population to the first optically accessible  $S_2$  state. The subsequent  $S_1/S_0$  internal conversion, vibrational cooling and IVR is interrogated mode-selectively via a time-variable CARS process consisting of two *pump* lasers (**1** and **3**,  $\lambda_{pu} = 510$  nm, FWHM = 70 fs, 60 nJ) that also utilize the  $S_2 \leftarrow S_0$  optical transition and a *Stokes* laser (**2**,  $\lambda_S = 530$ -550 nm, FWHM = 70 fs, 50 nJ) which allows for the CARS process to be tuned to different normal modes ( $\Delta\tilde{\nu}$ ) in the  $S_0$  state. The CARS probe is characterized by a FWHM of 120 fs in the convolution of **1-3**. Lasers **1-3** generate the CARS signal, **4** which is monitored as a function of the delay time, ( $\Delta t$ ) between the *initial pump* laser and the CARS process.

ground state bleach induced by the *initial pump* laser and the subsequent dynamics of repopulation into the vibrational modes of the electronic ground state with the CARS probe. For this, the laser pulses involved in the CARS process (**1-3** in Fig. 5.2) interact simultaneously with the sample. The CARS probe is characterized with a FWHM of 120 fs in the convolution of **1-3**, giving the time resolution of this probe mechanism. The two *pump* lasers of the CARS process (**1** and **3** in Fig. 5.2,  $\lambda_{pu} = 510$  nm, FWHM = 70 fs, 60 nJ) are also tuned resonant with the  $S_2 \leftarrow S_0$  optical transition (see also Fig. 5.3). In order to monitor the recovery dynamics of a specific vibrational mode in the ground state potential, the wavelength of the *Stokes* laser (**2** in Fig. 5.2,  $\lambda_S = 530 - 550$  nm, FWHM = 70 fs, 50 nJ) is adjusted so that the energy difference,  $\Delta\tilde{\nu}$  between the *pump* and *Stokes* lasers corresponds to the energy spacing of a specific vibrational mode. The mechanism with which the CARS process is able to selectively interrogate specific normal modes has its foundation in the strong enhancement of the CARS signal intensity in the case that the energy difference,  $\Delta\tilde{\nu}$  between the *pump* and *Stokes* laser (**1** and **2**, Fig. 5.2) corresponds to a Raman transition of a vibrational mode in the electronic ground state. The resonance enhancement by means of a Raman transition is the result of an effective projection of an initial population in a vibrational state of a particular vibrational mode (with the quantum number,  $v = n$ ;  $n = 0, 1, 2, 3, \dots$ ), into an intermediate vibrational state ( $v = n + 1$ ) through the interaction with **1** and **2**. In the case of a Raman resonance, an effectively prepared, intermediate vibrational state ( $v = n + 1$ ) of a specific mode will lead to a strong inelastic scattering of the pump laser **3**, and subsequently to the generation of an intense coherent anti-Stokes signal (**4** in Fig. 5.2). The lack of a Raman resonance forces the CARS process to go through a virtual intermediate state, making the generation of the CARS signal out of the initial state ( $v = n$ ) through the interaction with lasers **1 - 3** extremely ineffective. The effect of the Raman resonance enhancement allows the CARS probe to act as a filter that only shows a significant signal intensity for the normal mode to which  $\Delta\tilde{\nu}$  is tuned to. This will be discussed in detail in the following section.

The solid dark line in Fig. 5.4 shows the resonance Raman spectrum of  $\beta$ -carotene in *n*-hexane (0.1 mM), recorded with the 514.5 nm laser line of an argon ion laser. By tuning the energy difference,  $\Delta\tilde{\nu}$  between the *pump* (**1** and **3**) and *Stokes* (**2**) lasers to a value that corresponds to the energy of a specific vibrational mode seen

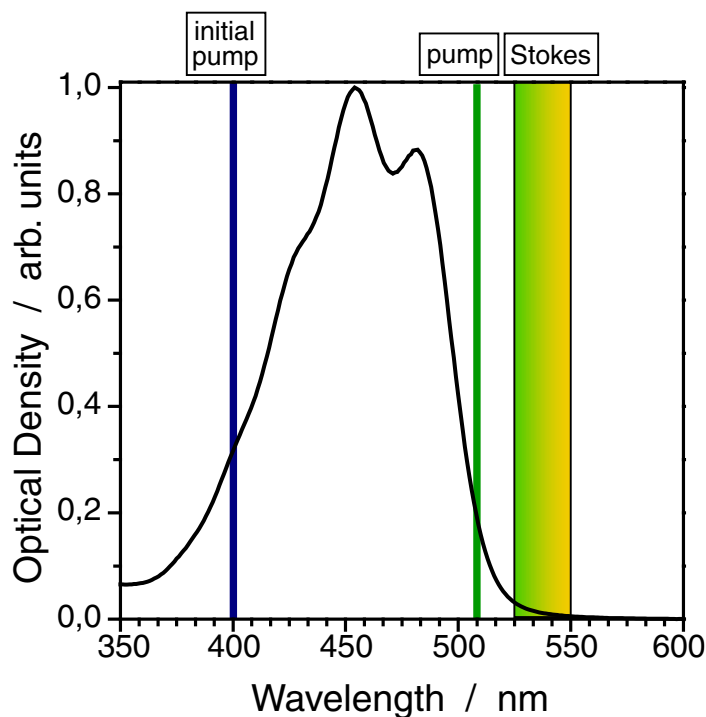


Figure 5.3: Absorption spectrum of the  $S_2 \leftarrow S_0$  optical transition from a 0.1 mM solution of  $\beta$ -carotene in  $n$ -hexane showing the position of the electronic transitions utilized in the *pump*-CARS scheme. The vertical bars show the central wavelength of the *initial pump* laser (400 nm) and the *pump* lasers in the CARS process (510 nm) as well as the variable central wavelength of the *Stokes* laser in the CARS process (530-550 nm).

in the resonance Raman spectrum, the coherent anti-Stokes signal is observed with the corresponding energy shift on the blue side of the *pump* lasers, located at  $\lambda_{pu} = 510$  nm. The resulting CARS signal is coupled into a monochromator and the dispersed signal is detected with a multichannel CCD detector as described in section 3.3. The broken lines in Fig. 5.4 show the spectral profile of four broadband CARS signals tuned to four different  $\Delta\tilde{\nu}$ . These profiles are superimposed on the corresponding spectral positions of the resonance Raman spectrum. The broadband nature of the CARS signal results from the spectrally broad fs laser pulses (**1-3**) that generate the signal. This broadband nature of the pulses allows for all the relevant Raman modes of  $\beta$ -carotene in the  $S_0$  state to be incorporated in one of the four coherent anti-Stokes spectra, shown in Fig. 5.4. For a specific Raman mode, the intensity of

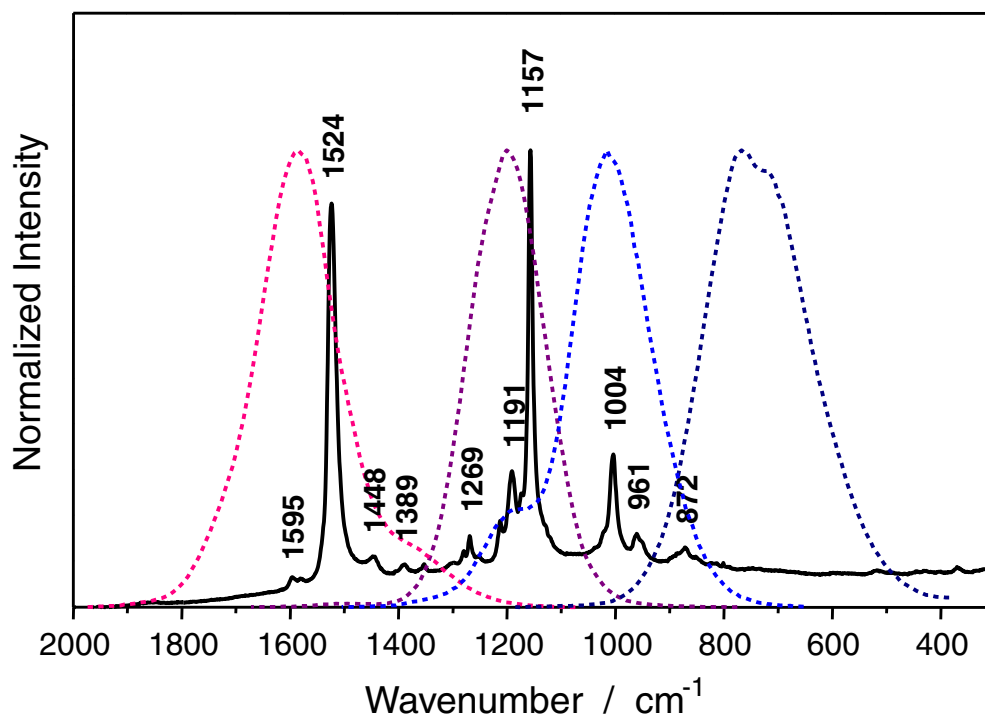


Figure 5.4: Resonance Raman spectrum (solid black line) of  $\beta$ -carotene in *n*-hexane (0.1 mm) and spectral profiles of CARS signals tuned to different Raman modes in the electronic ground state (broken lines) attained with the *pump*-CARS scheme. Here, the CARS spectra that appear on the anti-Stokes side of the pump laser are superimposed on the corresponding position of the Raman spectrum observed on the Stokes side of the pump laser. The spectral profiles of the CARS spectra were taken at  $\Delta t = 1$  ps between the *initial pump* and CARS process. For details see text.

the CARS signal (4, Fig. 5.2 and broken lines in Fig. 5.4) is monitored at a spectral position characteristic for a specific vibrational mode as a function of the delay time,  $\Delta t$  between the *initial pump* and the CARS probe.

For a clear picture of the experimental procedure, the order of events with respect to the delay time are discussed in the following. For  $\Delta t < 0$ , the CARS process interacts with the system before the *initial pump* laser. For this sequence of the lasers, the CARS process probes a system that is in its equilibrium state. At  $\Delta t = 0$ , the *initial pump* laser and the CARS process interact simultaneously with the system. The transfer of population into the  $S_2$  state and the corresponding bleach of the electronic ground state induced by the *initial pump* laser will lead to a depletion

of ground state molecules available for the CARS probe process. This depletion shows itself in a drop in the CARS signal intensity. For delay times  $\Delta t > 0$ , a repopulation of the vibrational states in the electronic ground state via the  $S_1/S_0$  internal conversion and subsequent vibrational cooling and IVR brings the transient molecules back into the probe window of the CARS process. This leads to a recovery of the CARS signal intensity. The recovery dynamics into the  $S_0$  state are observed for five characteristic normal modes that possess enough spectral separation from neighboring modes to be differentiated by the broadband laser pulses. For these vibrational modes, the transient behavior of the CARS signal at the corresponding spectral position is observed as a function of  $\Delta t$ . The transients attained with this method will be presented in the following section.

In order to rule out contributions to the CARS probe from  $S_1$  state vibrational modes that enter the signal due to the weak resonance at  $\lambda_{pu} = 510$  nm to the  $S_n \leftarrow S_1$  optical transition, the CARS process was also resolved in time in the presence of the *initial pump* laser in a control experiment according to the scheme shown in Fig. 5.5. Here, the electronic states interrogated by the CARS probe are examined by determining the Raman modes that contribute to the signal. Since the  $S_1$  and electronic ground state possess characteristic Raman shifts that vary significantly between the respective electronic state, the relative Raman shifts will show the signature of the electronic states interrogated by the CARS probe. These Raman shifts can be seen in Fourier transformation of the time-resolved CARS process.<sup>23,30,112</sup>

The control experiment shown in Fig. 5.5 is realized by setting a fixed delay time,  $\Delta t_1 = 1$  ps between the *initial pump* and the CARS process to allow for a population of the  $S_1$  state. With  $\lambda_{pu} = 510$  nm and  $\lambda_{Stokes} = 540$  nm, the CARS process is tuned to  $\Delta\tilde{\nu} = 1100$   $\text{cm}^{-1}$ , which allows for a coherent superposition of the Raman modes between 1275 and 975  $\text{cm}^{-1}$ , assuming a spectral FWHM of 250  $\text{cm}^{-1}$  in the convolution of *pump* and *Stokes* lasers. The CARS process is resolved temporally by varying the time delay,  $\Delta t_2$  of the second *pump* laser (**3** in Fig. 5.5) relative to the stationary *pump* and *Stokes* laser (**1** and **2** in Fig. 5.5). By monitoring the intensity of the CARS signal (**4** in Fig. 5.5) as a function of the delay time,  $\Delta t_2$  the macroscopic beating between the coherent signals of all the Raman modes contributing to the signal can be observed. This coherent beating structure will give the relative Raman shifts in the Fourier transformation of the transient. The analysis, that will be given

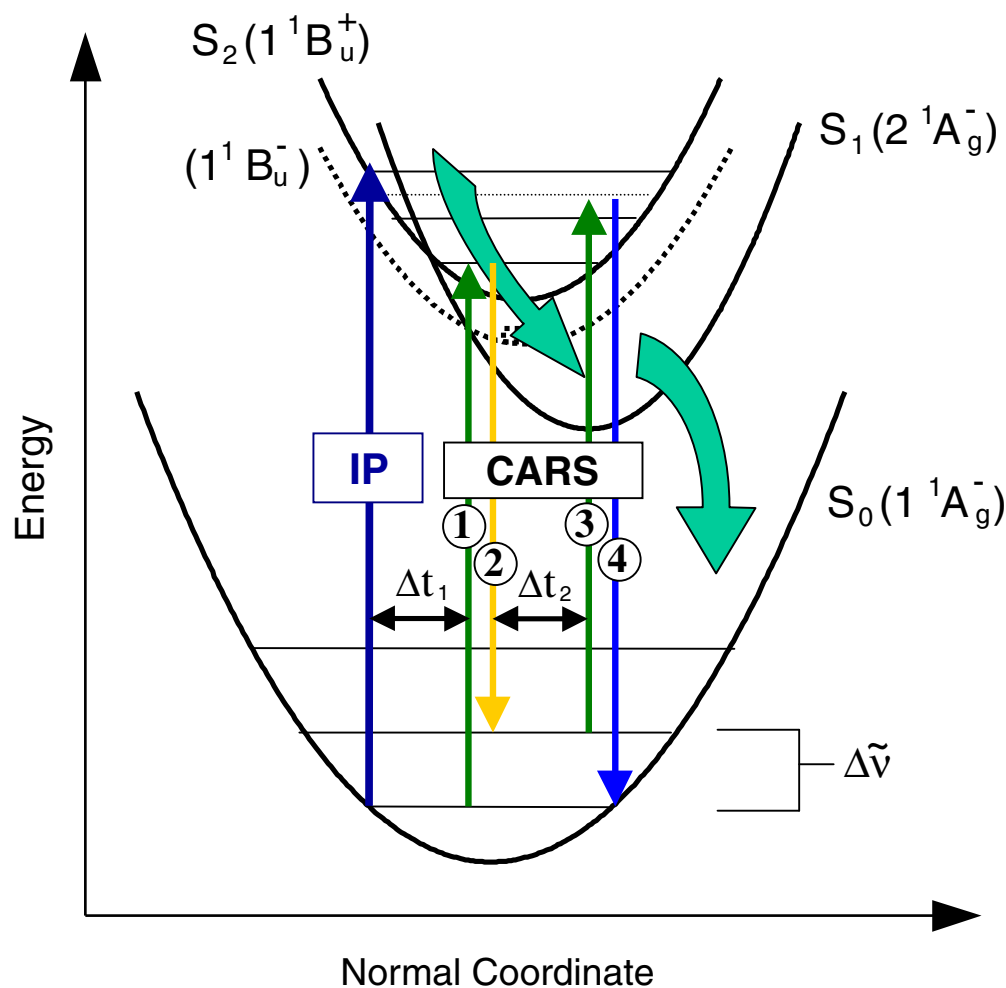


Figure 5.5: Experimental scheme applied for determining the electronic states and Raman modes within these states that are interrogated by the CARS probe. For this the delay time between the *initial pump* laser, **IP** ( $\lambda_{IP} = 400$  nm, FWHM = 250 fs, 400 nJ) and the CARS process (**1** and **3**,  $\lambda_{pu} = 510$  nm, FWHM = 70 fs, 60 nJ; **2**,  $\lambda_S = 530$ -550 nm, FWHM = 70 fs, 50 nJ) is fixed at  $\Delta t_1 = 1$  ps. The CARS process is resolved in time by varying the time delay,  $\Delta t_2$  of **3** relative to the two stationary lasers, **1** and **2** and detecting the intensity of the CARS signal **4** as a function of  $\Delta t_2$ .

in the next section, allows for the electronic states interrogated by the CARS probe to be determined due to the characteristic Raman shifts of the  $S_1$  and  $S_0$  state.

## 5.2.2 Experimental Results: CARS as a Mode-Selective Probe Process in a *Pump-Probe* Scheme

In panels A-E of Fig. 5.6, the transient CARS signal is shown as a function of the delay time,  $\Delta t$  between the *initial pump* laser and the CARS probe, recorded for five different spectral positions of the CARS signal. The spectral positions correspond to the Raman shift of five vibrational modes of  $\beta$ -carotene in the  $S_0$  state shown in Fig. 5.4. In order to characterize the dynamics of the population recovery into the individual normal modes of the electronic ground state, a model was used to fit the transient data of the CARS intensity,  $I_{CARS}$  as a function of the delay time,  $\Delta t$ . The model consists of a temporal response function given by a Gaussian profile convoluted with an exponential function with a time constant,  $\tau$  that characterizes the repopulation dynamics of the electronic ground state for the vibrational mode probed by the CARS process:

$$I_{CARS}(\Delta t; \tau; \sigma) = A \cdot e^{-\frac{(\Delta t)^2}{2\sigma^2}} \otimes e^{-\frac{\Delta t}{\tau}} \cdot H(\Delta t). \quad (5.1)$$

Here, the temporal response function possesses a FWHM given by  $2\sigma = 254$  fs in the Gaussian profile, which corresponds to the convolution of the *initial pump* and the lasers participating in the CARS process. The FWHM was determined experimentally with the help of an optical Kerr gate of the *initial pump* laser with one of the lasers of the CARS process.<sup>113</sup> Furthermore,  $H(\Delta t)$  is a step function positioned at  $\Delta t = 0$ .

The characteristic recovery times,  $\tau$  for the different normal modes are obtained from the fit of equation 5.1 with the experimental data, which is shown in panels A-E in Fig. 5.6. The values of  $\tau$  for the different normal modes are noted in the panel of the respective transient in Fig. 5.6 with the spectral position at which the dynamics were recorded. From the values for  $\tau$  listed in Fig. 5.6, it can be seen that the recovery times are not homogeneous for the different normal modes probed in the experiment.

Before the varying recovery times are interpreted and a model for the repopulation of the ground state vibrational modes can be formulated, the mechanism with which the CARS probe interrogates the transient population will be discussed in detail in



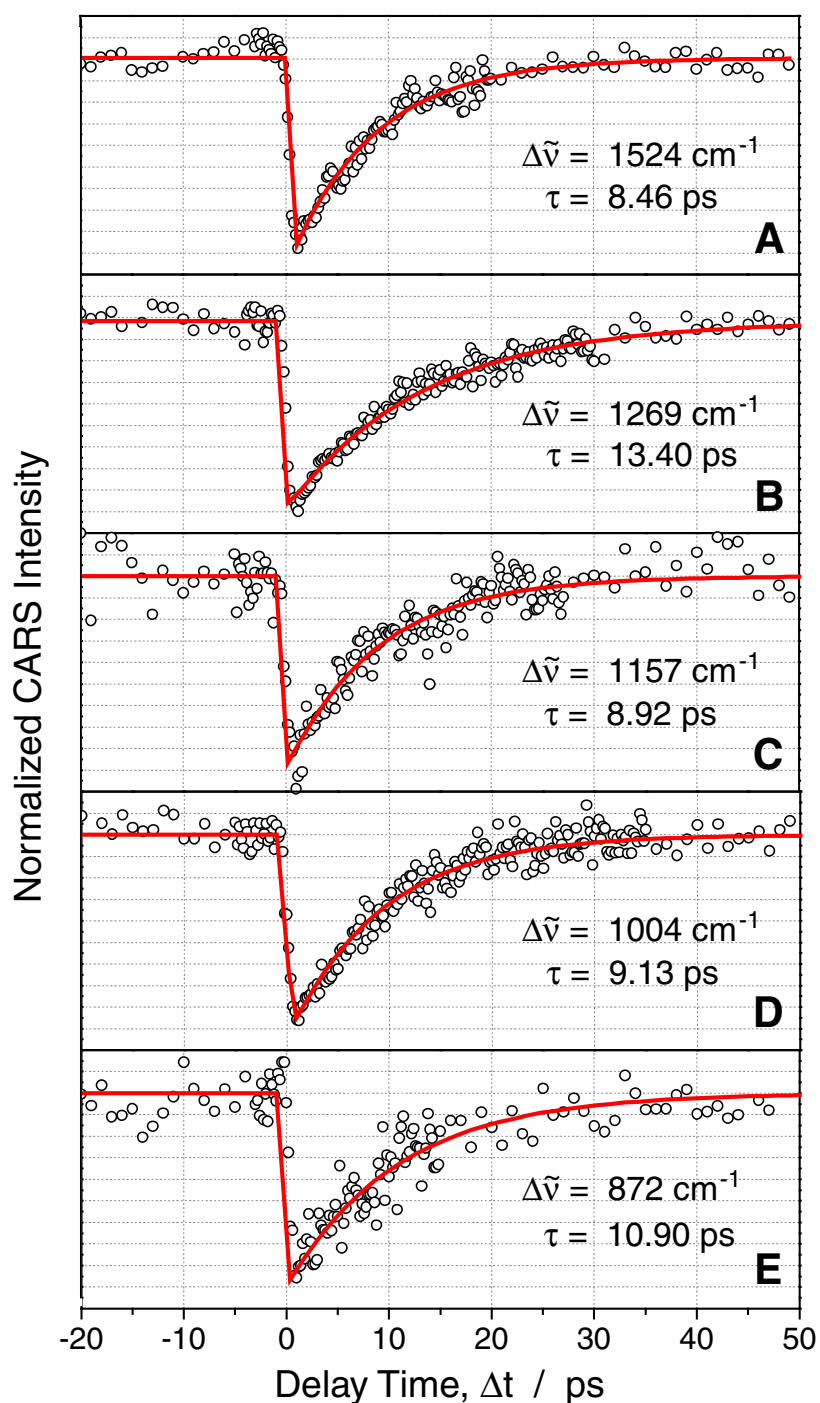


Figure 5.6: Normalized CARS intensity plotted as a function of the delay time,  $\Delta t$  between the *initial pump* and the CARS process. Panels A-E show the transient CARS signal intensity recorded at different spectral positions of the CARS signal,  $\Delta\tilde{\nu}$  which are noted in the bottom left corner along with the time constants,  $\tau$  characterizing the kinetics of the repopulation of the electronic ground state. For details see text.

order to determine the precise dynamics that are characterized with the recovery time,  $\tau$ . This can be explored with the theoretical formalism of time-resolved, third-order interaction that was explicitly developed in chapter 2. Here, the third-order polarization induced by the interaction of the sample with lasers **1-3** in Fig. 5.7, is described by the coherent, anti-Stokes transition (**4** in Fig. 5.7) with the transition dipole,  $\mu_{aS}$  between the respective states:

$$P^{(3)}(t, \Delta t) = \langle g^{(0)} | \mu_{aS} | e'^{(3)} \rangle + cc. \quad (5.2)$$

The notation of the states participating in the CARS process are illustrated in panel A of Fig. 5.7. Here,  $|e'^{(3)}\rangle$  results out of the interaction of  $|g^{(0)}(\Delta t)\rangle$  with the three lasers fields involved with the CARS process (consisting of two *pump* fields,  $E_{pu}$  and the *Stokes* field,  $E_S$ ). All three laser pulses interact with the system at  $\Delta t$  after the excitation with the *initial pump* laser and the notation is simplified to  $E_i(\Delta t) \equiv E_i$ . Furthermore, the notation describing the order of the electronic states are omitted for simplicity giving:

$$P^{(3)}(t, \Delta t) = \langle g(\Delta t) | \mu_{aS} | (\mu E_{pu} \mu E_S \mu E_{pu} | g(\Delta t)) \rangle + cc. \quad (5.3)$$

$$P^{(3)}(t, \Delta t) = \langle g(\Delta t) | \mu_{aS} | e' \rangle \langle e' | \mu E_{pu} | g' \rangle \langle g' | \mu E_S | e \rangle \langle e | \mu E_{pu} | g(\Delta t) \rangle + cc. \quad (5.4)$$

Since all the laser fields involved in the CARS process interact simultaneously with the sample, it will be the population of the initial vibrational state in  $|g(\Delta t)\rangle$ , from which the CARS process is initiated, that governs the time dependence of the polarization in equation 5.4. The sensitivity of four wave mixing as a probe mechanism for the direct population of the initial state is confirmed experimentally in the literature, where Motzkus *et.al.* directly compare a degenerate four-wave mixing probe to the time-resolved data obtained by means of laser induced fluorescence as a probe mechanism.<sup>42</sup> Here, it was established that both methods directly monitor the same transient population.

On this basis, the coefficients,  $c(\Delta t) = c(0) e^{-(t+\Delta t)/2T_1}$  that are dependent on the parametric delay time,  $\Delta t$  are expanded out of the ground state,  $|g(\Delta t)\rangle$  that propagates during the parametric delay time. The phase introduced by the time-dependent wave functions can be ignored in this expansion since the laser pulses do not possess a time resolution that allows for a phase sensitive excitation or interrogation

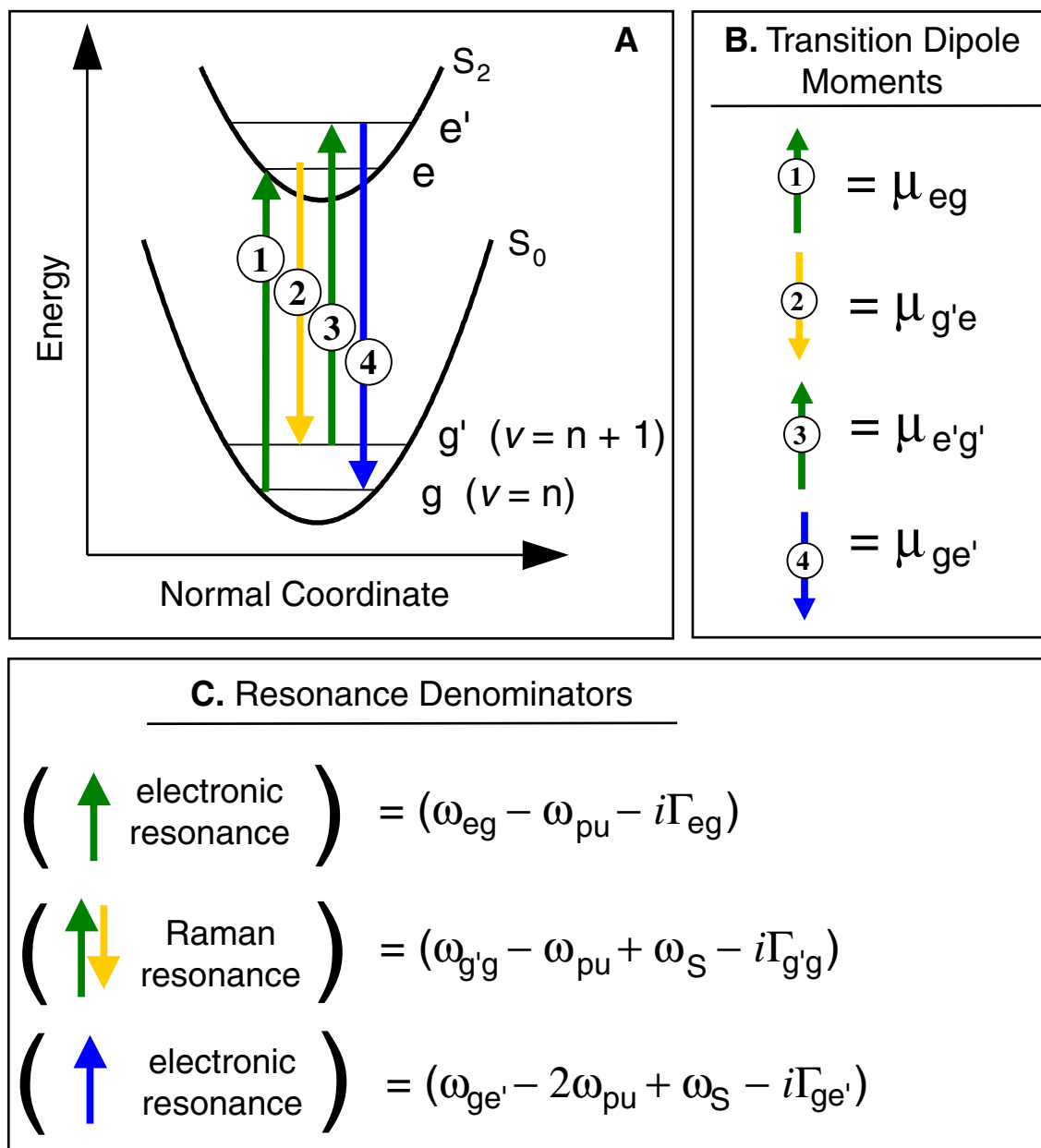


Figure 5.7: **A**. Schematic potential energy diagram showing the CARS process resonant to the  $S_2 \leftarrow S_0$  optical transition in  $\beta$ -carotene. ( $g \equiv$  vibrational state in the  $S_0$  with  $v = n$ ;  $g' \equiv$  vibrational state in the  $S_0$  with  $v = n + 1$ ;  $e \equiv$  vibrational state in the  $S_1$ ;  $e' \equiv$  higher excited vibrational state in the  $S_1$ .) **B**. and **C**. Illustrations of the terms in equation 5.7 that are relevant for the selectivity of the CARS probe.<sup>49,56,57</sup> **B** shows the transition dipole moments and **C** the resonance denominators in the CARS process. ( $\mu \equiv$  transition dipole moment;  $\omega \equiv$  transition frequency or laser frequency; and  $\Gamma \equiv$  damping constant for the respective transition.)

of the vibrational states.

$$P^{(3)}(t, \Delta t) = c^*(0)c(0)e^{-\Delta t/T_1} \cdot \langle e^{-t/2T_1} \cdot g | \mu_{aS} | e' \rangle \langle e' | \mu E_{pu} | g' \rangle \langle g' | \mu E_S | e \rangle \langle e | \mu E_{pu} | e^{-t/2T_1} \cdot g \rangle + cc. \quad (5.5)$$

Important to further consider are the vibrationally excited states that will be significantly populated due to the population flow out of the  $S_1$  state during the  $S_1/S_0$  internal conversion. For this, the interaction of the CARS probe with the normal modes at a vibrational quantum number of  $v = 0$  and the interrogation of vibrational hot modes ( $v \geq 1$ ) needs to be considered. Due to this,  $P^{(3)}(\Delta t)$  must be written as the sum over all vibrational modes  $i$  and the vibrational states,  $v_i$  of these modes accessed spectrally by the *pump* and *Stokes* laser. The terms left in the integration over the spatial coordinates can be summarized in an amplitude factor,  $A_{i,v}(t)$  and equation 5.5 can be written as:

$$P^{(3)}(t, \Delta t) = \sum_i \sum_v c_{i,v}^*(0)c_{i,v}(0) e^{-\Delta t/T_{1,i,v}} \cdot A_{i,v}(t). \quad (5.6)$$

With this, it is possible to further examine the goal of the experiment which lies in using the CARS probe to selectively interrogate specific vibrational modes of the system. The intrinsic effect within the CARS probe that allows the differentiation between the different vibrational modes is the pronounced enhancement of the CARS signal intensity when the difference in energy between the *pump* and *Stokes* laser (**1** and **2**, Fig. 5.7),  $\Delta\tilde{\nu}$  corresponds to the energy difference between two vibrational levels,  $v = n$  (given by  $|g\rangle$  in Fig. 5.7) and  $v = n + 1$  (given by  $|g'\rangle$  in Fig. 5.7) of a particular normal mode. This resonance of the energy difference between the *pump* and *Stokes* laser,  $\Delta\tilde{\nu}$  to the energy spacing between the vibrational states of a particular normal mode is referred to as a *Raman resonance* of the CARS process to this mode. The interrogation of a specific vibrational state,  $v = n$  that interacts with the *pump* laser **1** can only show a significant signal intensity if the projection into the corresponding *Stokes* mode,  $v = n + 1$  via lasers **1** and **2** is enhanced by the Raman resonance of the CARS process. This projection of the population occupying a vibrational state of a specific normal mode under Raman resonant conditions corresponds to the preparation of a strong population grating of molecules occupying

the respective *Stokes* mode ( $v = n + 1$ ) in the sample cell. This grating is then converted into the optically coherent anti-Stokes signal (**4**, Fig. 5.7) with the second *pump* laser (**3**, Fig. 5.7) by scattering off the grating under Bragg conditions. If the *pump* and *Stokes* lasers, (**1** and **2**) interact with molecules occupying a vibrational state of a mode that is not Raman resonant to the CARS probe, then it will not show a significant contribution to the signal intensity. The lack of a Raman resonance will lead to an ineffective projection of these vibrational states into a virtual state. The scattering of the second *pump* laser pulse **3** from a poorly pronounced grating of virtual states will be ineffective and therefore, the dynamics of these vibrational state will not contribute significantly to the transient CARS intensity **4** as a function of the delay time,  $\Delta t$ .

Of course, this also holds true for vibrationally excited modes as long as the Raman resonance is met and the vibrational states of the mode with  $v = 1, 2, 3 \dots n$  are populated. Since the internal conversion from the  $S_1$  state prepares vibrationally hot modes in the electronic ground state, this will be important to consider. This non-equilibrium thermal distribution following the internal conversion will be interrogated with the same mode-selective mechanism described above. After the internal conversion, the vibrationally hot molecules can interact with the *pump* and *Stokes* laser, **1** and **2** of the CARS process. They are projected into the corresponding Stokes level ( $v = n + 1$ ) and converted to a CARS signal **4** via the second *pump* laser pulse **3**. Under these conditions, the vibrationally hot molecules will contribute significantly to the CARS signal as long as the Raman resonance is preserved. This means that the CARS process tuned to a specific normal mode will interrogate the dynamics in the vibrational ladder of states from  $v = 0$  to  $v = n$  of a specific normal mode up to the vibrational state  $v = n$  where the anharmonicity of the potential causes the energy difference between the vibrational levels to become smaller than the Raman resonance to which the CARS process is tuned to. Under consideration of the broadband nature of the femtosecond laser pulses employed in the experiment, the effect of anharmonicity will not play a critical role.

The importance of the Raman resonance can further be shown with the help of an alternative description of the third-order polarization, commonly found in the literature for the description of a resonant CARS process.<sup>49,56</sup> The advantage of this description is the clear separation of the factors describing the resonance enhancement

of the CARS process. Here, the third order-polarization is described by the amplitude of the laser fields involved in the CARS process and the third-order susceptibility,  $\chi^{(3)}$ :

$$P^{(3)} = E_{pu}^2 E_S \cdot \chi^{(3)}.$$

The description of the third-order susceptibility is shown in Fig. 5.7, where the significance of the different terms of  $\chi^{(3)}$  in the equation below are illustrated.

$$\chi^{(3)} = \frac{\mu_{ge'} \mu_{e'g'} \mu_{g'e} \mu_{eg}}{(\omega_{ge'} - 2\omega_{pu} + \omega_S - i\Gamma_{ge'}) (\omega_{g'g} - \omega_{pu} + \omega_S - i\Gamma_{g'g}) (\omega_{eg} - \omega_{pu} - i\Gamma_{eg})} \cdot \rho_{gg} \quad (5.7)$$

Here,  $\mu_{jk}$  represents the transition dipole moments between the respective molecular states  $|j\rangle$  and  $|k\rangle$ ,  $\Gamma_{jk}$  are the damping constants for the respective transition and  $\rho_{gg}$  is the density matrix of the vibrational states of the electronic ground state. Important to consider are the resonance denominators in equation 5.7, which describe the electronic resonance of the anti-Stokes transition  $\omega_{ge'}$ , the Raman resonance,  $\omega_{g'g}$  and the electronic resonance of the *pump* transition,  $\omega_{eg}$  in relation to the angular frequency of the *pump* and *Stokes* laser,  $\omega_{pu}$  and  $\omega_S$ . All three expressions become small in the resonant case where  $(\omega_{eg} - \omega_{pu} \approx 0)$ ,  $(\omega_{g'g} - \omega_{pu} + \omega_S \approx 0)$  and  $(\omega_{e'g} - 2\omega_{pu} + \omega_S \approx 0)$ . This leads to a high polarizability and furthermore, to a high CARS signal intensity according to the expression of  $\chi^{(3)}$  shown by equation 5.7 and in Fig. 5.7. When this is the case, the damping constants  $\Gamma_{eg}, \Gamma_{g'g}, \Gamma_{e'g}$  in the respective expression for the electronic transition of the *pump* laser ( $e \leftarrow g$ ), the Raman transition ( $g' \leftarrow g$ ) and the anti-Stokes transition ( $e' \leftarrow g$ ) will determine the magnitude with which each resonance influences the signal intensity. It is well established for chromophores in solution that electronic transitions are damped orders of magnitude stronger than Raman transitions.<sup>21,114</sup> This clearly makes the Raman resonance the most critical factor due to a  $\Gamma_{g'g}$  that is orders of magnitudes smaller than  $\Gamma_{eg}$  or  $\Gamma_{e'g}$  for the electronic resonances, in the denominator terms. Therefore, the Raman resonance and not the electronic resonance of the *pump* laser is the most influential when considering the CARS signal intensity from a particular vibrational state in the total signal. As long as the energy difference between excited vibrational state ( $v = n$  and  $v = n + 1$ ) is still resonant to the energy difference of the *pump* and *Stokes* laser, the Raman resonance will primarily determine the signal intensity while the lack of a Raman resonance will lead to a much weaker signal.

With this, the Raman resonance can be seen as an intensity filter for the CARS signal. Since this filter mechanism will hold for ground state vibrational levels ( $v = 0$ ) and vibrationally excited levels ( $v \geq 1$ ), it allows for the monitoring of a superposition of the repopulation dynamics taking place within the ladder of vibrational levels ( $v = 0, 1, 2, 3 \dots n$ ) within a *specific* normal mode,  $i$  as long as the Raman resonance holds. This allows for the amplitude factors in equation 5.6 for modes that are not Raman resonant to the energy difference of *pump* and *Stokes* laser to be approximated to,  $A_{i,v} \approx 0$  in relation to the Raman resonant mode. This further allows equation 5.6 to be simplified to:

$$P^{(3)}(t, \Delta t) = \sum_v^{\infty} c_v^*(0) c_v(0) e^{-\Delta t/2T_{1,v}} \cdot A_v(t). \quad (5.8)$$

Equation 5.8 shows that the third-order polarization is given by the sum over all vibrational states of the one vibrational mode to which the CARS process is tuned to. In order to evaluate how this selectivity shows itself in the CARS signal, the mechanism of detection must be considered. In the experiments presented here, the signal is detected by a quadrature detector in a homodyne scheme, where  $I_{CARS}$  is given by the square of the absolute value of the polarization. In the case of the photoexcitation of  $\beta$ -carotene with the *initial pump* laser, only a small percentage of the total ground state population ( $\leq 1\%$ ) will be excited into the  $S_2$  state. The remaining ground state population will give a constant, stationary CARS signal in the same phase-matched direction as the transient species as they relax into the  $S_0$  state. Due to the population ratio between transient and stationary species, the stationary background will give a much stronger CARS signal than the transient species. Under these conditions, the detection scheme of the transient species corresponds to a heterodyne scheme.<sup>21</sup> Here, the polarization from the transient species  $P_{trans}^{(3)}(t, \Delta t)$  is mixed with the strong polarization of the stationary species  $P_{const}^{(3)}(t)$  on the quadrature detector according to:

$$\begin{aligned} I_{CARS}(\Delta t) &= \int_{t=\Delta t}^{\infty} \left| P_{trans}^{(3)}(t, \Delta t) + P_{const}^{(3)}(t) \right|^2 dt. \\ &= \int_t^{\infty} \left| P_{const}^{(3)}(t) \right|^2 + \left| P_{trans}^{(3)}(t, \Delta t) \right|^2 + 2 \left| P_{const}^{*(3)}(t) \cdot P_{trans}^{(3)}(t, \Delta t) \right| \end{aligned} \quad (5.9)$$

Here the mixed term (last term in the equation 5.9) clearly represents the strongest

polarization that is a function of the delay time,  $\Delta t$ .<sup>21</sup> This is due to the population ratio of the species from which the respective signals are generated. With this equation 5.9 can be simplified to:

$$I_{CARS}(\Delta t) = \int_{t=\Delta t}^{\infty} 2 \left| P_{const}^{*(3)}(t) \cdot P_{trans}^{(3)}(t, \Delta t) \right| dt. \quad (5.10)$$

Using equation 5.8 for the polarization from the transient species,  $P_{trans}^{(3)}(t, \Delta t)$  in equation 5.10 and carrying out the integration over time, the CARS intensity as a function of the delay time can be written as:

$$I_{CARS}(\Delta t) = \sum_v^{\infty} c_v^*(0) c_v(0) e^{-\Delta t/T_{1,v}} \cdot A'_v. \quad (5.11)$$

Here,  $A'_v$  unifies the contribution from  $A_v(t)$  and the polarization from the stationary species  $P_{const}^{(3)}(t)$  in the integration over time. A comparison of the fit function in equation 5.1 with equation 5.11 shows that the mono-exponential time constant, extracted with the fit of the experimental data, characterizes the superposition of the dynamics taking place within the ladder of vibrational states of a specific normal mode to which the CARS process is tuned. The population flow in the ladder of vibrational states of a specific normal mode will show the dynamics of internal conversion, IVR and cooling, taking place within the ladder of vibrational states of the mode that the CARS process is tuned to, so that the time constant,  $\tau$  can be related to these dynamic phenomena in the following way:

$$\frac{1}{\tau} = \frac{1}{\tau_{S1/S0} + \tau_{IVR} + \tau_{cooling}}. \quad (5.12)$$

Which of the time constants,  $\tau_{S1/S0}$ ,  $\tau_{IVR}$ , and  $\tau_{cooling}$  contribute significantly to the population recovery of the different normal modes given by time constant extracted from the fits,  $\tau$  will be discussed in the following section.

With equation 5.12, the repopulation of the vibrational states in a specific normal mode is solely attributed to non-radiative processes. The repopulation of the electronic ground state through fluorescence can be ruled out since the  $S_1 \leftarrow S_0$  optical transition is symmetry forbidden for one photon transition. In order to further rule out contributions from  $S_1$  state vibrational modes that enter the signal due to  $S_n \leftarrow S_1$  optical transition, the CARS process was also resolved in time according to the experimental scheme shown in Fig. 5.5. The electronic states interrogated by the



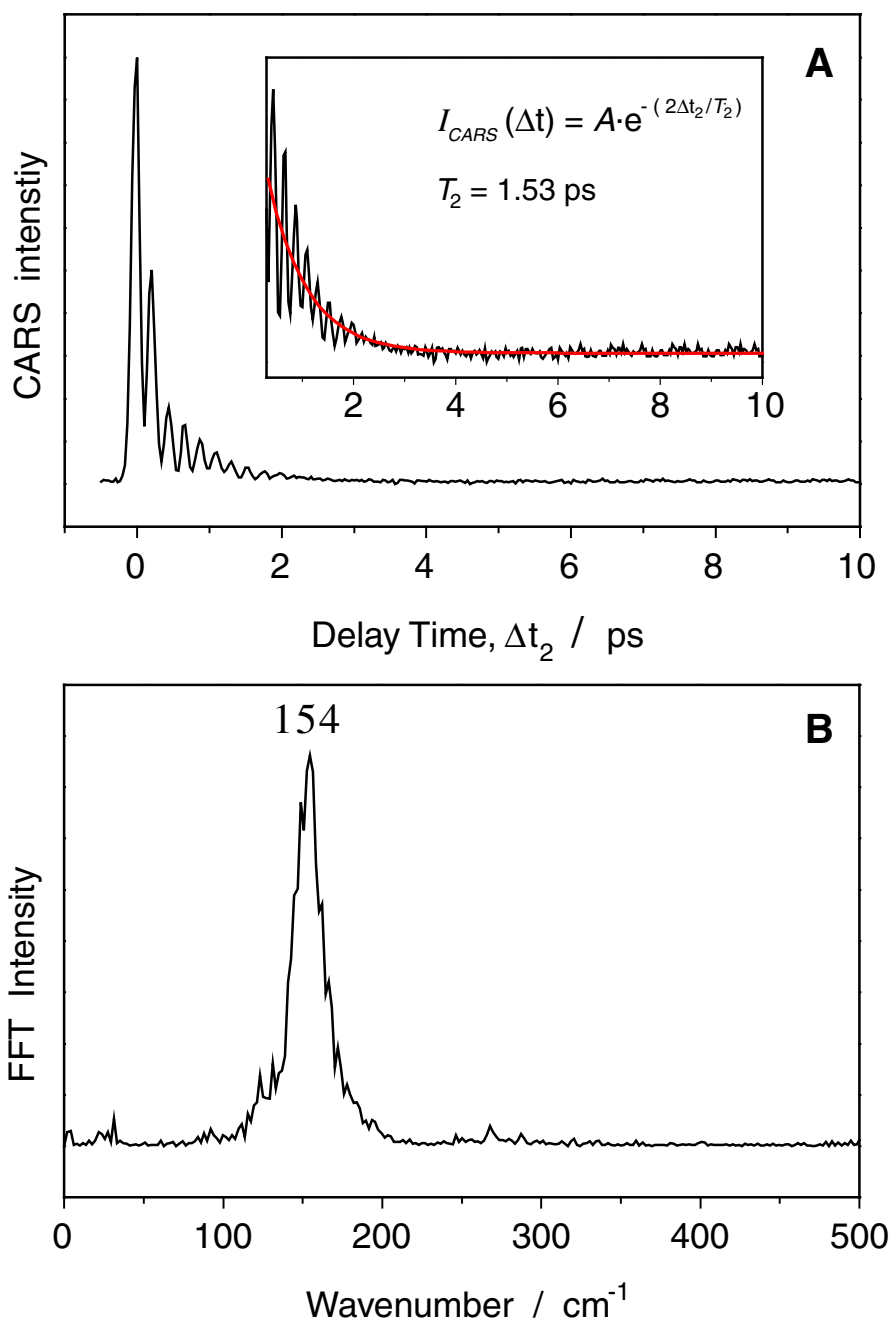


Figure 5.8: **A.** Transient CARS signal detected at  $1005 \text{ cm}^{-1}$  as a function of the delay time,  $\Delta t_2$ , as shown in the experimental scheme in Fig. 5.5 with  $\Delta t_1 = 1$  ps. The inset shows a fit to the experimental data for determining the damping of the signal due to dephasing of the Raman modes described by the time constant  $T_2$ . **B.** FFT spectrum of the transient CARS signal in **A** after the subtraction of the exponential dephasing component. For details see text.

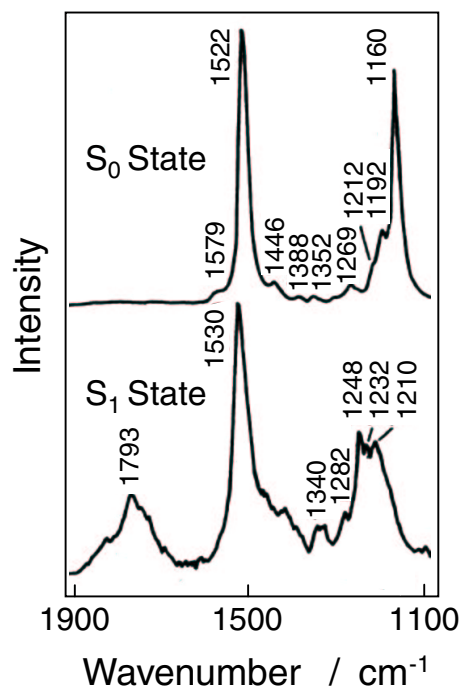


Figure 5.9: Resonance Raman spectrum of the  $S_1$  and  $S_0$  state in  $\beta$ -carotene measured by Hashimoto and Koyama utilizing the  $S_n \leftarrow S_1$  and  $S_2 \leftarrow S_0$  optical transitions, respectively.<sup>98</sup> A comparison of the Raman bands in the  $S_1$  and  $S_0$  state gives insight into the role of the different vibrational modes in the  $S_1/S_0$  internal conversion. The Raman band at  $1793\text{ cm}^{-1}$  in the  $S_1$  state, which is attributed to the C=C symmetric stretch mode in the polyene backbone of  $\beta$ -carotene, is particularly interesting. This band shows the largest FWHM of all Raman bands in the  $S_1$  state and displays a significant shift to higher wavenumbers in comparison to the position of the band for this mode in the  $S_0$  state at  $1530\text{ cm}^{-1}$ .

CARS probe can be monitored by determining the Raman modes that contribute to the signal. The  $S_0$  and  $S_1$  states possess characteristic Raman shifts that vary significantly between the respective electronic state and the relative Raman shifts, that can be seen in the Fourier transformation of the time-resolved CARS process, will show the signature of the electronic states interrogated by the CARS probe for  $\Delta t_1 = 1\text{ ps}$  and a variable delay time,  $\Delta t_2$ . Furthermore the energy difference between *pump* and *Stokes* lasers tuned to  $\Delta\tilde{\nu} = 1100\text{ cm}^{-1}$  allows for a coherent superposition of the Raman modes between approximately  $1275$  and  $975\text{ cm}^{-1}$  (see  $S_0$  and  $S_1$  resonance Raman spectra in Fig. 5.9), assuming a spectral FWHM of  $250\text{ cm}^{-1}$  in the spectral convolution of *pump* and *Stokes* laser. The transient CARS signal, shown in panel A of Fig. 5.8, detected at  $1005\text{ cm}^{-1}$  as a function of  $\Delta t_2$  shows a strong non-resonant signal centered at  $\Delta t_2 = 0$ .<sup>115</sup> For  $\Delta t_2 > 0$  the dephasing of the coherent Raman modes can be seen in the decay of the resonant signal, as described in section 2.1.1. This decay can be characterized with a total dephasing time,  $T_2 = 1.53\text{ ps}$  as shown in the inset of panel A in Fig. 5.8. The transient signal further shows oscillations with a period of approximately  $215\text{ fs}$  that correspond to the beating of the optically coherent signals from different Raman modes that are mixed on the quadrature detector. This macroscopic effect is described extensively in the literature, where it is

shown that the Fourier transformation gives the energy spacing between the Raman modes contributing to the beating signal.<sup>23,30,112</sup> After the subtraction of the component attributed to the dephasing according to the equation given in panel A, the transient signal is Fourier transformed which is shown in panel B of Fig. 5.8. The Fourier transformation reveals an energy spacing of  $154\text{ cm}^{-1}$  which corresponds well to the difference between the Raman shift of  $1004$  and  $1157\text{ cm}^{-1}$  in the electronic ground state. Important to note, is the shift of the  $1157\text{ cm}^{-1}$  Raman mode in the  $S_1$  state to approximately  $1230\text{ cm}^{-1}$  as shown in Fig. 5.9. The larger difference of  $225\text{ cm}^{-1}$  between this shifted  $S_1$  Raman mode and the band at  $1006\text{ cm}^{-1}$  cannot be observed in the Fourier transformation of the transient CARS signal. This shows that the CARS signal exclusively gives the spectral signature of the  $S_0$  and not the  $S_1$  state. With this, the observed dynamics with the CARS process as the probe mechanism in the experimental scheme shown in Fig. 5.2 only show the dynamics of the electronic ground state. Contributions from Raman modes in the excited  $S_1$  state can be ruled out.

### 5.2.3 Discussion: Nuclear Motion Involved in the $S_1/S_0$ Internal Conversion of $\beta$ -Carotene

In the previous section, it was established that the CARS probe is mode-selective with respect to the interrogation of the dynamics taking place in the different vibrational modes of the electronic ground state of  $\beta$ -carotene subsequent to the  $S_1/S_0$  internal conversion. In the following, a mechanism with which these modes are populated subsequent to the  $S_1/S_0$  internal conversion is postulated. This is done by interpreting the varying recovery times for the different normal modes shown in Fig. 5.10 and summarized in Table 5.1, with the help of theoretical models of internal conversion and previous experimental work reported in the literature. The interpretation of the recovery times will then be used to formulate a model for the  $S_1/S_0$  internal conversion, giving a picture of the nuclear motion involved in this electronic transition.

As established in the previous section, the values for  $\tau$  show that the population flow from the  $S_1$  state into the electronic ground state is not uniform for the normal modes that were interrogated. The recovery time of  $\tau = 8.46\text{ ps}$  for the normal mode at  $1524\text{ cm}^{-1}$ , which is dominated by a large amplitude motion along the C=C

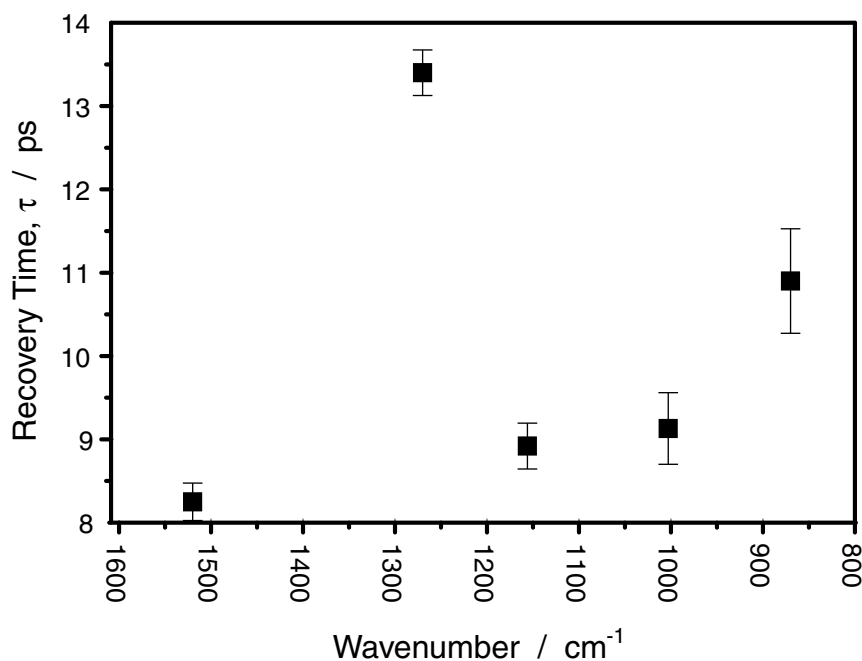


Figure 5.10: Wavenumber position of the vibrational modes probed with the CARS process as a function of the recovery time,  $\tau$  of the population in the electronic ground state subsequent to the  $S_1/S_0$  internal conversion.

symmetric stretch in the polyene backbone of  $\beta$ -carotene, is clearly the fastest recovery time listed in Table 5.1. From this, it can be postulated that the fastest time constant of population recovery in the electronic ground state for this vibrational mode is direct experimental evidence that this mode acts as the primary accepting mode for population flow in the  $S_1/S_0$  internal conversion. The fast recovery time for this mode in comparison to the recovery times measured for all other vibrational modes listed in Table 5.1, shows that the population flow between the  $S_1$  and  $S_0$  potential energy surface is primarily funneled through this form of nuclear motion. This interpretation is discussed below in the framework of the commonly accepted theoretical models of internal conversion with the help of theoretical and experimental work found in the literature such as (i) theoretical calculations of model polyenes, (ii) transient infrared absorption of the  $S_1$  state, (iii) line width analysis and Raman shift of this normal mode in  $S_1$  state Raman spectrum of  $\beta$ -carotene, (iv) isotope effects on the  $S_1/S_0$  internal conversion and, (v) comparisons to mode-averaged time constants for the depopulation of the  $S_1$  state, all of which support this picture.

Table 5.1: Summary of the results obtained from a *pump*-CARS experiment for the investigation of the population recovery into the different vibrational modes of the electronic ground state in  $\beta$ -carotene subsequent to the  $S_1/S_0$  internal conversion. List below are the wavenumber positions, recovery times and characteristic motion of the vibrational modes probed in the experiment.

Wavenumber / $\text{cm}^{-1}$	Recovery Time, $\tau$ / ps	Characteristic Motion <sup>66,120</sup>
1524	$8.46 \pm 0.23$	C=C symmetric stretch
1269	$13.40 \pm 0.27$	C-H in plane bending
1157	$8.92 \pm 0.27$	C-C symmetric stretch
1004	$9.13 \pm 0.43$	Methyl to chain stretch
872	$10.90 \pm 0.63$	C=C-C bending

Theoretical calculations of model polyenes have shown that the equilibrium bond length of the C=C symmetric stretch mode shows a large displacement to a shorter equilibrium bond length in the  $S_0$  state when compared to the equilibrium bond length in the  $S_1$  state.<sup>116–119</sup> This is further supported by transient  $S_1$  state IR-absorption experiments which confirm that the equilibrium bond length of this mode shows a significantly larger nuclear displacement between the  $S_1$  and  $S_0$  state, in comparison to all other modes investigated in the  $S_1$  state.<sup>108</sup> Assuming a tunneling mechanism for the  $S_1/S_0$  internal conversion as described by the formalism of Engelman-Jortner in section 2.3.2, it will be vibrational modes showing a large nuclear displacement of the equilibrium bond lengths in the two electronic states involved in the internal conversion that are particularly suited as accepting modes for population transfer into the lower lying electronic state.<sup>4,66</sup> This is due to the large Franck-Condon factors between the vibrational states of the respective electronic states. The quadratic influence of Franck-Condon factors,  $|\langle\varphi_{nv}|\varphi_{mu}\rangle|$  can be seen in the expression of the rate of internal conversion in the formalism of Engelman and Jortner, as given in equations 2.56 and 2.57 on page 39.

The classification of the C=C symmetric stretch mode at  $1534 \text{ cm}^{-1}$  as the nuclear motion that facilitates the electronic transition between the  $S_1$  and  $S_0$  state, based on the fastest recovery of repopulation with  $\tau = 8.46 \text{ ps}$ , is further substantiated by the  $S_1$  Raman spectrum of  $\beta$ -carotene, recorded by Hashimoto and Koyama, which is explicitly shown in Fig. 5.9 along with the  $S_0$  Raman spectrum.<sup>66,98</sup> The Raman

spectrum shows a band at approximately  $1790\text{ cm}^{-1}$ , assigned to the C=C symmetric stretch mode, which is shifted to a much lower wavenumber position of  $1530\text{ cm}^{-1}$  in the electronic ground state Raman spectrum. Two important characteristics of this  $1790\text{ cm}^{-1}$  band should be noted with regard to the role of this mode in the  $S_1/S_0$  internal conversion. First of all, the strong shift of this mode to a higher wavenumber position in the  $S_1$  state is attributed to the coupling of the  $S_1$  and  $S_0$  state via this vibrational mode. The pronounced blue shift of this mode in the  $S_1$  state shows that the coupling constant,  $C$  described in equation 2.57 on page 39 is large for the C=C symmetric stretch mode. This guarantees a high rate of population flow between the  $S_1$  and  $S_0$  state for this mode due to the quadratic proportionality of  $C$  to the rate constant,  $k_{IC}$ . Additionally, for the two-state/two-mode model, which would assume a surface hopping mechanism via a conical intersection, it is a coupling mode that is specifically designated as an accepting mode for population transfer in the lower lying electronic state.<sup>9,68,121</sup> This would hold true for the C=C symmetric stretch mode, which possesses the necessary  $a_g$  symmetry for coupling the relevant  $S_1$  ( $1A_g^-$ ) and  $S_0$  ( $2A_g^-$ ) states. The second important attribute of the Raman band at  $1790\text{ cm}^{-1}$  is the pronounced FWHM of this band, which is clearly larger than any other band in the Raman spectrum of the  $S_1$  state. The large FWHM is interpreted in terms of a lifetime broadening ( $T_1$  broadening). This supports the shortest lifetime of this mode in the  $S_1$  state and accordingly the fastest population flow into the  $S_0$  state through this mode. In summary, assigning the C=C symmetric stretch mode as the primary accepting mode for population flow during the  $S_1/S_0$  internal conversion on the basis of the fastest repopulation of  $\tau = 8.46\text{ ps}$ , measured with the mode-selective CARS probe at  $1524\text{ cm}^{-1}$ , is in agreement with a variety of theoretical and experimental data in the literature and is conform with the theoretical models for non-adiabatic transitions between electronic state as presented above. With respect to equation 5.12, the fastest repopulation of the vibrational states of this mode is primarily determined by the flow of population out of the  $S_1$  state, given by  $\tau_{S_1/S_0}$ , versus other mechanisms of repopulation of the  $S_0$  state such as internal vibrational energy redistribution (IVR) or vibrational cooling given by  $\tau_{IVR}$  and  $\tau_{cooling}$ .

The slower population recovery for the other vibrational modes listed in Table 5.1 in relation to the fastest recovery time of the C=C symmetric stretch mode can also be put in the framework of experimental data found in the literature, allowing for a

better interpretation of the slower recovery times. Here, isotope effects on the  $S_1/S_0$  internal conversion give valuable information when compared to the direct, mode-selective measurement of the population recovery in the vibrational modes of the  $S_0$  state. The isotope effect on the  $S_1/S_0$  internal conversion was determined by Nagae *et.al.* by measuring the mode-averaged rate of depopulation of the  $S_1$  state through transient  $S_n \leftarrow S_1$  absorption.<sup>66</sup> For natural  $\beta$ -carotene, a mode-averaged time constant of  $\tau_{IC}(\text{natural}) = 9.92$  ps was determined for the  $S_1/S_0$  internal conversion. The deuteration of  $\beta$ -carotene only displayed a small effect on the time constant of internal conversion ( $\tau_{IC}(\text{D}) = 10.73$  ps), while  $^{13}\text{C}$  substitution in  $\beta$ -carotene shows a much slower time constant of ( $\tau_{IC}(^{13}\text{C}) = 14.27$  ps) than  $\beta$ -carotene with the natural  $^{13}\text{C}/^{12}\text{C}$  ratio. The smaller effect on the  $S_1/S_0$  internal conversion for the deuterated species in comparison to the  $^{13}\text{C}$  substitution is particularly interesting since the exchange in mass is greater for the deuteration, where 56 hydrogen atoms are replaced while the  $^{13}\text{C}$  substitution only exchanges  $\leq 40$  carbon atoms in  $\beta$ -carotene.

These results can be correlated with the mode-selective rates of repopulation in the electronic ground state by classifying the nuclear motion into normal modes that play a rate-determining role in the  $S_1/S_0$  internal conversion and normal modes that do not significantly participate in the population flow between the  $S_1$  and  $S_0$  state. The small deuteration effect shows that normal modes with large amplitude motion of carbon/hydrogen bonds and large skeletal motion, where hydrogen atoms are strongly involved, are extremely unlikely candidates for significant population transfer between the two potential energy surfaces involved in the  $S_1/S_0$  internal conversion. This correlates well with the mode-selective interrogation of the repopulation of the electronic ground state with the CARS probe. The slowest recovery time of  $\tau = 13.40$  ps was measured for the normal mode at  $1269\text{ cm}^{-1}$  with a large amplitude motion along the C-H in plane bending coordinate and the second slowest recovery time of  $\tau = 10.90$  ps is seen for the C=C-C bending mode at  $872\text{ cm}^{-1}$ , which involves large skeletal motion and a significant participation of hydrogen atoms.

On the other hand, the much slower internal conversion time in the case of  $^{13}\text{C}$  substitution shows that normal modes with large amplitude motion of carbon/carbon bonds, such as stretching motion along the polyene backbone, are good candidates for funneling the population into the electronic ground state via the  $S_1/S_0$  internal conversion. This is also in good correlation with the time constants,  $\tau$  determined

for the normal modes with large amplitude motion along the C-C and C=C bond symmetric stretch at  $1157\text{ cm}^{-1}$  and  $1525\text{ cm}^{-1}$ , respectively (see Table 5.1). These two vibrational modes show the two fastest recovery times of  $\tau = 8.46\text{ ps}$  and  $8.92\text{ ps}$  respectively. Over all, the tendency in the recovery times shows excellent agreement with the respective isotope effects which are a direct reflection of the type of vibrational mode decisive for the rate of population flow between the two potential energy surfaces.

The characterization of the isotope effects on the  $S_1/S_0$  internal conversion were carried out using a probe mechanisms that is not mode-selective, which leads to the observation of dynamics that are a weighted superposition of the dynamics in all normal modes. Important to further note from these experiments is the time constant for the mode-averaged depopulation of the  $S_1$  state for the natural species in *n*-hexane of  $\tau_{IC}(\text{natural}) = 9.92\text{ ps}$ .<sup>66</sup> In comparison, the recovery time of repopulation of the  $S_0$  state, measured for the C=C symmetric stretch, is significantly faster with  $\tau = 8.46\text{ ps}$ . This is important to note since the recovery of population in the vibrational states in the  $S_0$  cannot be faster than the depopulation of the  $S_1$ . The observation of a recovery rate for the C=C symmetric stretch mode that is faster than the mode-averaged time constant for depopulation of the  $S_1$  allows for the deduction that the time constant for the C=C symmetric stretch mode is determined by fast population flow between the participating electronic states rather than subsequent cooling processes in the  $S_0$  state. Additional cooling processes for this mode could only lead to recovery times that are slower than the time scale measured for the depopulation of the  $S_1$  state monitored by mode-averaged probes. For the vibrational modes with slower recovery times of  $\tau = 9.13$  to  $13.40\text{ ps}$ , the rate of internal vibrational energy redistribution among the vibrational modes in the electronic ground state and the cooling process will be important to consider when evaluating the measured time constants in terms of a mechanism with which the respective vibrational modes are repopulated.

The comparison above, between the mode-selective time constants for the recovery of the population in the electronic ground state modes, determined by means of the CARS probe, and the experimental data found in the literature allows for the postulation of a precise mechanism for the  $S_1/S_0$  internal conversion with respect to the role of the individual normal modes in this radiationless transition. This mech-



anism will be discussed with the help of the schematic potential energy diagram in Fig. 5.11, which shows the potentials for the C=C symmetric stretch and the C-H in plane bending mode. These two vibrational modes are chosen for the representation since they show the clearest difference in recovery times,  $\tau$ . It was clearly established above, that the fastest recovery time of the C=C symmetric stretch mode is determined by the funneling of population between the  $S_1$  and  $S_0$  states through this mode. With this, the C=C symmetric stretch mode can be classified as the accepting mode for population in the  $S_0$  state. For the repopulation of the other vibrational modes, two possible mechanisms can be formulated in the framework of the recovery times measured. Here the C-H in plane bending mode will be representative of the vibrational modes showing the slower recovery times between  $\tau = 9.13$  to 13.40 ps. The mechanism with which the C-H in plane bending mode is populated is assumed to be analog for all other modes possessing slower recovery times of  $\tau = 9.13$  to 13.40 ps. In the 2-state/2-mode model of internal conversion, the population flow is funneled into a coupling mode, in this case the C=C symmetric stretch mode and then spreads out over the normal modes of the energetically lower lying potential energy surface via internal vibrational energy redistribution and cooling.<sup>8,9,68,121</sup> If this model is applied to the  $S_1/S_0$  internal conversion in  $\beta$ -carotene, then the slower recovery times measured for the normal modes in Table 5.1 with  $\tau = 9.13$  to 13.40 ps will be determined by (i) the time scale with which the vibrational modes of the C=C symmetric stretch mode are populated by means of population transfer from the  $S_1$  state and subsequent cooling within the C=C symmetric stretch mode and, (ii) the following internal vibrational energy redistribution out of the vibrational states of the C=C symmetric stretch into the vibrational states of other modes with subsequent cooling in these modes. This mechanism is described in Fig. 5.11 by following pathway **A** to **B** when considering the population of the C-H in plane bending mode.

In the framework of the Jortner-Engelman model, it cannot be ruled out that the slower recovery times of  $\tau = 9.13$  to 13.40 ps for the other vibrational modes correlate to a slower repopulation of these modes directly out of the  $S_1$  state, rather than internal vibrational energy redistribution from the C=C symmetric stretch mode of the electronic ground state.<sup>4,66</sup> For this mechanism of repopulation, the modes showing slower recovery times are populated directly out of the  $S_1$  state on a slower time scale due to poor Franck-Condon Factors and weak coupling constants between

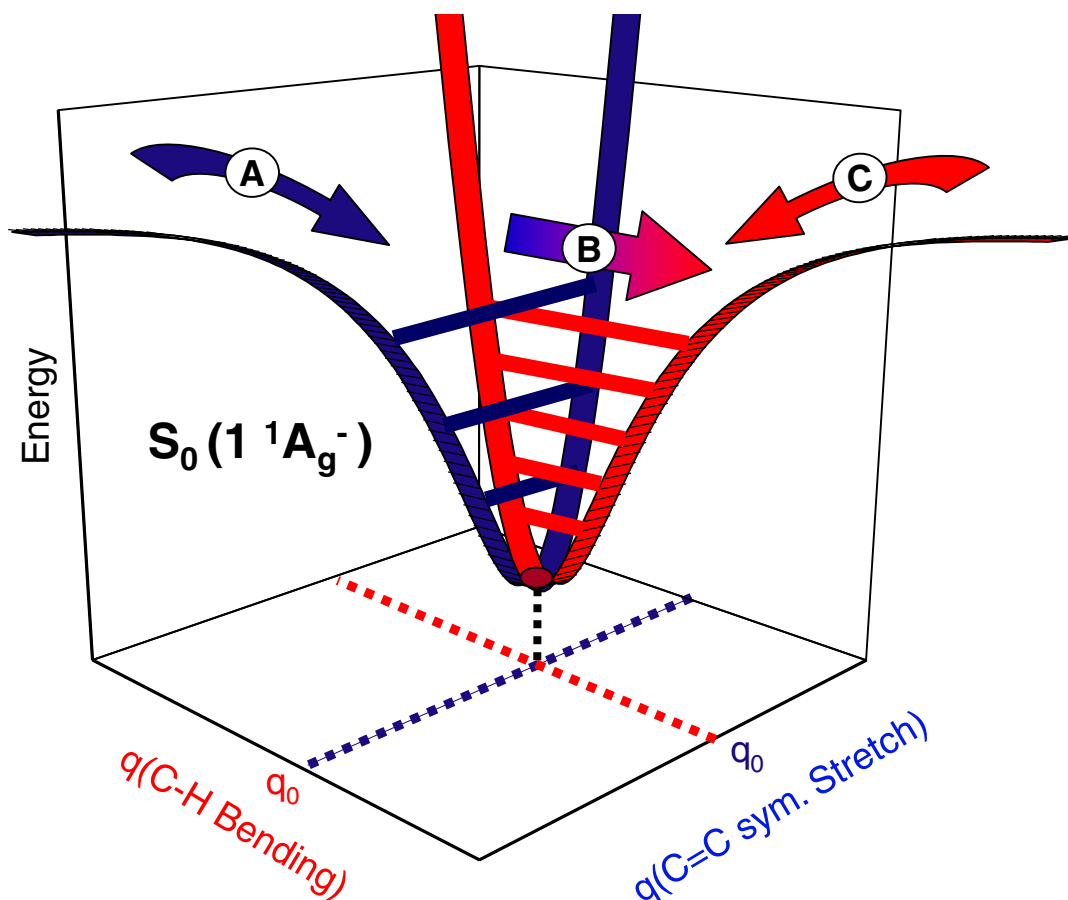


Figure 5.11: Schematic model for the repopulation of the electronic ground state subsequent to the  $S_1/S_0$  internal conversion. The model is postulated based on the measured time constants of repopulation,  $\tau$  of the individual vibrational modes in the electronic ground state listed in Table 5.1. Pathway **A** shows the primary flow of population in the C=C symmetric stretch mode ( $\tau = 8.46$  ps) which acts as the dominant accepting mode. The repopulation of other vibrational modes in the electronic ground state can take place over pathway **B** or **C**. Representative of all modes showing slower recovery times, pathway **B** shows the repopulation of the C-H bending mode ( $\tau = 13.40$  ps) via IVR processes out of the C=C symmetric stretch which makes the slower recovery times the composite time of population flow into the C=C symmetric stretch mode and IVR/cooling processes together. The alternative pathway **C** shows a direct population flow from the  $S_1$  state into vibrational modes with slower recovery times which are in this case the result of poor Franck-Condon factors and small coupling constants for these modes. For details see text.

the  $S_1$  and  $S_0$  state. These factors strongly determine the rate for an electronic transition as described in equations 2.56 and 2.57 on page 39. This mechanism is illustrated in Fig. 5.11 by following pathway **C**, which takes place parallel to pathway **A**.

The measured recovery times for the repopulation of the different vibrational modes do not give evidence that would allow for either of the two mechanisms with which the electronic ground state is fully repopulated to be preferred. The difficulty in differentiating between the two possible mechanisms is most evident when the repopulation of the C-C symmetric stretch mode is evaluated. This vibrational mode shows the second fastest recovery time of  $\tau = 8.92$  ps in the  $S_0$  state during the  $S_1/S_0$  internal conversion. This population recovery lies very close to the fastest recovery of the C=C symmetric stretch mode. The isotope effects on the  $S_1/S_0$  internal conversion presented above cannot rule out that the C-C symmetric stretch mode plays a significant role in population transfer between the  $S_1$  and  $S_0$  state since this mode does not incorporate large amplitude motion of hydrogen atoms. The fast recovery time of  $\tau = 8.92$  ps would further support significant population transfer through this mode. This would make the direct repopulation out of the  $S_1$  state through the C-C symmetric stretch according to pathway **C** in Fig. 5.11 plausible. On the other hand, the resonance Raman band of the C-C symmetric stretch mode in the  $S_1$  state does not show a significantly broad FWHM in comparison to the other  $S_1$  state Raman bands (see Fig. 5.9).<sup>66,98</sup> Therefore, pathway **B** via **A** in Fig. 5.11 is a likely mechanism of repopulation for the C-C symmetric stretch mode and the fast repopulation of this mode would be the result of strong coupling between the C=C and C-C symmetric stretch mode in the electronic ground state. This shows the difficulty in differentiating between the two possible mechanisms of repopulation for primarily the C-C symmetric stretch mode and more generally for all other modes showing recovery times between  $\tau = 9.13$  to 13.40 ps in Table 5.1. As a further possibility, both mechanisms could be active in the repopulation of the vibrational modes of the  $S_0$  state and each contributes according to the rates involved with each channel. A greater insight into the mechanism of repopulation of the vibrational modes with slower recovery times could be gained through precise theoretical calculation of the  $S_1$  and  $S_0$  potential energy surfaces.

Despite the ambiguity between the two possible mechanisms for modes showing

the slower recovery times in Table 5.1, the fastest recovery time of  $\tau = 8.46$  ps for the C=C symmetric stretch mode allows for an insight into the nuclear motion involved in the  $S_1/S_0$  internal conversion of  $\beta$ -carotene. It was shown above, that the C=C symmetric stretch is the vibrational mode that determines the time scale for the population transfer between the  $S_1$  and  $S_0$  state and with this it can clearly be labelled as the accepting mode for this radiationless transition. Through the comparison of the dynamics of repopulation of this mode to the other modes listed in Table 5.1, the reaction coordinate for the  $S_1/S_0$  internal conversion can be identified to take place primarily along the coordinate of the C=C symmetric stretch mode.

With the results and discussion presented above, it has been shown that the CARS process used as a probe mechanism in a time resolved *pump*-CARS scheme is a powerful tool in time-resolved spectroscopy for determining the population flow in specific normal modes of a molecular system. With the *pump*-CARS scheme, it is possible to directly determine the nuclear motion involved in ultrafast, non-adiabatic dynamics such as the  $S_1/S_0$  internal conversion in  $\beta$ -carotene. This allows for a better understanding of the mechanism of this electronic transitions with respect to the role of specific normal modes. In the case of  $\beta$ -carotene, the identification of the reaction coordinate of the  $S_1/S_0$  internal conversion allows for speculation about the influence of *in-vivo* environments, such as the protein environment of photosystem II and how these environments facilitate or hinder the  $S_1/S_0$  internal conversion in order to allow  $\beta$ -carotene to fulfill its biophysical roles as an auxiliary light harvesting pigment, energy dissipater and triplet quencher in photosynthesis. For further work, the CARS process shows the potential to act as a powerful tool for determining the reaction coordinate and with this, the precise mechanism of photochemical reactions and electron transfer in which the change in electronic distribution is substantial, leading to large amplitude motion along a specific coordinate and ultimately to the dissociation and formation of chemical bonds.

### 5.3 The Behavior of Vibrationally Hot Modes during Internal Conversion

While the experiment described in the previous section aimed at determining the type of nuclear motion involved in the  $S_1/S_0$  internal conversion of  $\beta$ -carotene,

the experiment described in the following will focus on the energetics of vibrational states participating in the  $S_1/S_0$  internal conversion. For this, time-resolved population gratings as described in section 2.2.3 will be applied for the interrogation of the population dynamics in the  $S_1$  dark state of  $\beta$ -carotene. The use of transient gratings in the exploration of non-adiabatic dynamics will be presented and furthermore, an experimental strategy within the transient grating scheme will be pursued, that allows for the probing of different vibrational quantum states in this electronic potential.<sup>62</sup> The experiment aims to characterize the time scale of internal conversion for vibrational hot modes and to compare these to the time scale of vibrational ground state modes. In addition to this, the competition between vibrational cooling and internal conversion as decay channels for vibrationally hot states in excited electronic potentials will be explored with this spectroscopic method.

### 5.3.1 Methodology of Population Gratings in $\beta$ -Carotene

The theoretical description of transient gratings was presented in section 2.2.3 and the precise experimental details concerning the practical realization of this method were given in chapter 3. Figure 5.12 shows the experimental scheme of a transient grating experiment applied to the investigation of the dynamics taking place in the  $S_1$  state of  $\beta$ -carotene. Here, a 0.1 mM solutions of  $\beta$ -carotene in acetone were prepared in a rotating sample cell (100 Hz) with a cell length of 0.5 mm. Gratings were induced in the sample space by focusing two non-collinear *pump* lasers pulses (**1** and **2** in Fig. 5.12,  $\lambda_{pu} = 510$  nm, FWHM = 70 fs, 60 nJ) into the sample, which are resonant with the  $S_2 \leftarrow S_0$  optical transition in  $\beta$ -carotene. The two *pump* pulses interact simultaneously with the sample while a third, *probe* pulse (**3** in Fig. 5.12,  $\lambda_{probe} = 570$  to 635 nm, FWHM = 70 fs, 50 nJ) with a variable time delay,  $\Delta t$ , interrogates the dynamics initiated by the two *pump* lasers. This is accomplished by an elastic scattering of the *probe* pulse under Bragg conditions off the grating. The signal (**4** in Fig. 5.12), scattered in the phase matched direction,  $\mathbf{k}_{TG} = \mathbf{k}_{pu} - \mathbf{k}_{pu} + \mathbf{k}_{probe}$  (section 3.2) is coupled into a monochromator and the spectral components are detected with a broadband CCD detector (section 3.3). The intensity of the signal is recorded as a function of the delay time,  $\Delta t$  between the two *pump* pulses and the *probe* pulse. By tuning the *probe* laser resonant to the  $S_n \leftarrow S_1$  absorption, it is possible to observe the population flow into the  $S_1$  state through the  $S_2/S_1$  internal conversion from the

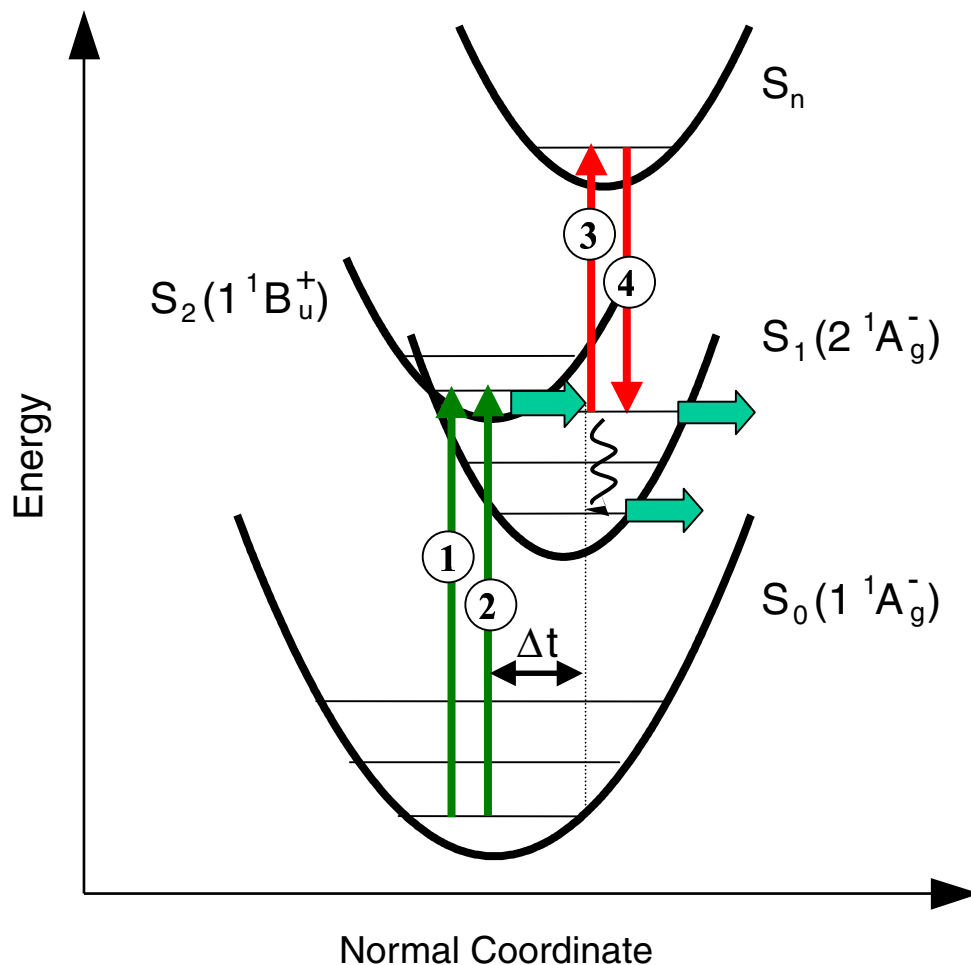


Figure 5.12: Two *pump* lasers (**1** and **2**,  $\lambda_{pu} = 510$  nm, FWHM = 70 fs, 60 nJ), induce a population grating of electronically excited molecules in the  $S_2$  state of  $\beta$ -carotene. The subsequent  $S_2/S_1$  internal conversion populates the  $S_1$  state which is probed by elastically scattering a third *probe* pulse (**3**,  $\lambda_{pu} = 570 - 660$  nm, FWHM = 70 fs, 60 nJ) of the population grating generating the coherent signal **4** in the phase-matched direction. The *probe* pulse is delayed variably in time ( $\Delta t$ ) relative to the two laser *pump* pulses that interact simultaneously with the sample in order to induce the population grating. The *probe* pulse is tuned variably to be in resonance to the  $S_n \leftarrow S_1$  optical transition and furthermore spectrally red-shifted out of this optical transition to enhance the interrogation of vibrationally excited states in the  $S_1$  potential.

originally prepared  $S_2$  state, and the depopulation of the  $S_1$  state by means of the  $S_1/S_0$  internal conversion. In order to monitor the population in different regions of the  $S_1$  potential, the broadband signal was spectrally resolved and monitored at different spectral positions of the signal. Furthermore, the central wavelength of *probe* pulse was varied to include spectral positions that lie red-shifted to the  $S_1$  absorption in order to bring the *probe* laser in resonance with vibrationally hot states in the  $S_1$  potential. Here, the energy of the hot vibrational states compensate for the lack of energy in the *probe* pulse necessary for the  $S_n \leftarrow S_1$  transition from the vibrational ground state in the  $S_1$  state.<sup>62</sup>

### 5.3.2 Experimental Results: Probing Vibrationally Hot Modes in Electronic Dark States

In Fig. 5.13, the signal intensity of the scattered *probe* pulse is plotted as a function of the spectral position in the signal and the delay time,  $\Delta t$  between the two *pump* lasers that form the grating and the *probe* laser scattered off this grating. Since the *probe* laser is scattered elastically, a given spectral position in the signal corresponds to the spectral component of the *probe* laser that interrogates the dynamics of the grating.<sup>34,53,54,62</sup> For an overview, the dynamics taking place at the four different spectral positions of the signal obtained by varying the *probe* pulse from  $\lambda_{probe} = 570$  nm to 635 nm ( $\tilde{\nu}_{probe} = 15950$  cm<sup>-1</sup> to 16950 cm<sup>-1</sup>) are shown in panels A-D in Fig. 5.14. The experimental data points, displayed as open circles, show the dynamics observed at the maximum signal intensity for the four different central wavelength of the *probe* pulse, which are noted in the upper right hand corner of the respective panel of Fig. 5.14. The dynamics were further analyzed at the blue and red side of the FWHM in the spectral profile of the signal. This is shown in Fig. 5.13 for the measurement performed with the *probe* laser centered at 590 nm (16950 cm<sup>-1</sup>). The measurements carried out with other spectral positions of the *probe* laser were evaluated in the same manor.

From a first qualitative comparison of the measurements in Fig. 5.14, it can be seen that the transient signal shows a dependency on the spectral position at which the signal is observed. The first evident feature in panels A-D, that shows a variation in the transient signal for the different spectral positions of detection, is an intense peak centered around  $\Delta t = 0$  ps that is observed for a detection at 15950 cm<sup>-1</sup> in

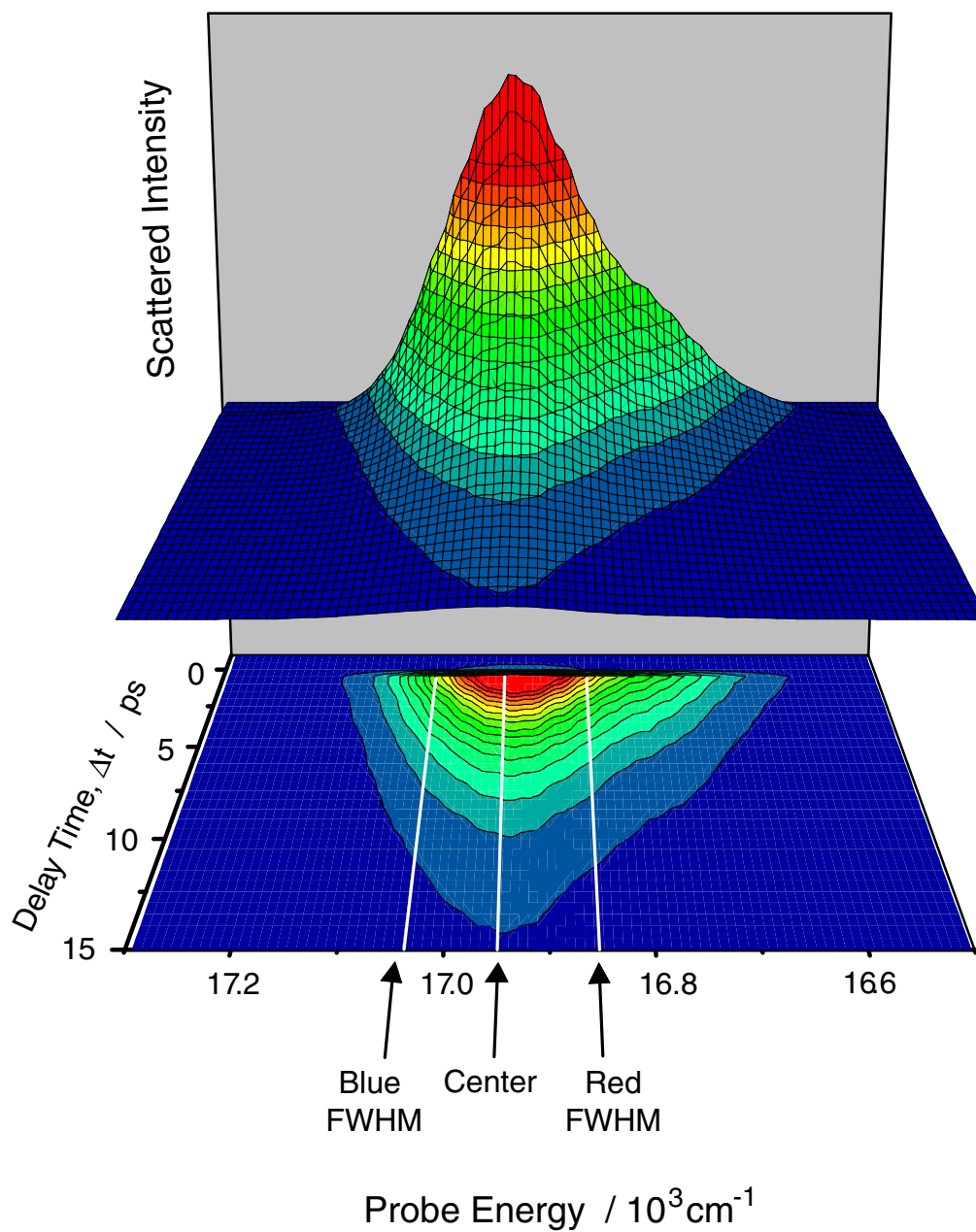


Figure 5.13: Plot of the intensity of the scattered *probe* pulse as a function of the delay time,  $\Delta t$  and the *probe* pulse energy. The dynamics are analyzed at the maximum of the scattered intensity (**C**), and the blue (**B**) and red (**R**) side of the FWHM in the spectral profile of the probe pulse. For details see text.



panel D and not observed in the transients at 17390, 16950 and 16330  $\text{cm}^{-1}$  of panels A-C in Fig. 5.14. This peak is attributed to the non-resonant scattering of the *probe* pulse from the grating formed by the electric field of the two *pump* pulses that is independent of an electronic resonance in the chromophore of the sample.<sup>115,122</sup> This non-resonant scattering is only observed for delay times during which the two *pump* pulses and the *probe* pulse interact simultaneously with the sample. The non-resonant peak shows a temporal profile that corresponds to the convolution of these three laser pulses. This scattering mechanism is in contrast to the resonant scattering from the grating of electronically excited molecules possessing an electronic transition that is in resonance with the frequency of the *probe* pulse. This resonant scattering can be observed for delay times of  $\Delta t \geq 100$  fs at all the spectral positions of the signal. For this resonant contribution, the *pump* pulses prepare a grating of a transient population and the *probe* pulse utilizes the  $S_n \leftarrow S_1$  transition for the resonant scattering.

The lack of a non-resonant peak for the transients in panels A-C in Fig. 5.14 is surprising at first since the blue-shift wavelengths of the *probe* pulse, used for the transients in panels A-C should lead to a stronger non-resonant scattering effect. The missing non-resonant peak centered around  $\Delta t = 0$  can therefore only be the result of a change in the ratio between the non-resonant signal and the resonant signal observed at  $\Delta t \geq 100$  fs. In the progression of Fig. 5.14 from panel A to D, the spectral position of the *probe* laser is shifted further towards, and eventually out of the red flank of the  $S_1$  state absorption. This change in the electronic resonance conditions causes a decrease in the intensity of the resonant signal in relation to the non-resonant contribution. For the transients recorded between 17390 and 16330  $\text{cm}^{-1}$  in panels A-C, the ratio between resonant and non-resonant effects is overwhelmingly in favor of the resonant signal. This makes the non-resonant contribution diminish to the point of not being apparent. For the transient recorded at 15950  $\text{cm}^{-1}$  in panel D, the decreasing resonant signal allows for the non-resonant effect to become noticeable.

In order to evaluate the resonant transient data, a model was formulated that includes the possible population and depopulation channels for the region of the  $S_1$  potential that is monitored by the *probe* pulse. For this, the  $S_2/S_1$  internal conversion is assumed to be the only mechanism with which the  $S_1$  state is populated, and this process is characterized with a time constant,  $\tau_{S_2/S_1}$ . Two possible channels are postulated with which molecules can leave the region of the  $S_1$  potential,

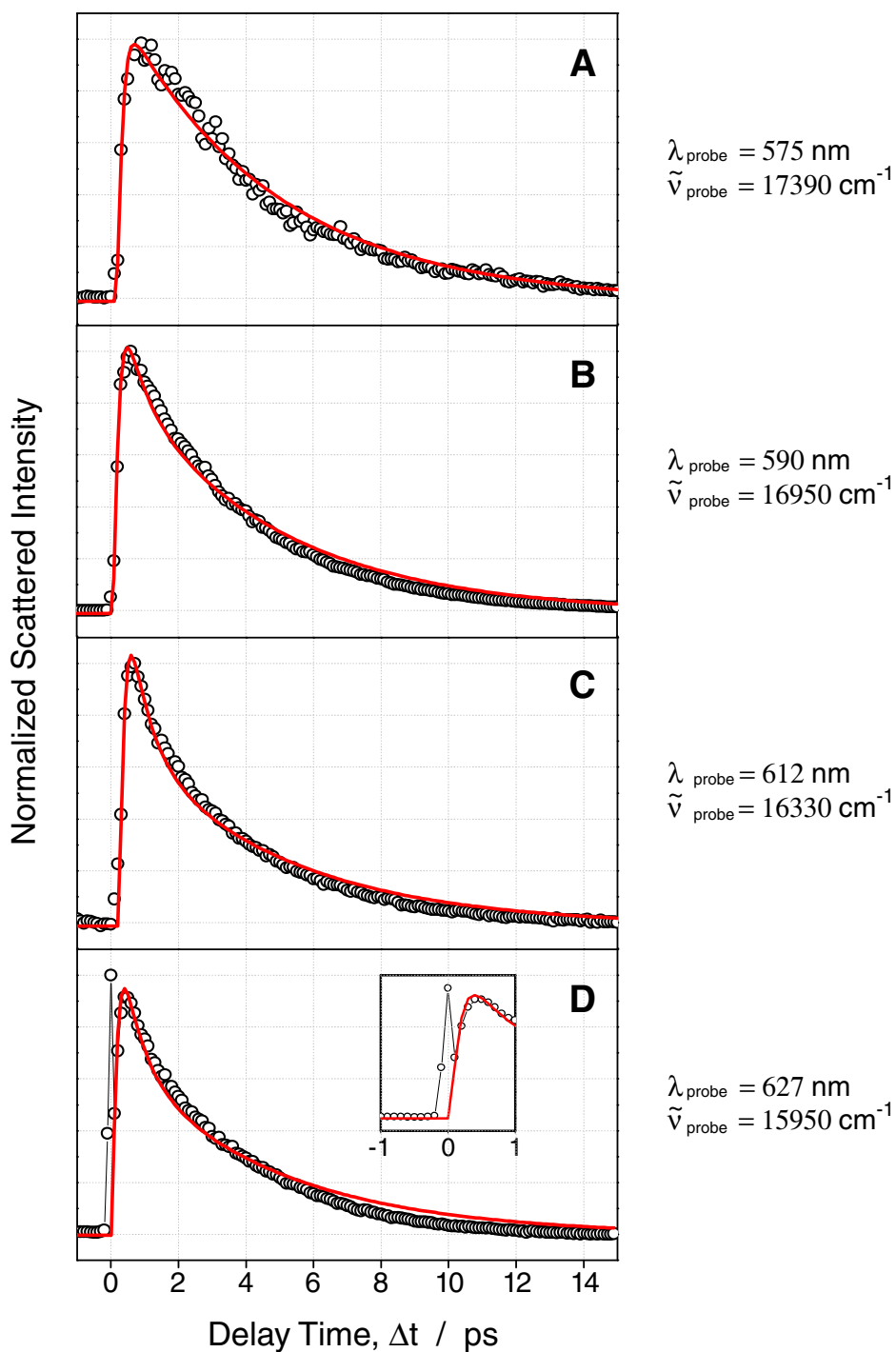


Figure 5.14: Scattered intensity of the *probe* pulse plotted as a function of the delay time,  $\Delta t$ . Panels A-D show the transient signal for different spectral positions of the *probe* laser. The experimental data points are shown as open circles and the theoretical fit as a solid lines, using equation 5.13 with the parameters of Model 1 listed in Table 5.2. The inset in panel D shows a time window that emphasizes the non-resonant scattering observed at this spectral position.

that is interrogated by the *probe* laser. For molecules in the vibrational ground state of the  $S_1$  potential, the  $S_1/S_0$  internal conversion is assumed to be the only channel of depopulation and this process is characterized with the time constant,  $\tau_{S_1/S_0}$ . Fluorescence as a decay channel for  $S_1$  state molecules can be neglected since the  $S_1 \leftarrow S_0$  optical transition is symmetry forbidden. For wavelengths of the *probe* laser that are red-shifted to the  $S_1$  state absorption, it is postulated that vibrationally hot states are also contributing to the signal, allowing for two possible channels that let molecules leave the region of the  $S_1$  potential being interrogated by the *probe* laser. The first channel is the  $S_1/S_0$  internal conversion taking place out of vibrationally hot states. The second channel is given by vibrational cooling due to system-bath coupling, resulting in energy transfer to solvent molecules. The cooling processes are characterized with a global time constant for all modes,  $\tau_{cool}$ .

The population of the  $S_1$  state being probed is characterized by the time constant of the  $S_2/S_1$  internal conversion,  $\tau_{S_2/S_1}$ . This channel of population is coupled with the multiple mechanisms of depopulation characterized by time constant for the  $S_2/S_1$  internal conversion,  $\tau_{S_1/S_0}$  and the global time constant for vibrational cooling  $\tau_{cool}$ , which are assumed to be independent of one another. These assumptions results in the following model, considering the time-dependency of transient gratings described in section 2.2.3:

$$I_{TG}(\Delta t) = \left| (1 - e^{-\Delta t/\tau_{S_2/S_1}}) \cdot [Ae^{-\Delta t/\tau_{cool}} + (1 - A)e^{-\Delta t/\tau_{S_1/S_0}}] \right|^2 \quad (5.13)$$

The model above possesses four variable parameters describing the transient data, consisting of  $\tau_{S_2/S_1}$ ,  $\tau_{cool}$ ,  $\tau_{S_1/S_0}$  and  $A$ , the amplitude factor, which describes the distribution between cooling and the  $S_1/S_0$  internal conversion as a decay channel out of the probe window. A free fit of all the parameters in equation 5.13 would prove difficult since the multitude of variables makes the determination of a minimum for the least-mean-square fit difficult. Due to this, data from the literature are used for the time constants of the processes involved in the dynamics. Macpherson *et.al.* performed solvent-dependent measurements of the  $S_2/S_1$  internal conversion using fluorescence up-conversion of the  $S_2$  state fluorescence and determined a time constant of  $\tau_{S_2/S_1} = 134$  fs for this process of  $\beta$ -carotene dissolved in acetone.<sup>96</sup> In the group of de Silvestri, the vibrational cooling effects in the  $S_1$  state of  $\beta$ -carotene subsequent to the  $S_2/S_1$  internal conversion were characterized with a global time constant of  $\tau_{cool} = 623$  fs, determined from a blue-shift in the intensity of the transient absorption of the

$S_1$  state.<sup>111</sup> Furthermore, transient infrared absorption measurements in the group of Sundström characterize the cooling in the  $S_1$  state after the  $S_2/S_1$  internal conversion in analog carotenoids with a very similar time constant of  $\tau_{cool} = 750$  fs.<sup>108</sup> The solvent effect on the  $S_1/S_0$  internal conversion was explored with transient absorption which allows for  $\tau_{S_1/S_0}$  in acetone to be estimated with 9.2 ps.<sup>97</sup> By using the time constants of  $\tau_{S_2/S_1} = 134$  fs,  $\tau_{cool} = 700$  fs and  $\tau_{S_1/S_0} = 9.2$  ps, to fit resonant signal from the transient grating data, only the amplitude factor,  $A$  is left as a free variable in equation 5.13. The amplitude factor,  $A$  describes the distribution, with which vibrational cooling and  $S_1/S_0$  internal conversion contribute to the decay of the population being probed. The distribution between these two channels is characterized by directly assigning the cooling process the factor  $A$  and the  $S_1/S_0$  internal conversion the corresponding amplitude of  $(1 - A)$ . This allows for the expression  $(A \cdot 100)$  to describe the percentage of vibrational states that take the pathway of vibrational cooling to leave the region of the  $S_1$  potential interrogated by the *probe* laser. The values used for the fixed parameters and the free variables in the fit procedure are summarized under Model 1 in Table 5.2.

This model can directly be applied to the transients in panels A-C in Fig. 5.14 that show a negligible non-resonant contribution at  $\Delta t = 0$ . For the transient in panel D, which shows a strong non-resonant contribution, a deconvolution of the resonant and non-resonant signal must be carried out since the kinetic model only describes the resonant scattering out of the  $S_1$  state. The non-resonant contribution is characterized by replacing the sample with a glass platelet and recording the transient signal under analog experimental conditions. Since the glass platelet shows no resonant response, the transient signal attained in this manor gives the temporal profile. The non-resonant profile acquired from the glass platelet corresponds to the convolution of all three lasers involved in the optical process and this profile. The non-resonant profile from the glass platelet is deconvoluted from the transient data points and the resulting, deconvoluted data set is fit with the model described above, where the data points remaining from the non-resonant profile are not included in the fitting process. In order to directly compare the quality of the fit to the transient data that did not require the deconvolution process, the theoretical curve generated out of the fit to the deconvoluted data set, is convoluted with the non-resonant profile from the glass platelet. This convoluted fit curve, is shown as a solid line with the original data in

Table 5.2: **Summary of the two models for the transient grating data using equation 5.13. The models differ with respect to the parameters that are fit as free variables and parameters that are fixed with literature values.**

Parameter	Model 1	Model 2
$\tau_{S_2/S_1}$ <sup>[96]</sup>	134 fs	134 fs
$\tau_{cool}$ <sup>[108,111]</sup>	700 fs	700 fs
$\tau_{S_1/S_0}$ <sup>[97]</sup>	9.20 ps	variable (panel C, Fig. 5.18)
$A$	variable (Fig. 5.15)	variable (Fig. 5.17)

panel D of Fig. 5.14.

The fits to the experimental data in Fig. 5.14 are shown as solid lines in the plots of panel A-D. The fits show that the model described by equation 5.13 gives a good first approximation of the experimental data using the time constants of from the literature summarized under Model 1 in Table 5.2. The amplitude factors,  $A$  determined from the fit are plotted in the form of  $(A \cdot 100)$  as a function of the spectral position of the *probe* pulse in Fig. 5.15. An interpretation of the tendency observed in the amplitude factor,  $A$  as a function of the spectral position of the *probe*, will be given in the following section. Despite the relatively good approximation of the transient data with the respective amplitude factors, deviations of the fit in specific regions of the experimental data call for a modification of the model. With the exception of the transient recorded at  $17390 \text{ cm}^{-1}$  shown in panel A of Fig. 5.14, the deviation from the transient data shows a tendency as the detection is shifted into the red from panel A to D. While the transient at  $17390 \text{ cm}^{-1}$  shows the best agreement with the model, the deviations from the experimental data increase with a further red-shift of the *probe* pulse. This growing deviation can be seen as an overestimated amplitude,  $A$  for the decay channel of cooling. The overestimated amplitude factor is the result of this fit variable overcompensating for a changing decay time of either the cooling process described by  $\tau_{cool}$  or the  $S_1/S_0$  internal conversion given by  $\tau_{S_1/S_0}$ . The deviations from the experimental data are particularly evident in panel D, in the region between  $6 \leq \Delta t \leq 15$  ps. Since the deviations are larger in the region characterized by the decay channel of  $S_1/S_0$  internal conversion, it is assumed that this parameter leads to the deviation of the fits from the experimental data.

In order to improve the quality of the fit to the experimental data, the fit procedure is modified so that a variable time constant for the  $S_1/S_0$  internal conversion is taken

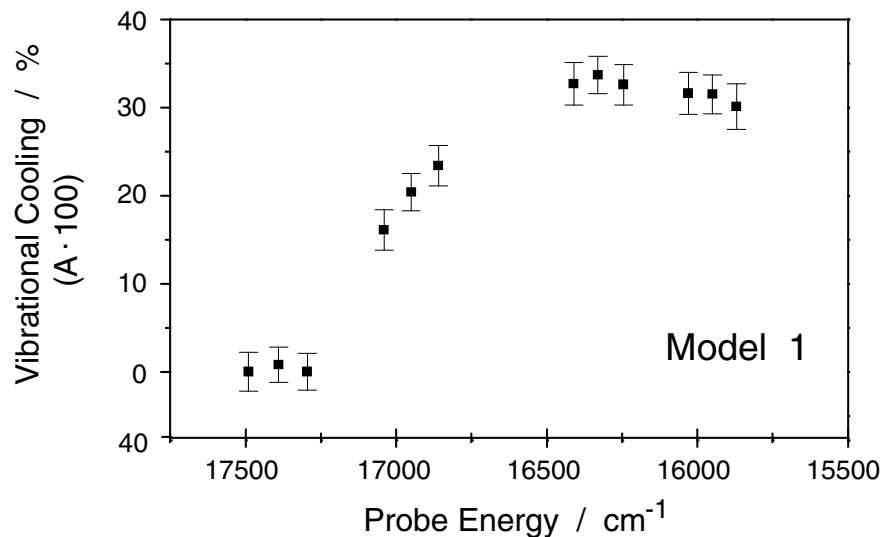


Figure 5.15: Percentage cooling ( $A \cdot 100$ ) as a decay channel out of the probe window in the  $S_1$  state shown as a function of the spectral position of the *probe* pulse. The amplitude factor,  $A$  is extracted with fits to the experimental data (see Fig. 5.14) using equation 5.13 as described in Model 1 (see Table 5.2).

into consideration for the different regions of the  $S_1$  potential that were probed. For this, the model described in equation 5.13 is again applied in the fit procedure and, in consistency with Model 1 presented above, the time constants for the  $S_2/S_1$  internal conversion and the cooling process are fixed with the literature values of  $\tau_{S_2/S_1} = 134$  fs and  $\tau_{cool} = 700$  fs, respectively. Deviating from the first model, not only is the amplitude factor  $A$  fit as a free parameter, the time constant for the  $S_1/S_0$  internal conversion,  $\tau_{S_1/S_0}$  is also set as a variable in the fit procedure. The parameters that were used in this second model are summarized in Table 5.2 under Model 2. Transients that require deconvolution of the resonant and non-resonant contributions of the signal are fit with the same procedure as described for the first model above. The obtained fits to the transient data are shown as solid lines in panels A-D in Fig. 5.16. Furthermore, the amplitude factor,  $A$  is plotted as a function of the spectral position of the *probe* in Fig. 5.17 and the results for the amplitude factor,  $A$  and the time constant,  $\tau_{S_1/S_0}$  are summarized in Fig. 5.18. The improvement in the quality

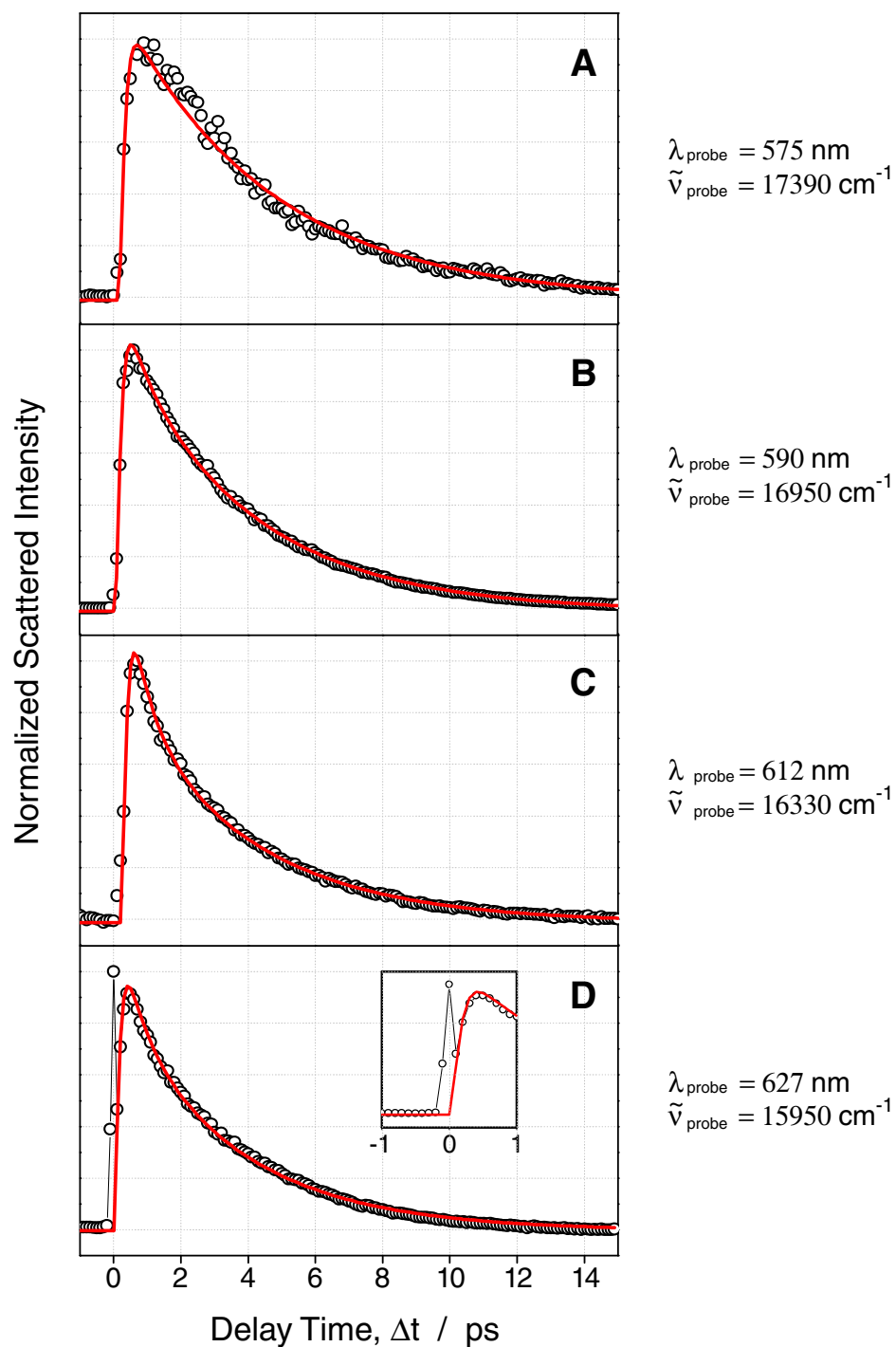


Figure 5.16: Scattered intensity of the *probe* pulse plotted as a function of the delay time,  $\Delta t$ . Panels A-D show the transient signal for different spectral positions of the *probe* laser. The experimental data points are shown as open circles and the theoretical fit as a solid lines, using equation 5.13 with the parameters of Model 2 listed in Table 5.2. The inset in panel D shows a time window that emphasizes the non-resonant scattering observed at this spectral position.

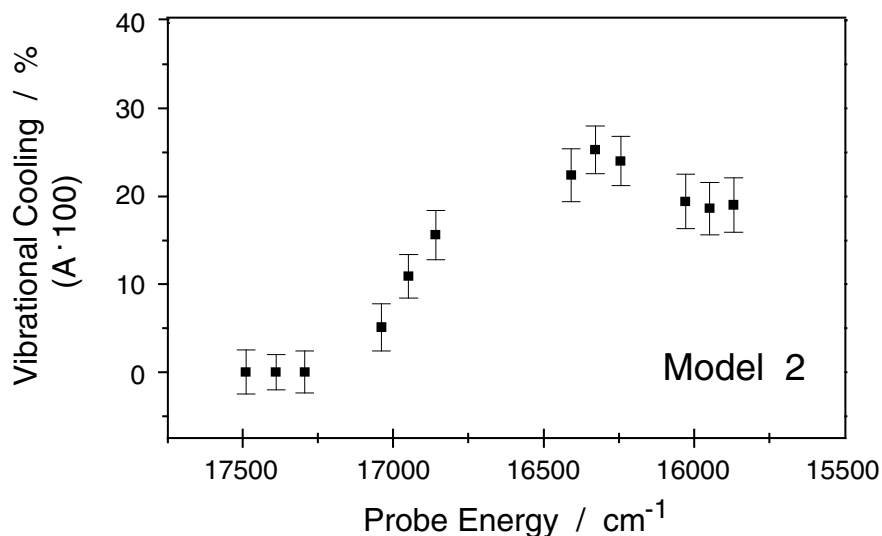


Figure 5.17: Percentage cooling ( $A \cdot 100$ ) as a decay channel out of the probe window in the  $S_1$  state shown as a function of the spectral position of the *probe* pulse. The amplitude factor,  $A$  is extracted with fits to the experimental data (see Fig. 5.14) using equation 5.13 as described in Model 2 (see Table 5.2).

of the fit to the experimental data for a variable  $\tau_{S_1/S_0}$ , in comparison to a fixed value for  $\tau_{S_1/S_0}$  in the first model, justifies adding an additional free variable into the fit procedure. By allowing  $\tau_{S_1/S_0}$  to fit freely, the second model shows excellent agreement to the experimental data. A comparison of the amplitude factor  $A$ , that gives the percentage cooling as a decay channel in the form of  $(A \cdot 100)$  in Fig. 5.17 shows the correction of the overestimated value in the first model (Fig. 5.15). The general tendency of this factor seen as step-like increase for red-shifted detection positions remains the same for both models. This behavior in the amplitude factor as well as the tendency observed for the time constant,  $\tau_{S_1/S_0}$  as a function of the spectral position of the *probe* will be discussed in the following section.

### 5.3.3 Discussion: Vibrational Cooling and the Increasing Rate of Internal Conversion

By fitting the experimental data with the second model, it was possible to characterize the behavior of the amplitude factor,  $A$  as a function of the spectral position of the *probe* pulse. This allowed for the characterization of the distribution between



the  $S_1/S_0$  internal conversion taking place parallel to the cooling of the vibrationally hot states in the  $S_1$  potential. Here, the vibrationally hot states are prepared through the internal conversion from the  $S_2$  state, that lies approximately  $6000\text{ cm}^{-1}$  above the  $S_1$  state. Furthermore, the time constant,  $\tau_{S_1/S_0}$  could also be characterized as a function of the spectral position of the *probe* pulse. The results of the fits described in the previous section are summarized in Fig. 5.18.

The characterization of the amplitude factor,  $A$  gives insight into the region of the  $S_1$  potential energy surface that is interrogated when the *probe* laser is red-shifted towards and eventually out of the red flank of the  $S_1$  state absorption. The  $S_2$  state lies approximately  $6000\text{ cm}^{-1}$  above the vibrational ground state of the  $S_1$  state for  $\beta$ -carotene in acetone and this excess energy is transferred into the vibrational modes of the  $S_1$  state subsequent to the  $S_2/S_1$  internal conversion. This generates vibrationally hot molecules in the  $S_1$  state that undergo cooling processes which have been characterized with transient absorption measurement by Cerullo *et.al.* as well as Nagae *et.al.*<sup>66,111</sup> The transient absorption shows a decrease in intensity of the red components and an increase in the blue components in the spectral profile as the  $S_1$  state population develops in time subsequent to the  $S_2/S_1$  internal conversion. For the transient grating measurements performed in this work, the red-shift in the *probe* laser corresponds to the detection of vibrationally hot states seen in the red components of the transient absorption spectra. The energy necessary for a resonance with the  $S_n \leftarrow S_1$  optical transition is insufficient for the vibrational ground state molecules in the  $S_1$  state when the *probe* laser is red-shifted in the absorption profile of the  $S_1$  state. This forces the *probe* to interrogate energetically higher lying vibrational states that can still utilize the  $S_n \leftarrow S_1$  optical transition, since the excess vibrational energy compensates for the lack of energy given by the red-shifted *probe* pulse. A similar experimental scheme was realized by Duppen *et.al.* with two color photon echos in pentacene.<sup>62</sup> This is schematically illustrated in Fig. 5.12.

The behavior of the amplitude factor,  $A$  as a function of the spectral position of the *probe* laser, displayed in Fig. 5.18, confirms that the strategy of spectrally red-shifting the *probe* for the interrogation of vibrationally hot states in the  $S_1$  potential energy surface shows the desired effect. The percentage cooling as a decay channel out of the region in the  $S_1$  state potential being probed, given by  $(A \cdot 100)$ , shows a strong increase of up to 25 % (Model 2, panel B of Fig. 5.18) for the red spectral

positions between 16500 and 15500  $\text{cm}^{-1}$ . This is in contrast to the absence of the fast decay channel of cooling for the blue spectral region of the *probe* from 17500 to approximately 17250  $\text{cm}^{-1}$ . Here, the *probe* laser primarily interrogates vibrational ground state molecules when the color is tuned to a spectral region that is in strong resonance with the  $S_n \leftarrow S_1$  optical transition. Important to further note about the behavior of the amplitude factor,  $A$  is the consistency between the tendency in the fit values for  $(A \cdot 100)$  extracted from different spectral positions of a single measurement and the general tendency of  $(A \cdot 100)$  when the central wavelength of the *probe* laser is shifted. Here, the sharp slope in the values extracted for the three spectral positions of the *probe* laser centered around 16950  $\text{cm}^{-1}$  follows the general tendency of  $(A \cdot 100)$  observed over the full spectral region probed. This strong variation in the dynamics for different spectral components of the measurement centered at 16950  $\text{cm}^{-1}$  can be seen from the asymmetry of the plot in Fig. 5.13.

The characterization of the vibrational cooling through the amplitude factor,  $A$  confirms the interrogation of vibrationally hot states in the  $S_1$  state for a red-shifted *probe*. With this established, it is possible to discuss the behavior of the time constant for the  $S_1/S_0$  internal conversion,  $\tau_{S_1/S_0}$  as a function of the spectral position of the *probe* laser. In the previous section, the transient data for the different spectral positions of the *probe* were characterized with a first model that used fixed literature values for all the time constants involved in the  $S_1$  state kinetics. This first model was presented in order to demonstrate that the fixed values for  $\tau_{S_2/S_1}$ ,  $\tau_{cool}$ , and  $\tau_{S_1/S_0}$  show good agreement for the *probe* between 17500 and 17250  $\text{cm}^{-1}$  (panel A, Fig. 5.14) that are in strong resonance with the  $S_n \leftarrow S_1$  optical transition. For red-shifted *probe* energies, where vibrationally hot states are interrogated and a vibrational cooling noticeably contributes to the kinetics observed, the first model is inadequate for describing the population flow in the vibrationally excited states, if the varying contribution of the cooling process via the amplitude factor,  $A$  is the only parameter considered. The obvious deviations of the fit using Model 1 (panel B-D, Fig. 5.14) call for the revised Model 2, that allows for a variable fit of the amplitude factor,  $A$  as well as the time constant describing the  $S_1/S_0$  internal conversion,  $\tau_{S_1/S_0}$ . This revision in the fit procedure allows the transient data for all spectral positions to show good agreement to the model (see panels A-D, Fig. 5.16)

When the time constant for the  $S_1/S_0$  internal conversion is varied in Model 2, a

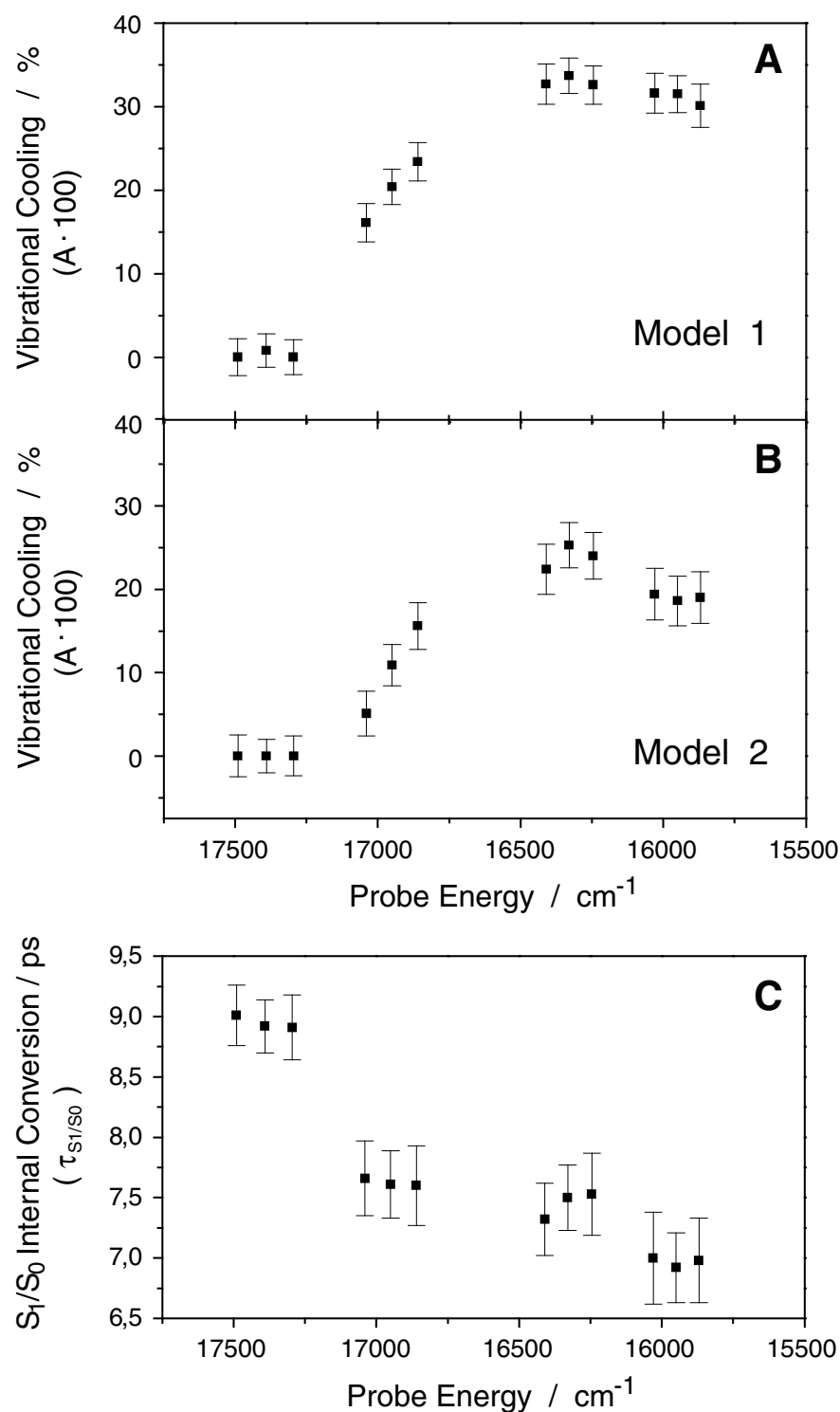


Figure 5.18: Parameters obtained from the fits to the experimental data shown in Fig. 5.14 and 5.16 using equation 5.13. **A.** Percentage cooling as a function of the probe energy using Model 1 (see Table 5.2). **B.** Percentage cooling as a function of the probe energy using Model 2 (see Table 5.2). **C.** Time constant,  $\tau_{S_1/S_0}$  for the respective internal conversion as a function of the probe energy using Model 2. For details see text.

clear tendency of  $\tau_{S_1/S_0}$  can be observed as a function of the spectral position of the *probe* pulse (panel C of Fig. 5.18). The plot of  $\tau_{S_1/S_0}$  clearly shows that the  $S_1/S_0$  internal conversion begins in the blue-shifted region with a value of  $\tau_{S_1/S_0} \approx 9.0$  ps and becomes faster for the red-shift spectral region, reaching a minimum in the time constant of approximately 7 ps in the region between 16500 and 15500  $\text{cm}^{-1}$ . A comparison of the behavior of the amplitude factor,  $A$  and the time constant,  $\tau_{S_1/S_0}$  as a function of the spectral position of the *probe* in panels B and C in Fig. 5.18, shows a strong correlation between both variables. Here,  $A$  as well as  $\tau_{S_1/S_0}$  show a sharp change in their values in the spectral region between 17250 and 16500  $\text{cm}^{-1}$  that become constant in the region from 16500 to 15500  $\text{cm}^{-1}$ . On the basis of this strong correlation, it is postulated that the vibrationally hot states that are interrogated with a red-shifted *probe* pulse undergo a faster internal conversion than vibrational ground state modes in the  $S_1$  potential. Since the contribution of vibrational cooling as a decay channel given by  $A$  is a measure for the amount of vibrationally excited states contributing to the total signal, it can be concluded that the decrease in the time constant for the  $S_1/S_0$  internal conversion, is the result of vibrationally excited states possessing a faster time constant for the  $S_1/S_0$  internal conversion.

Since a single time constant,  $\tau_{S_1/S_0}$  is used in the fit procedure, the values extracted from the fit represent an integral time constant for all vibrational states contributing to the signal (including vibrationally excited as well as vibrational ground state modes in the  $S_1$  potential). It would be possible to attempt a disentanglement of the time constants for vibrational excited states and vibrational ground state modes by modifying equation 5.13 to include two separate time constants for both cases. Attempts at these type of fits have shown that the two time constants for the internal conversion of vibrationally hot and cold modes do not show adequate separation in their values. Therefore, the experiments presented here only allow for the qualitative result that vibrationally hot states in the  $S_1$  state undergo a internal conversion to the electronic ground state with a faster time constant than the vibrational ground state modes.

The faster  $S_1/S_0$  internal conversion for vibrationally excited modes in the  $S_1$  state can be the result of a variety of parameters. Under consideration of equation 2.56 on page 39, advantageous Franck-Condon factors or coupling constants for the excited vibrational modes as well as the higher energy for a tunneling process or

overcoming of energy barriers can result in a faster internal conversion for the vibrationally hot molecules in the  $S_1$  state.<sup>68</sup> The experiments presented here do not allow for an identification of the effect that results in the faster internal conversion since the participating potentials are not characterized sufficiently. Furthermore, when the contribution of vibrationally excited states to the population transfer between the  $S_1$  and  $S_0$  potential is evaluated, the competition with the much faster process of vibrational cooling must be considered. This competition will lead to a low contribution of vibrationally excited states to the overall population transfer between the  $S_1$  and  $S_0$  state despite the fast time constant.

The last important property of the experimental data characterized by the behavior of the amplitude factor,  $A$  and the time constant,  $\tau_{S_1/S_0}$  is the step-like change as a function of the spectral position of the *probe* laser. Rather than a continuous change in these two parameters as the spectral position of the *probe* is red-shifted, both parameters show a jump in a relatively small spectral region of the *probe* to a value that stays consistent for further change in the *probe* energy. A sudden change in a molecular parameter as a function of energy can often be associated with a quantum effect in the molecular system. In the following, the step-like behavior of  $A$  and  $\tau_{S_1/S_0}$  (panel B and C, in Fig. 5.18, respectively) is correlated to quantum spacing of vibrational modes given by the  $S_1$  state Raman spectrum and the particular sensitivity of the  $S_n \leftarrow S_1$  optical transition to a specific Franck-Condon active mode.<sup>66</sup> The jump in the values for amplitude factor,  $A$  and the time constant,  $\tau_{S_1/S_0}$  takes place in a spectral region between approximately 17300 and 16300  $\text{cm}^{-1}$ , which corresponds to an energy difference of  $\tilde{\nu} \approx 1000 \text{ cm}^{-1}$ . This tendency in the  $S_1$  kinetics was attained by utilizing the  $S_n \leftarrow S_1$  optical transition, which shows a vibronic structure with an estimated energy spacing of  $\Delta\tilde{\nu} \approx 1150$  in the transient absorption spectrum at 20°K recorded by Kispert and coworkers (panel B, Fig. 5.1).<sup>95</sup> The structure shows that the  $S_n \leftarrow S_1$  transition possesses a Franck-Condon active mode or modes, that make this optical transition sensitive to the quantum spacing of particular vibrational modes. With the considerations presented above, the step-like behavior of the amplitude factor,  $A$  and the time constant,  $\tau_{S_1/S_0}$  is eventually the result of the *probe* pulse “jumping” from the interrogation of the vibrational ground state to the probing of vibrationally excited state modes. The fast change in ratio between the resonant and non-resonant signals (seen in the appearance of the non-resonant peak at  $\Delta t = 0$

in panel D of Fig. 5.16) in combination with the lack of a further step-like change in the behavior of  $A$  and  $\tau_{S_1/S_0}$  for the spectral region between 16000 and 15500  $\text{cm}^{-1}$  (panels B and C, in Fig. 5.18) could be the result of extremely poor Franck-Condon factors for the probing of higher vibrational quantum states. Despite this, the varying resonance conditions of the *probe* for different vibrational modes in the  $S_1$  state combined with the changing Franck-Condon factors and coupling constants for the different vibrational modes, as well as the position of possible energy barriers or conical intersections between the  $S_1$  and  $S_0$  state are too complex to be differentiated in the framework of this experiment. This makes the interpretation of the behavior in the amplitude factor,  $A$  and the time constant of internal conversion,  $\tau_{S_1/S_0}$  as a function of spectral position of the *probe* laser extremely complex. Due to this, the model of a quantum jump in the interrogation of the vibrational modes of the  $S_1$  state should only be seen as one possible interpretation.

With the interpretation of the experimental data presented in this section, it could be shown that transient gratings are an effective experimental method for investigating the kinetics in excited electronic dark states. Overall, the high sensitivity of this method has shown that the interrogation of an electronic potential in areas that show very small absorption cross sections is possible. In the case of  $\beta$ -carotene presented here, it could be shown that the strategy of red-shifting the *probe* laser out of an electronic resonance allows for the interrogation of vibrationally excited states within the electronic potential. With this, the characterization of vibrational cooling processes was possible and the good agreement to the transient absorption experiments in the literature was shown by using the time constants from these experiments for the evaluation of the transient grating data. Furthermore, it was possible to qualitatively characterize the kinetics in vibrationally excited and vibrational ground state modes. The distribution between cooling and internal conversion as a decay channel from these states as well as the increasing rate of internal conversion for vibrationally excited state modes could be characterized.

# Chapter 6

## Conclusion – Zusammenfassung

### 6.1 Conclusion

In the experiments presented in this work, third-order, time-resolved spectroscopy was applied to the disentanglement of nuclear and electronic degrees of freedom in polyatomic molecules. The motivation for approaching this problem was given by the decisive role that the coupling of nuclear and electronic dynamics plays in the mechanism of photochemical reactions and photobiological processes. In order to approach this complex problem, different strategies within the framework of time-resolved, four-wave mixing spectroscopy were developed that allowed for the dynamic as well as the energetic aspects of vibronic coupling in non-radiative transitions of polyatomic molecules to be addressed. This was achieved by utilizing the influence of optical as well as Raman resonances on four-wave mixing processes. These resonance effects on third-order, optical processes allow for a high selectivity to be attained with respect to the interrogation of specific aspects of molecular dynamics.

The development of different strategies within the framework of time-resolved, four-wave mixing spectroscopy for addressing the problem of vibronic coupling began with the experiments on gaseous iodine. This simple, well investigated molecular system was chosen in order to unambiguously characterize the effect of Raman resonances on four-wave mixing processes. Here, the broadband nature of femtosecond laser pulses, that exceed the energy spacing of the vibrational states in molecular iodine in their spectral profile, combined with a multichannel CCD detection scheme allowed for simultaneously generating and characterizing multiple FWM processes

parallel to one another. In doing so, the state-selectivity and the relevance of a Raman resonance in different FWM processes could be characterized in one experimental sweep. Specifically, a time-resolved degenerative four-wave mixing (DFWM) experiment was carried out on gaseous iodine that allowed for the dynamics of coherent Stokes Raman scattering (CSRS) as well as a coherent anti-Stokes Raman scattering (CARS) to be observed parallel to the dynamics of a DFWM process at different spectral positions of the FWM signal. Here, the state-selectivity of these different FWM processes manifests itself in the vibrational wave packet dynamics on different electronic potentials of iodine. It could be shown that Raman resonances determine the selectivity with which these FWM processes prepare and interrogate nuclear dynamics in different electronic states. It was established that optical processes that utilize virtual states do not contribute significantly to the dynamics prepared and interrogated in a molecular system while Raman resonant processes are decisive for the dynamics characterized with the CSRS, CARS and DFWM techniques.

With the insight gained into the relevance of Raman resonant processes in FWM spectroscopy, an experimental scheme was devised that utilizes this effect to selectively interrogate the dynamics of a specific vibrational mode within a polyatomic molecule during a radiationless electronic transition. Here, a CARS process was employed to selectively probe specific vibrational modes of a molecular system by variably tuning the energy difference between the lasers involved in the CARS process to be in Raman resonance with the vibrational energy spacing of a particular vibrational mode. This allows the CARS process to act as a filter that selectively interrogates the mode to which it is tuned to. Here, the filtering is achieved by means of the amplification of the CARS signal intensity in the Raman resonant case. For the vibrational mode that possesses the energy spacing in its quantum states that is resonant with the CARS process, a high signal intensity will be observed due to the resonance amplification. Other vibrational modes of the molecular system will display a negligible contribution to the CARS signal. Using this aspect of a tunable resonance enhancement within a CARS scheme, this optical process was incorporated in a time-resolved *pump-probe* experiment as a mode-selective probe mechanism. This type of experimental configuration, that employs four pulsed laser fields, was classified as a *pump-CARS* scheme. Here, a laser pulse independent of the CARS process initiates the molecular dynamics that are interrogated selectively with respect to the vibrational mode of the system



through the simultaneous interaction of the three pulsed fields involved in the CARS process. Time-resolution on a femtosecond timescale is achieved by introducing a time delay between the independent pump laser and the laser pulses of the CARS process.

The experimental configuration of a *pump*-CARS scheme was applied to the study of the nuclear dynamics involved in the radiationless electronic transition between the first excited singlet state ( $S_1$ ) and the electronic ground state ( $S_0$ ) of *all-trans*- $\beta$ -carotene. This internal conversion process in  $\beta$ -carotene was chosen as the object of investigation due to its significant role in the mechanism with which this molecule fulfills a variety of functions in photosynthesis. The *pump*-CARS scheme was realized in this molecule by allowing an independent *pump* laser to excite  $\beta$ -carotene into the second excited singlet state ( $S_2$ ). Here, an ultrafast internal conversion between the  $S_2$  and  $S_1$  state occurs due to the strong coupling of these states. The subsequent population flow from the  $S_1$  state to the electronic ground state, as a result of the internal conversion process between these electronic states, was monitored with a time variable CARS probe that interrogated the population flow into the vibrational states of a specific mode in the electronic ground state. The mode-selective CARS probe allowed for the characteristic timescale with which specific vibrational modes are repopulated in the  $S_0$  state to be determined. From the varying repopulation times of specific vibrational modes, a mechanism with which the full set of vibrational states of the  $S_0$  potential are repopulated subsequent to the internal conversion process could be postulated. Most importantly, the form of nuclear motion that primarily funnels the population between the two electronic states could be identified as the C=C symmetric stretch mode in the polyene backbone of  $\beta$ -carotene. With this, the reaction coordinate of this radiationless electronic transition could be identified. The experiment shows, that the CARS probe is capable of determining the nuclear motion coupled to a radiationless electronic transition in complex polyatomic systems.

The  $S_1/S_0$  internal conversion process in  $\beta$ -carotene was further investigated with time-resolved transient gratings. Here, the energetic aspects of a non-adiabatic transition was addressed by determining the influence of the vibrational energy on the rate of this internal conversion. For this, transient gratings were written into the sample space in resonance to the  $S_2$  state of  $\beta$ -carotene. The optical transition in the

$S_1$  state was utilized for the interrogation of the molecular dynamics. Vibrationally hot modes in the  $S_1$  state were prepared by populating these vibrational states via the  $S_2/S_1$  internal conversion process. In order to compare the rate of internal conversion taking place out of vibrational ground state modes versus this transition initiating out of vibrationally hot modes, the strategy of shifting the probe mechanism in the transient grating scheme to spectral positions within and out of the red flank of the  $S_1$  absorption profile was pursued. The spectral positions of the probe laser in optical resonance to the absorption of the  $S_1$  state allowed for the internal conversion of vibrational ground state molecules to be characterized while red-shifting the probe out of the absorption profile allowed for the internal conversion of vibrationally excited molecules to be monitored. The interrogation of different vibrational states was verified by determining the degree of vibrational cooling, taking place parallel to the internal conversion process. With this strategy, it could be shown that vibrationally hot states contribute to the internal conversion with a higher rate than vibrational ground state modes.

In summary, different third-order, optical processes in the framework of time-resolved FWM were applied to the study of non-adiabatic dynamics in polyatomic molecules. By utilizing the effect of optical as well as Raman resonances on different FWM processes, it could be shown that third-order, time-resolved spectroscopy is a powerful tool for gaining insight into complex molecular dynamics such as vibronic coupling. The experiments presented in this work showed that the CARS process, as a mode-selective probe in time-resolved experiments, is capable of disentangling nuclear and electronic dynamics. For future work, the experimental configuration of the *pump*-CARS scheme opens the possibility for investigating the reaction coordinate involved in various forms of non-adiabatic dynamics such as photochemical reactions and electron transfer where the large nuclear displacement leads to the breaking and formation of chemical bonds.

## 6.2 Zusammenfassung

In der vorliegenden Arbeit wurden verschiedene zeitaufgelöste, optische Prozesse dritter Ordnung zur Untersuchung nicht-adiabatischer Dynamiken in polyatomaren Molekülen vorgestellt. Derartige Dynamiken haben ihre Ursache in Kopplungen zwischen der Kern- und Elektronenbewegung im jeweiligen molekularen System und spielen eine entscheidende Rolle in vielen photochemischen und photobiologischen Prozessen. Es wurden unterschiedliche Strategien im Rahmen der zeitaufgelösten Vierwellenmisch-Spektroskopie entwickelt, die die Untersuchung sowohl dynamischer als auch energetischer Aspekte der vibronischen Kopplung bei strahlungslosen elektronischen Übergängen in polyatomaren Systemen ermöglichen. Dabei wurden sowohl elektronische als auch Raman-Resonanzen ausgenutzt, um eine hohe Selektivität in der Abfrage der molekularen Dynamik zu erzielen.

Um den Einfluss von Raman-Resonanzen auf Vierwellenmisch-Prozesse (FWM = *four-wave mixing*) eindeutig zu bestimmen, wurde zuerst das einfache und gut charakterisierte molekulare System Jod untersucht. Die spektrale Bandbreite der eingesetzten Femtosekunden-Laserpulse, die die Abstände zwischen den Schwingungszuständen im molekularen Jod deutlich überschreiten, kombiniert mit einer Multi-kanal CCD-Detektion, ermöglichte die gleichzeitige Initiierung und Charakterisierung verschiedener FWM-Prozesse. Femtosekunden-zeitaufgelöste entartete Vierwellenmischung (DFWM = *degenerate four-wave mixing*) an gasförmigem Jod ermöglichte eine simultane Beobachtung der Dynamik kohärenter Stokesscher Raman-Streuung (CSRS = *coherent Stokes Raman scattering*) und kohärenter anti-Stokesscher Raman-Streuung (CARS = *coherent anti-Stokes Raman scattering*) zusammen mit der Dynamik des eigentlichen DFWM-Prozesses durch Detektion an unterschiedlichen spektralen Positionen des FWM-Signals. Die Zustandsselektivität dieser drei FWM-Prozesse, die sich in der Generierung und Abfrage von Schwingungswellenpaketen auf verschiedenen elektronischen Potentialen von Jod manifestiert, konnte innerhalb eines einzigen Messvorgangs charakterisiert werden. Es zeigte sich, dass die Selektivität der unterschiedlichen FWM-Prozesse maßgeblich durch den Einfluss von Raman-Resonanzen bestimmt wird. Dagegen tragen Prozesse, bei denen virtuelle Zustände beteiligt sind, nicht wesentlich zum FWM Signal bei.

Basierend auf den so gewonnenen Erkenntnissen über den Einfluss von Raman-

Resonanzen bei FWM-Prozessen, wurde ein experimentelles Schema entwickelt, das es ermöglicht, selektiv bestimmte Schwingungsmoden eines polyatomaren Moleküls während eines strahlungslosen elektronischen Übergangs abzufragen. Hierzu wurde ein CARS-Prozess, der auf eine Raman-Resonanz in einem molekularen System abgestimmt wurde, als Abfrageschritt in einem *pump-probe*-Schema eingesetzt. Durch die erhebliche Signalverstärkung im Falle einer Raman-Resonanz stellt der CARS-Prozess einen durchstimmbaren Intensitätsfilter dar, der die Möglichkeit bietet, selektiv eine bestimmte Schwingungsmode in einem polyatomaren System abzufragen. Hierdurch stellen resonant angeregte Schwingungsmoden einen dominierenden Beitrag zum CARS-Prozess dar, während nicht-Raman-resonante Moden nur eine vernachlässigbare Intensität aufweisen. Dieses experimentelle Schema, bei dem vier gepulste Laser zum Einsatz kommen, wird in Analogie zu einem herkömmlichen *pump-probe*-Experiment als *pump-CARS*-Messung bezeichnet. Hierbei regt ein vom CARS-Prozess unabhängiger *pump*-Laser einen elektronischen Zustand an, dessen Besetzung durch die simultane Wechselwirkung mit den drei Laserpulsen des CARS-Prozesses modenselektiv abgefragt wird. Durch Einführung einer variablen Verzögerungszeit zwischen dem initiierenden *pump*-Laser und dem CARS-Prozess lässt sich die Relaxationsdynamik auf einer Femtosekunden-Zeitskala auflösen.

Diese experimentelle Konfiguration wurde zur Untersuchung der Kerndynamik des strahlungslosen elektronischen Übergangs zwischen dem ersten elektronisch angeregten Zustand ( $S_1$ ) und dem elektronischen Grundzustand ( $S_0$ ) des  $\beta$ -Carotin eingesetzt. Dieser nicht-adiabatische Übergang spielt eine maßgebliche Rolle bei der Photosynthese und wurde aus diesem Grund für die Untersuchungen ausgewählt. Zur Realisierung des *pump-CARS*-Schemas an  $\beta$ -Carotin regt der unabhängige *pump*-Laser den zweiten elektronisch angeregten Zustand ( $S_2$ ) an. Dieser  $S_2$ -Zustand ist über eine schnelle interne Konversion mit dem  $S_1$ -Zustand gekoppelt. Der hierdurch mögliche anschließende Populationstransfer vom  $S_1$ -Zustand in den elektronischen Grundzustand wird durch den zeitlich variablen CARS-Prozess modenselektiv abgefragt. Diese zustandsselektive Beobachtung der internen Konversion liefert die Zeitkonstanten, mit denen ausgewählte Schwingungsmoden im  $S_0$ -Zustand von  $\beta$ -Carotin wiederbevölkert werden. Aufgrund der Tatsache, dass unterschiedlichen Moden unterschiedliche Zeitkonstanten zugeordnet werden konnten, wurde ein Modell aufgestellt, welches die Konversion in den elektronischen Grundzustand in Abhängig-

keit von den Schwingungszuständen beschreibt. So konnte festgestellt werden, dass der Populationstransfer beim strahlungslosen Übergang von der  $S_1$ - auf die  $S_0$ -Potentialfläche vornehmlich über die symmetrische C=C-Streckschwingung verläuft; dieser Mode konnte die schnellste Zeitkonstante zugewiesen werden. Mit diesem Experiment konnte gezeigt werden, dass ein CARS-Prozess als Abfrageschritt in einem zeitaufgelösten *pump-probe* Experiment, in der Lage ist, die Kerndynamik zu bestimmen, die mit einem strahlungslosen elektronischen Übergang in einem komplexen polyatomaren Molekül verbunden ist.

Der energetische Aspekt des nicht-adiabatischen Übergangs zwischen dem  $S_1$ - und  $S_0$ -Zustand in  $\beta$ -Carotin wurde mittels zeitaufgelöster transienter Gitter untersucht (TG = *transient grating*). Hierbei wurde der Einfluss der Schwingungsenergie auf die Geschwindigkeit der internen Konversion bestimmt. Die transienten Gitter wurden durch die simultane Wechselwirkung mit zwei Laserpulsen in Resonanz zum  $S_2$ -Zustand in die untersuchte Probe geschrieben. Die Entwicklung der so erzeugten Populationsgitter wurde dann zeitverzögert unter Ausnutzung eines optischen Übergangs aus dem  $S_1$ -Zustand zur Beobachtung der Moleküldynamik mit einem dritten Laserpuls abgefragt. Schwingungsangeregte Zustände im  $S_1$ -Zustand wurden durch die interne Konversion des  $S_2$ -Zustands erzeugt. Um die Reaktionsgeschwindigkeit der internen Konversion zwischen  $S_1$  und  $S_0$  aus schwingungsangeregten Zuständen und Moden im Schwingungsgrundzustand des  $S_1$ -Potentials zu vergleichen, wurde das Signal spektral aufgelöst detektiert. Hierbei beinhaltete die rote Flanke des Absorptionsprofils des  $S_1$ -Zustandes die Dynamik der angeregten Schwingungsmoden. Die Abfrage der Dynamik an einer spektralen Position, die sich im Zentrum des Absorptionsprofils befindet, ermöglichte hingegen die Beobachtung der internen Konversion aus dem Grundzustand der Schwingungszustände. Auf diese Weise liess sich eine Zuordnung von Schwingungsrelaxationsprozessen durchführen. Mit der gewählten experimentellen Methode konnte gezeigt werden, dass schwingungsangeregte Zustände mit einer höheren Reaktionsgeschwindigkeit an der internen Konversion teilnehmen als Moden im Schwingungsgrundzustand.

Zusammenfassend wurden in dieser Arbeit unterschiedliche optische Prozesse dritter Ordnung zur Untersuchung nicht-adiabatischer Dynamiken in polyatomaren Molekülen angewandt. Durch Ausnutzung von sowohl elektronischen als auch Raman-Resonanzen auf unterschiedliche FWM-Prozesse konnte gezeigt werden, dass op-

tische Prozesse dritter Ordnung ein geeignetes Werkzeug zur Untersuchung komplexer Moleküldynamiken darstellen. Die Experimente in dieser Arbeit verdeutlichen, dass der CARS-Prozess als modenselektiver Abfrageschritt die spezifische Beobachtung von Kerndynamik während eines elektronischen Übergangs erlaubt. Ein solches *pump*-CARS-Schema kann in zukünftigen Arbeiten zur Identifizierung der Reaktionskoordinate unterschiedlicher nicht-adiabatischen Vorgänge eingesetzt werden. Besonders interessante Dynamiken, bei denen ein solches *pump*-CARS-Schema Verwendung finden könnte, sind photochemische Reaktionen und Elektronentransferprozesse, die aufgrund der großen Kernverschiebungen entlang der Reaktionskoordinate zum Bruch bzw. zur Bildung von chemischen Bindungen führen.

# Bibliography

- [1] Born, M.; Oppenheimer, R. *Ann. d. Phys.* **1927**, *84*, 457-484.
- [2] Born, M.; Heisenberg, W. *Ann. d. Phys.* **1924**, *74*, 1-31.
- [3] Schroedinger, E. *Phys. Rev.* **1926**, *28*, 1049-1070.
- [4] Englman, R.; Jortner, J. *Mol. Phys.* **1970**, *18*, 145-164.
- [5] Domcke, W.; Köppel, H.; Cederbaum, L. S. *Mol. Phys.* **1981**, *43*, 851-875.
- [6] Siebrand, W.; Zgierski, M. Z. *J. Chem. Phys.* **1981**, *75*, 1230-1238.
- [7] Bersuker, I. B.; Polinger, V. Z. *Vibronic Interaction in Molecules and Crystals*, volume 49 of *Springer Series: Chemical Physics* Springer: Berlin, 1985.
- [8] Bernardi, F.; Olivucci, M.; Robb, M. A. *Chem. Soc. Rev.* **1996**, 321-328.
- [9] Stock, G.; Domcke, W. *Adv. Chem. Phys.* **1997**, *100*, 1-169.
- [10] Bixon, M.; Jortner, J. *J. Chem. Phys.* **1997**, *107*, 1470-1482.
- [11] Blanchet, V.; Zgierski, M. Z.; Seideman, T.; Stolow, A. *Nature* **1999**, *401*, 52-54.
- [12] Schoenlein, R. W.; Peteanu, L. A.; Mathies, R. A.; Shank, C. V. *Science* **1991**, *254*, 412-415.
- [13] Wang, Q.; Schoenlein, R. W.; Peteanu, L. A.; Mathies, R. A.; Shank, C. V. *Science* **1994**, *266*, 422-424.
- [14] Scholes, G. D.; Fleming, G. R. *J. Phys. Chem. B* **2000**, *104*, 1854-1868.

- [15] Hahn, S.; Stock, G. *J. Phys. Chem. B* **2000**, *104*, 1146-1149.
- [16] Zewail, A. H. *Femtochemistry: Ultrafast Dynamics of the Chemical Bond*, volume I+II World Scientific: Singapore, 1994.
- [17] Manz, J.; Wöste, L., Eds.; *Femtosecond Chemistry*, VCH: Weinheim, 1995.
- [18] Chergui, M., Ed.; *Femtochemistry*, World Scientific: Singapore, 1996.
- [19] Shen, Y.-R. *The Principles of Nonlinear Optics*, Wiley: New York, 1984.
- [20] Mukamel, S. *Annu. Rev. Phys. Chem.* **1990**, *41*, 647-681.
- [21] Mukamel, S. *Principles of Nonlinear Optical Spectroscopy*, Oxford University Press: New York, 1995.
- [22] Kaiser, W., Ed.; *Ultrashort Laser Pulses: Generation and Applications*, volume 60 of *Topics in Applied Physics* Springer: Berlin, 1993.
- [23] Leonhardt, R.; Holzapfel, W.; Zinth, W.; Kaiser, W. *Rev. Phys. Appl.* **1987**, *22*, 1735-1741.
- [24] Zinth, W.; Leonhardt, R.; Holzapfel, W.; Kaiser, W. *IEEE J. Quant. Electr.* **1988**, *24*, 455-459.
- [25] Kohles, N.; Laubereau, A. *Appl. Phys. B* **1986**, *39*, 141-147.
- [26] Li, W.; Purucker, H.-G.; Laubereau, A. *Opt. Commun.* **1992**, *94*, 300-308.
- [27] Fickenscher, M.; Purucker, H.-G.; Laubereau, A. *Chem. Phys. Lett.* **1992**, *191*, 182-188.
- [28] Schmitt, M. *Femtosekunden-Zeitaufgelöste Kohärente Vierwellenmisch-Spektroskopie Zur Zustandsselektiven Untersuchung Molekularer Dynamik Einfacher Systeme*, Thesis, Universität Würzburg, 1998.
- [29] Chen, T.; Engel, V.; Heid, M.; Kiefer, W.; Knopp, G.; Materny, A.; Meyer, S.; Pausch, R.; Schmitt, M.; Schwoerer, H.; Siebert, T. *J. Molec. Struct.* **1999**, *480-481*, 33-43.



- [30] Materny, A.; Chen, T.; Schmitt, M.; Siebert, T.; Vierheilig, A.; Engel, V.; Kiefer, W. *Appl. Phys. B* **2000**, *71*, 299-317.
- [31] Meyer, S.; Schmitt, M.; Materny, A.; Kiefer, W.; Engel, V. *Chem. Phys. Lett.* **1997**, *281*, 332-336.
- [32] Meyer, S.; Schmitt, M.; Materny, A.; Kiefer, W.; Engel, V. *Chem. Phys. Lett.* **1999**, *301*, 248-254.
- [33] Rubner, O.; Schmitt, M.; Knopp, G.; Materny, A.; Kiefer, W.; Engel, V. *J. Phys. Chem. A* **1998**, *102*, 9734-9738.
- [34] Wiersma, D. A.; Duppen, K. *Science* **1987**, *237*, 1147-1154.
- [35] Schoenlein, R. W.; Mittleman, D. M.; Shiang, J. J.; Alivisatos, A. P.; Shank, C. V. *Phys. Rev. Lett.* **1993**, *70*, 1014-1017.
- [36] DeBoeij, W. P.; Pshenichnikov, M. S.; Wiersma, D. A. *J. Phys. Chem.* **1996**, *100*, 11806-11823.
- [37] DeBoeij, W. P. *Ultrafast Solvation Dynamics Explored by Nonlinear Optical Spectroscopy*, Thesis, Rijksuniversiteit Groningen, 1997.
- [38] Mukamel, S.; Hochstrasser, R. *Chem. Phys.* **2001**, *266*, 2-3.
- [39] Zanni, M. T.; Asplund, M. C.; Decatur, S. M.; Hochstrasser, R. M. Frequency Resolved and Heterodyned Femtosecond Infrared Echoes of Peptides; Multiple Pulse Coherent Vibrational Analogues of NMR. In *Springer Series: Chemical Physics*, Vol. 66; Springer: Berlin, 2001.
- [40] Zanni, M. T.; Gnanakaran, S.; Stenger, J.; Hochstrasser, R. M. *J. Phys. Chem. B* **2001**, *105*, 6520-6535.
- [41] Agarwal, R.; Krueger, B. P.; Scholes, G. D.; Yang, M.; Yom, J.; Mets, L.; Fleming, G. R. *J. Phys. Chem. B* **2000**, *104*, 2908-2918.
- [42] Motzkus, M.; Pedersen, S.; Zewail, A. H. *J. Phys. Chem.* **1996**, *100*, 5620-5633.
- [43] Sakurai, J. J. *Modern Quantum Mechanics*, Addison Wesley: New York, 1985.

- [44] Cohen-Tannoudji, C.; Diu, B.; Laloe, F. *Quantummechanics*, Walter de Gruyter: New York, 1997.
- [45] Meyer, S. *Nichtlineare Kurzzeitspektroskopie an Kleinen Molekülen*, Thesis, Universitaet Wuerzburg, 1999.
- [46] Engel, V. *Personal Communication*, Universitaet Wuerzburg, 2002.
- [47] Feynman, R. P. *Quantum Electrodynamics*, Benjamin Inc.: New York, 1961.
- [48] Hellwarth, R. W. *Progr. Quant. Electron.* **1977**, *5*, 1-68.
- [49] Weissbluth, M. *Photon Atom Interactions*, Academic Press: San Diego, 1988.
- [50] Zewail, A. H. *Acc. Chem. Res.* **1980**, *13*, 360-368.
- [51] Brewer, R. G.; Shoemaker, R. L. *Phys. Rev. A* **1972**, *6*, 2001-7.
- [52] Zinth, W.; Kaiser, W. Ultrafast Coherent Spectroscopy. In *Ultrafast Laser Pulses and Applications*, Vol. 60, Topics in Applied Physics ed.; Kaiser, W., Ed.; Springer: Berlin, 1988.
- [53] Eichler, H. J.; Gunter, P.; Pohl, D. W. *Laser Induced Dynamics Gratings*, Springer: Berlin, 1986.
- [54] Laubereau, A. Optical Nonlinearities with Ultrashort Laser Pulses. In *Ultrafast Laser Pulses and Applications*, Vol. 60, Topics in Applied Physics ed.; Kaiser, W., Ed.; Springer: Berlin, 1988.
- [55] Druet, S.; Taran, J.-P. *Progress in Quantum Electronics* **1981**, *7*, 1-72.
- [56] Lee, D.; Albrecht, A. C. A Unified View of Raman, Resonance Raman, Fluorescence Spectroscopy, and Their Analogues in Two-Photon Absorption. In *Advances in Infrared and Raman Spectroscopy*, Vol. 12; Clark, R. J. H.; Hester, R. E., Eds.; J. Wiley & Sons: Chichester, 1985.
- [57] Lee, D.; Albrecht, A. C. On Global Energy Conservation in Nonlinear Spectroscopies, Active and Passive. In *Adv. Chem. Phys.*, Vol. 83; Prigogine, I.; Rice, S. A., Eds.; J. Wiley & Sons: Chichester, 1993.

- [58] Kiefer, W.; Long, D., Eds.; *Raman Spectroscopy and Its Chemical Applications*, Reidel Pub. Co.: London, 1982.
- [59] Aben, E. A. A. *Resonanz CARS in I<sub>2</sub> and Br<sub>2</sub>*, Thesis, Universiteit Utrecht, 1992.
- [60] Demtroeder, W. *Laserspektroskopie*, Springer: Berlin, 1993.
- [61] Joo, T.; Dugan, M. A.; Albrecht, A. C. *Chem. Phys. Lett.* **1991**, *177*, 4-10.
- [62] Duppen, K.; Weitekamp, D. P.; Wiersma, D. A. *Chem. Phys. Lett.* **1984**, *108*, 551-554.
- [63] Meyer, S.; Engel, V. *J. Raman Spectrosc.* **2002**, *31*, 33-39.
- [64] Azumi, T.; Matsuzaki, K. *Photochem. and Photobio.* **1997**, *25*, 315-326.
- [65] Gillen, R. C. *Wellenpaketdynamik Von Konischen Durchschneidungen: Spektroskopie und Ultraschneller Zerfall Von Trans-Butadien und Ethinkation*, Thesis, Universitaet Muenchen, 2000.
- [66] Nagae, H.; Kuki, M.; Zhang, J.; Sashima, T.; Mukai, Y.; Koyama, Y. *J. Phys. Chem. A* **2000**, *104*, 4155-4166.
- [67] Chynwat, V.; Frank, H. *Chem. Phys.* **1995**, *194*, 237-244.
- [68] Klessinger, M. *Angew. Chem. Int. Ed.* **1995**, *34*, 549-551.
- [69] Garavelli, M.; Bernardi, F.; Olivucci, M.; Vreven, T.; Klein, S.; Celani, P.; Robb, M. A. *Faraday Discuss.* **1998**, *110*, 51-70.
- [70] Mueller, U.; Stock, G. *J. Chem. Phys.* **1997**, *107*, 6230-6245.
- [71] Thoss, M.; Stock, G. *Phys. Rev.* **1999**, *59*, 64-79.
- [72] Teller, E. *J. Phys. Chem.* **1937**, *41*, 109-116.
- [73] Lichten, W. *Phys. Rev.* **1967**, *164*, 131-142.
- [74] Smith, F. T. *Phys. Rev.* **1969**, *179*, 111-123.

- [75] Silfvast, W. T. *Laser Fundamentals*, Cambridge Uni. Press: New York, 1996.
- [76] Diels, J. C.; Rudolph, W. *Ultrashort Laser Pulse Phenomena*, Academic Press: San Diego, 1996.
- [77] Boyd, R. W. *Nonlinear Optics*, Academic Press: New York, 1992.
- [78] Shirley, J. A.; Hall, R. J.; Eckbreth, A. C. *Opt. Lett.* **1980**, *5*, 380-382.
- [79] Prior, Y. *Appl. Opt.* **1980**, *19*, 1741-1743.
- [80] Maeda, S.; Kamisuki, T.; Adachi, Y. . In *Advances in Non-Linear Spectroscopy*; Clark, R. J. H.; Hester, R. E., Eds.; J. Wiley & Sons: Chichester, 1988.
- [81] Funk, J.-M.; Michelis, T.; Eck, R.; Materny, A. *Appl. Spectrosc.* **1998**, *52*, 1541-1553.
- [82] Siebert, T.; Schmitt, M.; Michelis, T.; Materny, A.; Kiefer, W. *J. Raman Spectrosc.* **1999**, *30*, 807-813.
- [83] Tellinghuisen, J. *J. Chem. Phys.* **1973**, *58*, 2821-2829.
- [84] Kiefer, W.; Bernstein, H. J. *J. Mol. Spectrosc.* **1972**, *43*, 366-381.
- [85] Coxon, J. A. *J. Quant. Spectrosc. Radiat. Transfer* **1971**, *11*, 443.
- [86] Frank, H. A.; Cua, A.; Chynwat, V.; Young, A.; Gosztola, D.; Wasielewski, M. R. *Photosynth. Res.* **1994**, *41*, 398-395.
- [87] Chynwat, V.; Frank, H. A. *Chem. Phys.* **1995**, *194*, 237-244.
- [88] Frank, H. A.; Cogdell, R. J. *Photochem. and Photobio.* **1996**, *63*, 257-264.
- [89] Walla, P. J.; Yom, J.; Krueger, B. P.; Fleming, G. R. *J. Phys. Chem. B* **2000**, *104*, 4799-4806.
- [90] Schmitt, M.; Knopp, G.; Materny, A.; Kiefer, W. *Chem. Phys. Lett.* **1997**, *280*, 339.
- [91] Hahn, S.; Stock, G. *J. Chem. Phys.* **2002**, *116*, 1085-1091.

- [92] Schlücker, S.; Siebert, T.; Szeghalmi, A.; Schmitt, M.; Popp, J.; Kiefer, W. *J. Am. Chem. Soc.* submitted for publication.
- [93] Schlücker, S. *Lineare und Nichtlineare Raman-Spektroskopie an Biologisch Relevanten Modellsystemen*, Thesis, Universitaet Wuerzburg, 2002.
- [94] Connors, R. E.; Burns, D. S.; Farhoosh, R.; Frank, H. A. *J. Phys. Chem.* **1993**, *97*, 9351-9355.
- [95] Wasielewski, M. R.; Johnson, D. G.; Bradford, E. G.; Kispert, L. D. *J. Chem. Phys.* **1989**, *91*, 6691-6697.
- [96] Macpherson, A. N.; Gillbro, T. *J. Phys. Chem. A* **1998**, *102*, 5049-5058.
- [97] He, Z.; Gosztola, D.; Deng, Y.; Gao, G.; Wasielewski, M. R.; Kispert, L. D. *J. Phys. Chem. B* **2000**, *104*, 6668-6673.
- [98] Hashimoto, H.; Koyama, Y. *Chem. Phys. Lett.* **1989**, *154*, 321-325.
- [99] Koyama, Y.; Mukai, Y. Excited States of Retinoids, Carotinoids and Chlorophylls as Revealed by Time-Resolved, Electronic Absorption and Resonance Raman Spectroscopy. In *Biospectroscopy*, Vol. 21, Advances in Spectroscopy ed.; Clark, R. J. H.; Hester, R., Eds.; John Wiley & Sons: New York, 1993.
- [100] Hartl, I.; Gilch, P.; Zinth, W. *Appl. Phys. B* **2000**, *71*, 397-403.
- [101] Wernecke, W.; Kozisch, K.; Dreyer, J.; Rini, M.; Kummrow, A.; Elsaesser, T. Vibrational Excitation and Energy Redistribution Due to Back-Electron Transfer in Para-Nitroaniline. In *XII Conference on Ultrafast Processes in Spectroscopy (UPS)*; Florence, 2001.
- [102] Noguchi, T.; Hayashi, H.; Tasumi, M.; Atkinson, G. H. *J. Phys. Chem.* **1991**, *95*, 3167-3172.
- [103] Yoshizawa, M.; Kurosawa, M. *Phys. Rev.* **1999**, *61*, 013808/1-013808/6.
- [104] Yoshizawa, M.; Aoki, H.; Hashimoto, H. *Phys. Rev.* **2001**, *63*, 180301/1-180301/4.

- [105] Wachsmann-Hogiu, S. *Vibronic Coupling and Ultrafast Electron Transfer Studied by Picosecond Time-Resolved Resonance Raman and CARS Spectroscopy*, Thesis, Humboldt-Universitaet zu Berlin, 2001.
- [106] Funk, J.; Schmitt, U.; Kiefer, W.; Materny, A. *J. Raman Spectrosc.* **2000**, *31*, 743-753.
- [107] Zigmantas, D.; Polivka, T.; Hiller, R. G.; Roger, G.; Yartsev, A.; Sundström, V. *J. Phys. Chem. A* **2001**, *105*, 10296-10306.
- [108] Polivka, T.; Zigmantas, D.; Frank, H. A.; Bautista, J. A.; Herek, J. L.; Koyama, Y.; Fujii, R.; Sundström, V. *J. Phys. Chem. B* **2001**, *105*, 1072-1080.
- [109] Siebert, T.; Schmitt, M.; Engel, V.; Materny, A.; Kiefer, W. *J. Am. Chem. Soc.* **2002**, *124*, 6242-6243.
- [110] Shreve, A. P.; Trautman, J. K.; Owens, T. G.; Albrecht, A. C. *Chem. Phys. Lett.* **1991**, *178*, 89-96.
- [111] Cerullo, G.; Lanzani-Rossi, G.; DeSilvestri, S. *Phys. Rev. B* **2001**, *63*, 241104/1-241104/4.
- [112] Heid, M.; Schluecker, S.; Schmitt, U.; Chen, T.; Schweitzer-Stenner, R.; Engel, V.; Kiefer, W. *J. Raman Spectrosc.* **2001**, *32*, 771-784.
- [113] Ippen, E. P.; Shank, C. V. *Appl. Phys. Lett.* **1975**, *26*, 92-3.
- [114] Lau, A.; Werncke, W.; Pfeiffer, M. *Spectrochim. Acta Rev.* **1990**, *13*, 191-223.
- [115] Kohles, N.; Aechtner, P.; Laubereau, A. *Opt. Commun.* **1988**, *65*, 391-396.
- [116] Negri, F.; Orlando, G.; Zerbetto, F.; Zgierski, M. *J. Chem. Phys.* **1989**, *91*, 6215-6223.
- [117] Zerbetto, F.; Zgierski, M. Z.; Orlandi, G.; Marconi, G. *J. Chem. Phys.* **1987**, *87*, 2505-2511.
- [118] Zerbetto, F.; Zgierski, M. Z.; Negri, F.; Orlandi, G. *J. Chem. Phys.* **1988**, *89*, 3681-3688.

- [119] Orlandi, G.; Zerbetto, F.; Zgierski, M. Z. *Chem. Rev.* **1991**, *91*, 867-891.
- [120] Saito, S.; Tasumi, M. *J. Raman Spectrosc.* **1983**, *14*, 310-321.
- [121] Smith, B. R.; Bearpark, M. J.; Robb, M. A.; Bernardi, F.; Olivucci, M. *Chem. Phys. Lett.* **1995**, *242*, 27-32.
- [122] Ferwerda, H. A.; Terspsta, J.; Wiersma, D. A. *J. Chem. Phys.* **1989**, *91*, 3296-3305.





## Acknowledgements

*During the course of my work, it became evident to me that a thesis just isn't a one man enterprise. There are numerous people that I would like to thank for their support.*

Foremost, I would like to thank Prof. Dr. Wolfgang Kiefer for providing me with a fascinating subject for my thesis. The freedom to develop my ideas within this subject, the exceptional support and the continuous interest in the progress of my work was highly motivating. The possibility to visit numerous international conferences further provided an exciting environment for pursuing my thesis.

For questions concerning theoretical aspects of molecular physics, there is an office in the institute for physical chemistry in Wuerzburg where one can always find help. The office belongs to Prof. Dr. Volker Engel and I want to express my thanks for being able to visit at any time to discuss all the difficult theoretical aspects of my work in a free and constructive atmosphere. I would like to thank Prof. Dr. Arnulf Materny for introducing me to the subject matter of my thesis and for the great effort he has put into supervising my work. His guidance allowed me to make great progress in my thesis. I am very grateful to Prof. Dr. Jürgen Popp for his very personal support and for including me in his group. I very much enjoyed the work on the Mie-scattering experiments. I would like to say a truly special word of thanks to Dr. Michael Schmitt. His continuous interest and never ending support of all my efforts allowed me to achieve what would otherwise have certainly not been possible. The work under his supervision was the most constructive period of my thesis and I will certainly miss our conversations, whether scientific or personal.

My gratitude goes to Frau Ursula Müller for all her efforts towards the organization of virtually every aspect of my work. Additionally, her thoughtful reminders of deadlines I had long forgotten and her calming support in meeting these deadlines saved me from many chaotic situations. I would like to thank Wolfgang Liebler, Ralf Kohrmann, Peter Lang, Gerhard Bömmel, and Thomas Schreckling in the mechanics workshop, and Rainer Eck and Jürgen Zimmermann in the electronics workshop for

their outstanding technical support. The quality of electronic and mechanical devices they built was far beyond anything I could ever think of. Furthermore, I would like to thank Belinda Leimeister and Melanie Grom for all their technical assistance when the work load just got out of hand.

I would like to thank Gregor Knopp for passing on all his experience by spending many hours in the lab with me and, of course, the great time we had at the Femtochemistry conference in Toledo. I will certainly not forget the laughter I shared with Oliver Sbanski and Joachim Koster in our office due to the stories in particular German dialects and sketches from specific German comedians. The journey through China with Chen Tao and Mario Heid was an unforgettable experience. I want to thank Chen Tao for letting me see China from an inside view, and Mario Heid for being the best of travel mate and an exceptional colleague in all respects. I am grateful to Sebastian Schlücker for sharing his vast knowledge of “who is who” in scientific research with me and the fun discussions during the coffee breaks. I had great fun with Raman Maksimenka in the laser lab and I wish him the best of luck with all his work.

On a very personal note, I would like to thank my Tai-Chi teachers, Brigitte Moritz and Annette Schleich for giving me a way of leaving the “ups and downs” of a thesis behind me. I had a great time practicing Tai-Chi with my group.

In closing, I would like to give my deepest gratitude to my family and Liana. The support that one receives from a family can not be compared to anything else and it has been the most important element in all of my endeavors.

*Würzburg, the thirtieth of May, 2002.*

# LEBENS LAUF

TORSTEN UWE SIEBERT

---

## PERSÖNLICHE DATEN

Name: Torsten Uwe Siebert  
Geburtsdatum: 17. September 1969  
Geburtsort: Wiesbaden  
Familienstand: ledig

---

## SCHULAU SBILDUNG

1975–1977	Grundschule, Wehen
1977–1982	Elementary School (Grundschule), Denver, USA
1982–1983	Cheery Creek Middle Unit (Obersekunda und Unterprima), Denver, USA
1983–1988	Würzburg American High School (Gesamtschule), Würzburg Abschluss: High School Diplom
1988–1990	University of Maryland, München Abschluss: Associate in Arts
10.1990	Abitur (Prüfung für deutsche Staatsangehörige mit ausländischem Reifezeugnis beim Ministerialbeauftragten für Gymnasien in Oberbayern, München) Voraussetzung: High School Diplom/Associate in Arts Abschluss: Allgemeine Hochschulreife

---

## STUDIUM

10.1992–09.1998	Chemie Studium an der Julius-Maximilians-Universität, Würzburg
05.1995	Mündliche Diplom-Vorprüfung
11.1997	Mündliche Diplomprüfung
01.1998–09.1998	Diplomarbeit am Institut für Physikalische Chemie der Universität Würzburg bei Prof. Dr. W. Kiefer mit dem Thema: <i>“Femtosekunden-zeitaufgelöste kohärente anti-Stokessche Raman Streuung an einfachen molekularen Systemen”</i>

---

## PROMOTION

seit 10.1998	Am Institut für Physikalische Chemie der Universität Würzburg bei Prof. Dr. W. Kiefer mit dem Thema: <i>“Vierwellenmisch-Spektroskopie zur Untersuchung nicht-adiabatischer Dynamiken in polyatomaren Molekülen”</i>
--------------	--

---

## TÄTIGKEITEN

01.1991–01.1992	Grundwehrdienst
02.1992–09.1992	Praktikum im Bereich der kunsthistorischen Denkmalpflege, Firma “Löwen Restaurierung”, Erlenbach
05.1998–07.1998	Studentische Hilfskraft an der Universität Würzburg
seit 10.1998	Wissenschaftlicher Mitarbeiter an der Universität Würzburg